

POLYMER-MEDIATED METAL AND METAL OXIDE NANOPARTICLES:
SYNTHESIS, CHARACTERIZATION AND CONTROLLED ASSEMBLY

by

LITAO BAI

A DISSERTATION

Submitted in partial fulfillment of the requirements
for the degree of Doctor of Philosophy
in the Department of Chemistry
in the Graduate School of
The University of Alabama

TUSCALOOSA, ALABAMA

2009

Copyright Litao Bai 2009
ALL RIGHTS RESERVED

ABSTRACT

Functionalized nanoparticles and their assembly have been the subject of intense recent research activity. The stability and assembly of functionalized nanoparticles are still challenges for practical applications. Polymers are excellent stabilizing agents which can be used in nanoparticles synthesis. This dissertation describes polymer mediated nanoparticles which synthesized by both chemical and photo reduction techniques. The synthesis methods and assembly of polymer mediated nanoparticles were systematically studied.

Two kinds of polymers were used in this research: PAMAM dendrimer and hyperbranched polyethylenimine. PAMAM dendrimer was used as the host for the synthesis of FePt nanoparticles with narrow size distribution by chemical reduction. Magnetic and structural properties of the as-made and annealed samples were studied. The as-made FePt nanoparticles have the chemically disordered fcc structure and can be transformed into the chemically ordered fct structure after annealing. But the annealing process caused both the size and size distribution to increase. To prevent size increase during annealing, dendrimer mediated alloys were encapsulated in silica microspheres. Their magnetic properties can be manipulated by synthesis conditions. Polyethylenimine is a kind of hyperbranched polymer, which was used to encapsulate nanoparticles. With polyethylenimine, Pt and Co_3O_4 nanoparticles were synthesized by photochemical processes. Their formation mechanisms were discussed. The chemical and electrochemical catalytic activity of polyethylenimine mediated Pt nanoparticles were studied.

The results indicate that polyethylenimine is a good capping and reducing agent, and a carrier which improve samples stability and allows patterning.

Ordered discrete magnetic nanoparticle arrays were also fabricated. Polyethylenimine was used as a stabilizer to synthesize magnetite nanoparticles. Polyethylenimine coating of magnetite nanoparticles can effectively prevent the aggregation of the nanoparticles. By combining the capillary filling technique with a magnetic field, polyethylenimine mediated magnetite nanoparticles form ordered assembly, in which the resolution of the pattern is doubled. The formation process of ordered structures was systematically investigated. This method is technologically feasible and scalable to make ordered magnetic nanoparticles over a large area.

The result of this dissertation demonstrates that polymer stabilizers play an essential role in the synthesis of nanoparticles as well as their assembly.

LIST OF ABBREVIATIONS AND SYMBOLS

°C	Degree Celsius
A	Amperes
AFM	Atomic force microscopy
AGM	Alternating gradient magnetometry
CFIMF	Capillary filling in magnetic field
E	Energy
EDX/EDS	Energy dispersive x-ray spectroscopy
emu	Electromagnetic unit
eV	Electronvolt
fcc	Face centered cubic
fct	Face centered tetragonal
g	grams
G	Generation
H	Applied field
hr	Hour
H	Magnetic field
H _c	Coercivity
HRTEM	High resolution transmission electron microscopy
Hz	Hertz

K	Kelvin
K_B	Boltzman's constant
kV	Kilovolt
λ	Wavelength
M	Magnetization
m	Meter
MIMIC	Micromolding in capillaries
min	Minute
mL	Milliliter
mm	Millimeter
mM	Millimole
mol	Mole
M_r	Remanent magnetization
M_s	Saturation magnetization
nm	Nanometer
Oe	Oersted
PAMAM	Poly(amidoamine)
PEI	Poly(ethylenimine)
pH	Negative logarithm of the H^+ concentration
PPI	Poly(propylene imine)
PVP	Poly(N-vinyl-2-pyrrolidone)
θ	Angle
rpm	rotations per minute

SEM	Scanning electron microscopy
STM	Scanning tunneling microscopy
TEM	Transmission electron microscopy
TEOS	tetraethyl orthosilicate
UV	Ultraviolet
UV-Vis	Ultraviolet-Visible
W	Watt
XPS	X-ray photoelectron spectroscopy

ACKNOWLEDGMENTS

First and foremost, I would like to thank my research advisor Dr. Shane C. Street for his professional guidance and generous support. His broad knowledge, sparking ideas always inspired me. His extraordinary enthusiasm to research always encouraged me. He is the kindest, most understanding and friendly person. I greatly appreciate his consistent patient and trust over the course of this research and writing of this dissertation. My scientific improvement could never be the same without his dedication. It is a great of fortune and honor to have such a vivacious mentorship.

I would like to thank my dissertation committee members, Dr. Martin G. Bakker, Dr. Carolyn J. Cassady, Dr. Gregory J. Szulczewski, Dr. Mark L. Weaver, for their guidance and feedback throughout this endeavor. I sincerely appreciate their time and critical evaluation of my work.

I would like to thank all who have helped me in my research, especially the following: Dr. Shanlin Pan for useful discussion and constructive suggestions; Dr. Gregory Thompson, for his expertise in TEM and insightful suggestions; Dr. Earl Ada, Dr. James Weston, Dr. Mike Berch for their assistance in various aspects of characterization techniques.

Special gratitude is extended to all of my lab-mates, office-mates, and friends, especially Haiying Wan, Shelby Shuler, James Burgess, Clifton Watkins, Jonathan Williamson, Huizhen Zhu. They have been very generous with any kind of help I needed. We shared related projects and had very fruitful discussions.

A special appreciation goes out to the entire faculty and staff in MINT center and Department of Chemistry.

Finally, I would dearly like to express my sincere thanks to my parents and brother for their love and un-ending support. I would also like to thank my dear wife Bin for loving me and caring for me.

CONTENTS

ABSTRACT.....	II
LIST OF ABBREVIATIONS AND SYMBOLS	IV
ACKNOWLEDGMENTS	VII
LIST OF TABLES	XIV
LIST OF FIGURES	XV
CHAPTER 1 INTRODUCTION.....	1
1.1 NANOMATERIALS	1
1.1.1 General introduction	1
1.1.2 Dispersion and agglomeration	4
1.2 POLYMER MEDIATED NANOPARTICLES	8
1.2.1 Polymer matrices – PAMAM dendrimer	9
1.2.2 Polymer matrices – PEI	13
1.3 CHEMICAL AND PHOTOREDUCTION METHODS TO SYNTHESIZE NANOPARTICLES	15
1.3.1 Chemical reduction	16
1.3.2 Photoreduction methods.....	17
1.4 ASSEMBLY OF NANOPARTICLES ON SURFACES	18
1.4.1 Adsorption of nanoparticles on surfaces.....	19
1.4.2 Lay-by-layer (LBL) assembly.....	21

1.4.3 Patterning of nanoparticles arrays.....	22
1.5 OBJECTIVES OF THIS STUDY	26
1.6 OVERVIEW OF THIS DISSERTATION	27
CHAPTER 2 EXPERIMENTAL	29
2.1 CHEMICALS	29
2.2 SUBSTRATES	29
2.3 TECHNIQUES	29
CHAPTER 3 SYNTHESIS AND CATALYTIC ACTIVITY OF PHOTOREDUCED PLATINUM NANOPARTICLES IN POLYETHYLENIMINE MATRIX.....	44
3.1 SYNOPSIS	44
3.2 INTRODUCTION.....	44
3.3 EXPERIMENTAL METHODS.....	49
3.3.1 Materials	49
3.3.2 Synthesis of PEI/Pt NP	50
3.3.3 Characterization of PEI/Pt NP	50
3.3.4 Testing of the catalytic ability of Pt nanoparticles.....	51
3.3.5 Immobilization of PEI/Pt NP on GC electrode for CV test.....	51
3.3.6 Electrochemical instrumentation and measurements.....	52
3.4 RESULTS AND DISCUSSION	52
3.4.1 Preparation and characterization of PEI/Pt NP	52
3.4.2 Catalysis analyzation of photoreduced Pt nanoparticle	59
3.4.3 Electrocatalytic activity of photoreduced Pt nanoparticle	64
3.5 CONCLUSIONS	75

CHAPTER 4 UV IRRADIATION STRATEGY FOR SYNTHESIS OF SPINEL Co_3O_4 NANORODS AT ROOM TEMPERATURE 77

4.1 SYNOPSIS 77

4.2 INTRODUCTION..... 77

4.3 EXPERIMENTS 80

 4.3.1 Materials 80

 4.3.2 Preparation of Co_3O_4 nanorods..... 80

 4.3.3 Characterization of Co_3O_4 nanorods 80

4.4 RESULTS AND DISCUSSION 81

 4.4.1 UV-vis spectroscopic studies..... 81

 4.4.2 TEM, STEM and EDX analysis..... 82

 4.4.3 XRD and Raman analyses 86

 4.4.4 Discussion 88

4.5 CONCLUSIONS 93

CHAPTER 5 PREPARATION OF FEPT NANOPARTICLES BY CHEMICAL REDUCTION IN PAMAM-OH TEMPLATE..... 94

5.1 SYNOPSIS 94

5.2 INTRODUCTION..... 94

5.3 EXPERIMENTAL 97

 5.3.1 Materials 97

 5.3.2 Preparation of FePt nanoparticles 97

 5.3.3 Characterization of dendrimer mediated FePt nanoparticles 98

5.4 RESULTS AND DISCUSSION 99

5.4.1 Morphology analysis.....	99
5.4.2 Annealing induced particle sintering.....	105
5.4.3 Structural analysis of the FePt nanoparticles.....	109
5.4.4 Magnetic properties.....	111
5.5 CONCLUSIONS.....	112
CHAPTER 6 THE ENHANCED COERCIVITY FOR DENDRIMER MEDIATED MULTICOMPONENT MAGNETIC MICROSPHERES.....	114
6.1 SYNOPSIS.....	114
6.2 INTRODUCTION.....	114
6.3 EXPERIMENTAL.....	116
6.3.1 Materials.....	116
6.3.2 Preparation of CoPt@silica nanoparticles.....	116
6.3.3 Characterization of silica encapsulation of CoPt nanoparticles.....	117
6.4 RESULTS AND DISCUSSION.....	117
6.4.1 Characterization of as made dendrimer mediated CoPt nanoparticles.....	118
6.4.2 Characterization of silica encapsulated CoPt nanoparticles.....	120
6.5 CONCLUSIONS.....	124
CHAPTER 7 DOUBLING THE RESOLUTION OF DISCRETE FERROMAGNETIC NANOPARTICLES ARRAYS: CAPILLARY FILLING IN MAGNETIC FIELD	126
7.1 SYNOPSIS.....	126
7.2 INTRODUCTION.....	126
7.3 EXPERIMENTAL.....	129
7.3.1 Materials.....	129

7.3.2 Preparation of PEI encapsulated Fe ₃ O ₄	129
7.3.3 Patterning of PEI encapsulated Fe ₃ O ₄ nanoparticles	130
7.3.4 Characterization of PEI encapsulated Fe ₃ O ₄ and their pattern.....	132
7.4 RESULTS AND DISCUSSION	132
7.4.1 PEI encapsulated Fe ₃ O ₄ nanoparticles	132
7.4.2 Patterning of Fe ₃ O ₄ nanoparticles	138
7.5 CONCLUSIONS	144
CHAPTER 8 CONCLUSIONS AND SUGGESTIONS FOR FUTURE RESEARCH	146
8.1 CONCLUSIONS	146
8.2 SUGGESTIONS FOR FUTURE RESEARCH	148
8.2.1 Pt coated magnetite nanoparticles.....	149
8.2.2 Oxygen reduction reaction (ORR) of PEI mediated Pt nanoparticles	150
8.2.3 PEI mediated Ru nanoparticles	150
8.2.4 PEI mediated magnetic alloy nanoparticles.....	151
8.2.5 Enhanced coercivity by silica sphere encapsulation.....	151
8.2.6 Study of PEI oxidation mechanism.....	152
8.2.7 Patterned structures of magnetic nanoparticles.....	152
REFERENCES.....	153

LIST OF TABLES

Table 1.1 Effect of generation on selected properties of PAMAM	12
Table 3.1 Tabulated diameter analysis of samples with different PEI to Pt ratio.....	59
Table 3.2 Rate Constant for the Reduction of 4-Nitrophenol with different PEI to Pt ratio	62
Table 4.1 Peak assignments for the Raman spectrum of Co_3O_4 nanocrystals.....	88
Table 6.1 Comparison of the size and coercivity of silica encapsulated CoPt nanoparticles	123

LIST OF FIGURES

Figure 1.1 Pt nanoparticles prepared by photoreduction.....	2
Figure 1.2 The relationship between percentage of surface atoms and particle size.	6
Figure 1.3 Interaction of two particles stabilized by polymer.....	7
Figure 1.4 Schematic representation of a dendrimer structure.....	9
Figure 1.5 Chemical structure of G3 PAMAM dendrimers.	10
Figure 1.6 Chemical structure of PEI.....	14
Figure 1.7 Schematic representation of nanoparticles assembled on silanized glass.....	20
Figure 1.8 Scheme of fabrication of gold nanoparticle–polyelectrolyte multilayers.....	22
Figure 1.9 The preparation procedure of PDMS.....	24
Figure 1.10 Microcontact printing.....	25
Figure 1.11 Schematic of MIMIC used to fabricate pattern structures.	25
Figure 2. 1 The schematic outline of a TEM.....	32
Figure 2. 2 Production of characteristic EDS radiation.....	35
Figure 2.3 A schematic of XPS.	37
Figure 2.4 Energy level diagram of XPS process	37
Figure 2.5 Schematic illustration of reflection of x-rays from two planes.....	39

Figure 2.6 Schematic illustration of CV setup.	42
Figure 2.7 Cyclic voltammetry potential waveform.	42
Figure 3.1 Variation of UV-Vis absorption spectra during the photoreduction of H_2PtCl_6 . ..	55
Figure 3.2 TEM images of PEI/Pt NP synthesized by photoreduction.	56
Figure 3.3 TEM images of sample 1-9 with PEI:Pt ratio of (1) 1:1; (2) 3:1; (3) 6:1; (4) 8:1; (5) 10:1; (6) 15:1; (7) 17:1; (8) 18:1; (9) 20:1.....	58
Figure 3.4 a) Successive UV–Vis spectra of reduction of 4-NP by Pt nanoparticles with a PEI to Pt ratio of 18:1. Time of interval is 1min; b) Plots of $\ln A$ versus time for the reduction of 4-nitrophenol by Pt nanoparticles prepared by a PEI to Pt ratio of 18:1	61
Figure 3.5 The relation between the PEI to Pt ratio and catalytic activity.	64
Figure 3.6 CV of the as-prepared PEI/Pt NP coated electrode.....	66
Figure 3.7 Comparison of pure PEI with PEI/Pt NP coated electrode response in 1 M H_2SO_4	67
Figure 3.8 50 consecutive cycle scans of methanol oxidation obtained from PEI/Pt NP coated electrode with a scan rate of 20 mV/s in 1 M H_2SO_4 , 2 M methanol at 298 K. The peak current decreases with the number of scans. The voltammograms were recorded at 2 second intervals.	69
Figure 3.9 Comparison of pure PEI with PEI/Pt NP coated electrode response in 1 M H_2SO_4 + 2M CH_3OH	69
Figure 3.10 a) Magnified CV image of PEI/Pt NP coated electrode. Onset potential is	

labeled in the image. The arrows show the scan directions. b) Comparison of PEI/Pt NP with bulk Pt electrode. CV was scanned in 1M H₂SO₄+ 2M CH₃OH. 72

Figure 3.11 Long-term cycle stabilities of PEI/Pt NP coated electrode over 50 scan in N₂ saturated 1 M H₂SO₄ + 2 M CH₃OH at scan rate of 20 mV/s. a) The variation of the forward and backward scan peak current with cycle number. b) Plot of I_f/I_b versus cycle number. 73

Figure 3.12 Cyclic voltammograms of methanol oxidation on PEI/Pt NP coated electrode at 20 mV/s in 1M H₂SO₄, 2M CH₃OH with different potential scan limits labeled in the inset figure. The inset shows a magnified peak region. 74

Figure 3.13 Chronoamperometry curves of PEI/Pt NP coated electrode for methanol oxidation recorded at 0.3 V, 0.6 V and 0.8 V in 1M H₂SO₄, 2M CH₃OH, 298K. 75

Figure 4.1 Temporal evolution of UV-vis absorption spectra after UV irradiation of Co²⁺/PEI complex. 82

Figure 4.2 TEM characterization of as-prepared Co₃O₄ nanorods (a) low magnification image of Co₃O₄ nanorods coexisting with PEI, (b) length and width distributions of Co₃O₄ nanorods, (c) high magnification image of an individual rod, (d) a high-resolution transmission electron microscope (HRTEM) image taken from the middle part of the rod, (inset: FFT transform of HRTEM image). 84

Figure 4.3 EDX spectrum of Co₃O₄ nanorods taken from the spot 1 in the middle of inset STEM image. 85

Figure 4. 4 (a) XRD pattern of nanorods, confirming the formation of pure spinel structure cobalt oxide (Co₃O₄), (b) Raman spectrum of the Co₃O₄ nanorods. 87

Figure 4.5 TEM image of CoCl ₂ and PEI mixture at pH 3, irradiation with UV light for 34h. There is apparently no feature bigger than 40 nm in the image.....	90
Figure 4.6 Proposed formation process for Co ₃ O ₄	90
Figure 4. 7 TEM micrographs of Co ₃ O ₄ prepared at different molar ratios of PEI to Co ²⁺ : (a) 0.5:1, (b) 1:1, (c) 2:1, (d) 3:1, (e) 4:1, (f) 6:1.....	92
Figure 5.1 TEM images of as-prepared FePt nanoparticles, inset shows HRTEM of the same sample depicting the crystalline nature of the sample, b) Particle size distribution, curve fitting is based on the assumption of a log-normal distribution. c) TEM images of as-prepared FePt nanoparticles without dendrimers.	101
Figure 5.2 EDX of as-made PAMAM-OH mediated FePt nanoparticles.	102
Figure 5.3 XPS of as-made FePt nanoparticles.....	103
Figure 5.4 XPS of C1s for as-made FePt nanoparticles.....	104
Figure 5.5 XPS of Pt 4f for as-made FePt nanoparticles.....	104
Figure 5.6 (a)TEM images of FePt nanopaticles annealing at 500 °C for 1h; (b) at 600 °C for 1h, (c) at 700 °C for 1h; (d) HRTEM image of a single fct-FePt nanoparticle annealing at 700 °C for 1h with interfringe spacing at 0.195nm; (e) Particle size distribution of sample (a); (f) Particle size distribution of sample (b); (g) Particle size distribution of sample (c); (h) FFT of the corresponding HRTEM image (d).	107
Figure 5.7 Effects of annealing temperature on the average particle size and standard deviation.....	108

Figure 5.8 X-ray diffraction patterns of FePt nanoparticles: a) as-synthesized and a series of samples annealed under Ar/H ₂ (5%) for 1 hour at temperatures of (b) 500, (c) 600, and (d) 700 °C.	110
Figure 5.9 Hysteresis loops of FePt nanoparticle a) as-prepared, b) annealed at 500 °C, c) annealed at 600 °C, d) annealed at 700 °C.....	110
Figure 5.10 Room-temperature of coercivity values as a function of annealing temperature for dendrimer mediated FePt nanoparticles.	112
Figure 6.1 TEM image, size distribution and diffraction pattern of as-made dendrimer mediated CoPt nanoparticles.....	119
Figure 6.2 Magnetic loops of as-made dendrimer-coated CoPt nanoparticle.	119
Figure 6.3 TEM images of Silica encapsulated CoPt nanoparticles with TEOS of (1) 0.05 ml, (2) 0.1 ml, (3) 0.2 ml and their size distribution histograms.....	121
Figure 6.4 EDS of silica encapsulated CoPt nanoparticles. a) Whole EDS spectra, b) Selective region of EDS.....	122
Figure 6.5 Hysteresis loops of three silica encapsulated CoPt nanoparticles.	123
Figure 7.1 Scheme of capillary filling in magnetic field (CFIMF) used to fabricate pattern structures.	131
Figure 7.2 a) TEM image of PEI mediated magnetite nanoparticles. Insert show a HRTEM image of one single PEI mediated magnetite nanoparticle; b) size distribution of magnetite nanoparticles; c) Electron diffraction pattern of magnetite nanoparticles.	134

Figure 7.3 XRD pattern of the PEI coated magnetite nanoparticles.	135
Figure 7.4 AGM magnetometry curves of magnetite nanoparticles.	136
Figure 7.5 SEM image of magnetite nanoparticles. Insert is EDX spectra of the sample.	137
Figure 7.6 SEM image of assembled chain of magnetite nanoparticles. Inset shows magnified chain structure.	138
Figure 7. 7 AFM images of the PDMS stamp used in this dissertation.	139
Figure 7. 8 SEM image of magnetite nanoparticles pattern structure.	141
Figure 7.9 Schematic representation of the assembly process of MIMIC in magnetic field.	142
Figure 7.10 Scheme of MIMIC of magnetite nanoparticles without magnetic field.	143
Figure 7.11 SEM image of magnetite nanoparticles arrays by MIMIC without magnetic field.....	143
Figure 7.12 AFM images of higher resolution of magnetite nanoparticles array by MIMIC in magnetic field.....	144
Figure 8.1 TEM image of Pt/magnetite nanoparticles.	149
Figure 8.2 a) TEM image of Ru nanoparticles; b) EDX of as-made PEI mediated Ru nanoparticles.....	151

CHAPTER 1 Introduction

1.1 Nanomaterials

1.1.1 General introduction

The groundbreaking talk “There's Plenty of Room at the Bottom” by the eminent physicist Richard Feynman on December 29, 1959 accurately predicted the development of nanoscience and nanotechnology that we are witnessing. For example, he stated that if 100 atoms can store a bit of information, it turns out that all of the information that man has carefully accumulated in all the books in the world could be written in a cube of material $1/200$ of an inch wide. Before the invention of scanning probe microscopy, this idea was only a fascinating dream. But two decades ago, with modern scanning tunneling microscopes, scientists successfully used atoms to write information¹⁻³. Eigler et al fabricated an IBM logo with 35 Xe atoms on Ni⁴ in 1990. Each character was composed of far fewer than 100 atoms. Although the practical application in information storage of this technique is perhaps limited (they are too slow), this initial experiment is a scientific milestone. Information storage is only a very small region of fast progressing nanoscience and nanotechnology. “Nano” is a household word nowadays. Nanoscience and nanotechnology is a field full of enormous challenges. This field is enjoying worldwide attention and has seen an explosion in growth especially in the last two decades because of the advent of new strategies for synthesis and new instruments for characterization which allow the measurement and manipulation of nanoscale materials⁵.

Nanoscience and nanotechnology is a major direction of modern research and it mainly consists of fabricating, characterizing, and processing of materials where the characteristic dimensions are in the nanometer range⁶. These nanomaterials offer exciting possibilities to study

fundamental physics as well as the potential for many exciting applications⁷. Nanomaterials can be metals, metal oxides, semiconductors, ceramics, polymeric materials, or composite materials. Nanomaterials include nanoparticles, nanowires, nanorods, nanotubes, nanofilms, and materials made of nanoscale structures⁸. As a typical example, Figure 1.1 shows a TEM image of Pt nanoparticles made by photoreduction. The particle size in this figure is about 3 nm in diameter, and this sample has a very narrow size distribution.

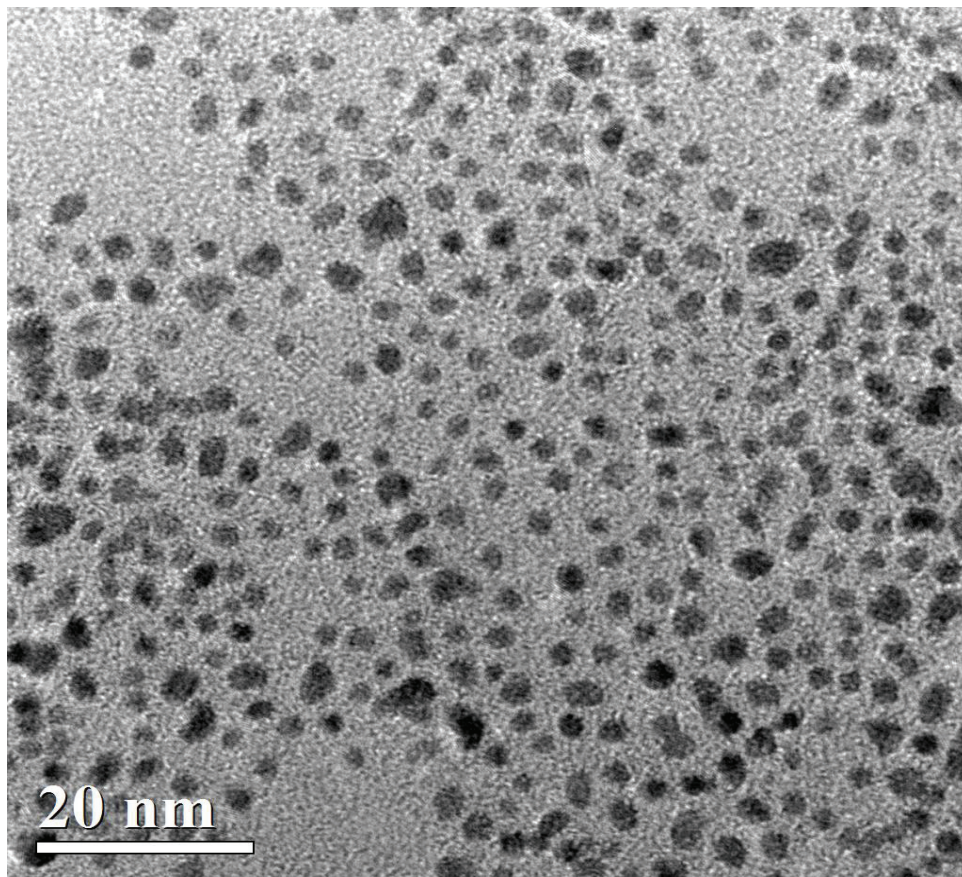


Figure 1.1 Pt nanoparticles prepared by photoreduction.

What is so exciting about nanomaterials? On the nanometer scale, properties of materials, regardless of composition, can change dramatically due to size effects⁹. For example, the limited

number of atoms/molecules in the material can alter its electro-optical properties as the density of states and the spatial length scale for electronic motion are reduced to the nanoscale dimension. Thus the materials can have distinct physical and chemical properties compared to atoms and bulk materials, such as luminescence, size dependent bandgap and plasmon absorption etc. Nanomaterials constitute a bridge between atoms and infinite bulk materials¹⁰. Manipulation of their geometry, composition, environment and size provide a way to tailor their properties. Their properties strongly depend on the particle size, shape and the nature of protection agents which modify their surfaces. For example, titanium dioxide becomes transparent in visible region at the nanoscale, and is able to absorb and reflect UV light^{11, 12}, however bulk titanium dioxide doesn't; ferroelectricity and ferromagnetism may lose their ferroelectricity and ferromagnetism when they are in nanometer scale¹³; gold nanoparticles exhibit excellent catalytic properties, while bulk gold does not⁹; bulk semiconductors will change to insulators when they are of nanometer scale¹⁴. Research in the behavior of nanomaterials have received emphasis from both basic science and technology points of view⁸.

Although we have stepped across the border of the nano-kingdom, there are many unknown regions in this realm. Here are the two main challenges before we can effectively integrate nanomaterials into macroscopic systems that interface with people and other technology:

- 1) Produce nanomaterials with controlled size, morphology, crystallinity, chemical composition and structure;
- 2) Improve the stability of nanomaterials, because their high intrinsic surface energy can cause degradation processes such as oxidation or sintering of the nanoparticles.

Stimulated by possible technological applications, immense efforts have been expended on fabricating nanostructures, designing new tools for characterization and manipulation. Ingenious methods for the preparation of nanomaterials have been reported in the past few years. Generally there are two broad areas of synthetic techniques: chemical methods and physical methods¹⁵. Each technique has its own advantages and disadvantages. Control over the shape and size is very important in the synthesis of nanoparticles, because their properties are size and shape dependent. In most cases, narrow size distribution is preferred. Based on these considerations, mechanical methods are not ideal because of relatively broad size distribution, varied geometry and imperfections in the surface structures, although large amounts of material can be generated in a short time¹⁶. Other physical techniques, such as the jet expansion method, can produce monodisperse nanomaterials, but the efficiency is low¹⁷. Even with disadvantages, physical techniques still play an important role in the fabrication of nanomaterials. Chemical techniques have been used for decades to prepare nanomaterials¹⁸. Chemical techniques are very attractive because they are versatile and can produce a large amount of nanomaterials in a short time. Because chemical processes are driven mainly by the reduction of Gibbs free energy, they can generate good chemical homogeneity and achieve size and shape control, and narrow size distributions. In other words, microstructure, crystallinity, and chemical composition of the final products can be controlled by these kinds of techniques. But due to the complexity, suitable reaction types and conditions need to be investigated for every material, and problems such as the entrapment of impurities normally need to be avoided.

1.1.2 Dispersion and agglomeration

High surface area is a basic characteristic of nanomaterials and a source of their special properties. In bulk materials, only a relatively small percentage of atoms are located at a surface,

while in nanomaterials, their small feature size ensures that more atoms, perhaps half or more in some cases, will be located on the surface. Figure 1.2 shows the relationship between size and percentage of surface atoms¹⁹. Nanomaterials have a much greater surface area per unit volume compared with bulk materials. This explains why their surface energy levels, electronic structure, and reactivity can be quite different from bulk materials. Nanomaterials typically have huge surface energies, so they are usually thermodynamically unstable or metastable²⁰. The high surface energy drives agglomeration to reduce surface energy. Agglomeration and sintering are serious issues for almost all nanomaterials²¹. And the huge increase of particle size can cause the loss of nanoscale properties. For example, if superparamagnetic nanoparticles aggregate together, they will lose their superparamagnetic properties. The desirable magnetic properties caused by single-magnetic-domain behavior can not be kept if ferromagnetic nanoparticles are not isolated from each other. Because of catalytic chemical reactions occur at surfaces, if aggregation occurs, reactivity of nanoparticles will dramatically decrease²². Aggregation may happen in the synthesis process or subsequent processing steps. It is very important to take measures to prevent aggregation in both preparation and processing steps.

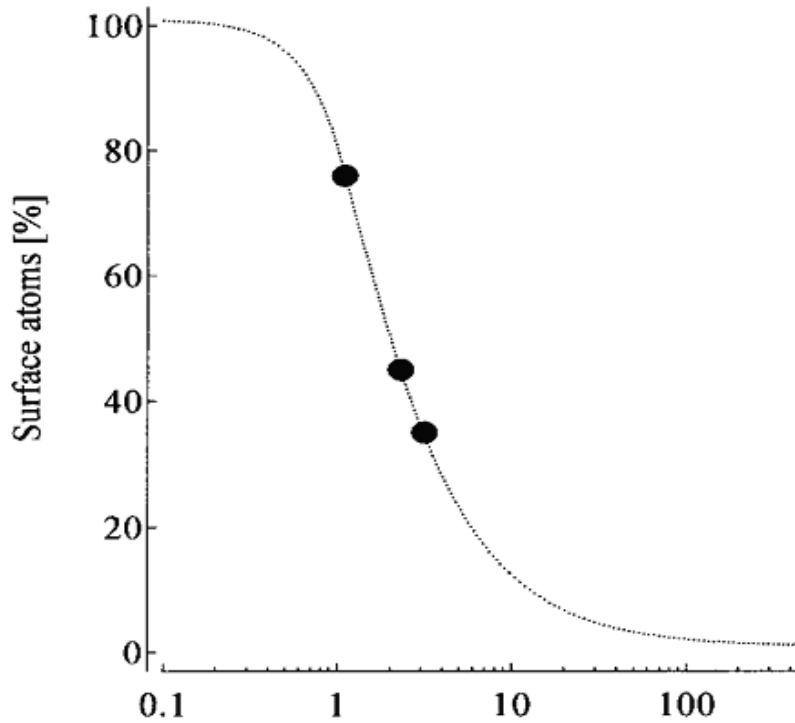


Figure 1.2 The relationship between percentage of surface atoms and particle size.

(Adapted from Ref 19)

Van der Waals forces can be strong enough to attract particles together when the size of nanoparticles is small enough. Two kinds of repulsive forces can be used to counteract attraction forces: electrostatic repulsion and the steric force. Electrostatic repulsion comes from the electric double layers around the nanoparticles. In polar organic media or dilute aqueous solution, electrostatic repulsive force can effectively overcome the attractive Van der Waals forces between nanoparticles. In this case, the system is kinetically stable. Electrostatic repulsion strongly depends on solution conditions, such as electrolyte concentration and pH. In the steric force method, stabilizers adsorbed on the surface of the nanoparticles increase the free energy of the system. The stabilizers around the particle can effectively restrict close contact of nanoparticles as their distance decreases. This method can be used with or without electrostatic barriers in both aqueous and non-aqueous media. The system is thermodynamically stable using

steric forces. Steric stabilization is also effective in concentrated solutions and is not sensitive to impurities²³. Kinetic and thermodynamic stabilization are totally different²⁴. Kinetic stabilization occurs because of the electrostatic repulsion restriction which increases the activation energy for aggregation of nanoparticles. Thermodynamic stabilization occurs because of the change in the energy balance created by polymers coating. Thermodynamic stabilization reflects a drive to the lowest overall energy of final products.

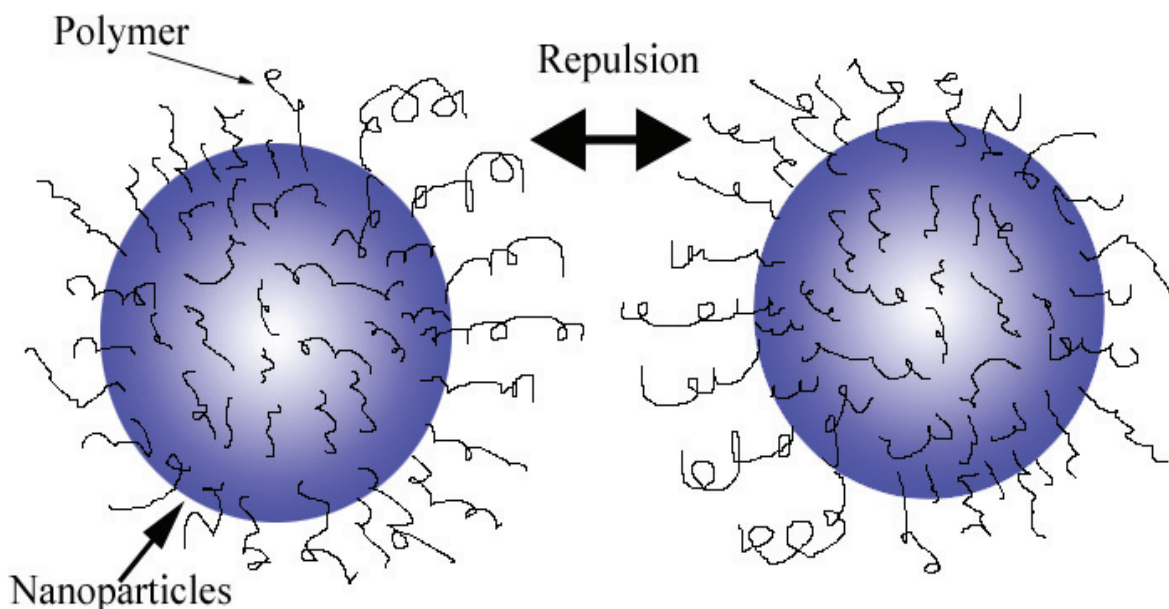


Figure 1.3 Schematic representative of interaction of two nanoparticles stabilized by polymers.

Steric stabilization is also called polymeric stabilization, because it is generally realized by polymer coating acting as a barrier. Polymer stabilizers can bond to the surface of nanoparticles or be physically adsorbed on the surface²⁵. Figure 1.3 shows a schematic representative of interaction of two particles stabilized by polymers. When the distance between two nanoparticles is smaller than the twice thickness of polymer layer, two polymer layers will

produce a repulsive force which results in increasing of system free energy. Aggregation will be avoided.

If polyelectrolytes are attached on the surface of nanoparticles, both the steric stabilization and electrostatic stabilization effects can act together²⁶. When two particles approach each other, both electrostatic repulsion and steric restriction prevent aggregation.

1.2 Polymer mediated nanoparticles

Polymer stabilizers are designed to prevent agglomeration of nanoparticles, but they also strongly influence the growth of nanoparticles in the preparation process and the final properties of nanoparticles. Polymer mediated nanoparticles have been synthesized traditionally by in situ generation of metal nanoparticles by reduction of metal precursors within a polymer matrix^{27, 28}. In this synthesis step, polymer stabilizers, which have strong affinity with the surface of nanoparticles, may block the growth sites, and this will strongly affect the growth rate of nanoparticles. Some kind of polymers can form special templates, wherein nanoparticles are confined and form certain shapes²⁹. Full coverage of polymer stabilizer may serious affect their catalytic properties³⁰. In addition to stabilization of nanoparticles, the polymer itself can provide additional functionality. For example, various polymer mediated magnetic nanoparticles have been synthesized with the intention to incorporate functional groups on their surface or to treat their surface to perform a certain function³¹, such as polymer-mediated gamma-Fe₂O₃³², PEI mediated FePt³³ et al.

Homopolymers, block copolymers, and branched polymers have been used to synthesize stable nanoparticles for various applications³⁴. Many kinds of metal nanoparticles have be

synthesized within these polymer templates, including Cu, Au, Ag, Pt, Pd, Rh, and others³⁵. In this dissertation two kinds of polyelectrolytes were used: PAMAM dendrimer and PEI.

1.2.1 Polymer matrices – PAMAM dendrimer

Dendrimers are hyperbranched monodisperse macromolecules, which are constructed around a core and are well defined by regular branching generation after generation^{36, 37}. The main difference between dendrimers and other hyperbranched polymers is polydispersity. Dendrimers' polydispersity are of order of 1.02-1.04, much lower than hyperbranched polymers generally. Dendrimers can be synthesized with near perfect control over size and functional group placement, and are composed of a core, repeating branches, and peripheral groups (as shown in Figure 1.4). There are many types of dendrimers; polyamidoamine (PAMAM) is among the most common³⁸. It is commercially available. Figure 1.5 shows the chemical structure of G3 (three generation) PAMAM³⁹.

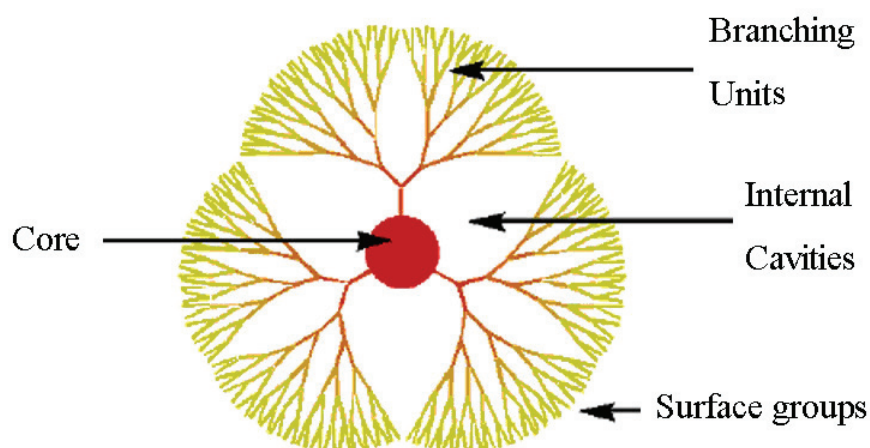


Figure 1.4 Schematic representation of a dendrimer structure.

(Adapted from <http://www.ninger.com/dendrimer/index.htm>. Accessed on Aug. 17, 09)

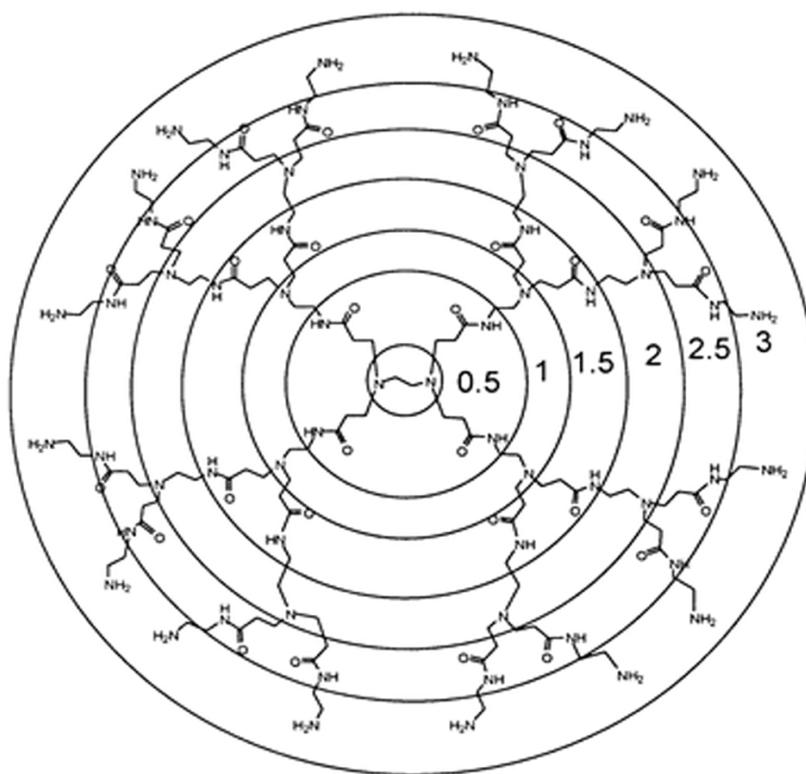


Figure 1.5 Chemical structure of G3 PAMAM dendrimers.
(Adapted from Ref 39)

The generation of dendrimers largely defines their shape. The size of dendrimers varies from 2 to 15 nm. Table 1.1 summarizes the physical aspects (molecular weight, measured diameter, and the number of surface groups) of PAMAM as a function of generation⁴⁰. The molecular weight and number of peripheral terminal groups increases exponentially with generation, while the size increases almost linearly. The physical state of dendrimers is a function of solution conditions, such as pH. Previous work⁴¹⁻⁴³ shows that PAMAM will swell in low pH solution because protonation of both primary amine and tertiary amine cause electrostatic repulsion; back-folding occurs in high pH solution because of hydrogen bonding between tertiary amines and primary amines. Lower generation dendrimers have an open and

asymmetric shape. High generation dendrimers show globular structure with large interior voids which can be used as a template to entrap and stabilize nanoparticles. Their terminal groups can be modified with carboxy, hydroxyl, and hydrocarboxy groups, which affect their properties. Their dendritic branches and terminal groups can serve as gates to control access of chemicals to the cavity inside. Their internal functional groups can be used to sequester metal ions or nanoparticles. Because primary amines are more basic than the internal amines (tertiary amine), in certain pH, dendrimers can be partially protonated and thus metal precursors will only complex with the tertiary amines. For example, many metal ions, such as Cu^{2+} , Pd^{2+} , Pt^{2+} , Ni^{2+} , Au^{3+} , and Ru^{3+} , can be sorbed into PAMAM interiors via chemical interactions with interior tertiary amines⁴⁴.

Table 1.1 Effect of generation on selected properties of PAMAM

(Adapted from Ref 44)

Generation (G)	Diameter (nm)	Molecular weight (Da)	No. of surface groups
0	1.5	517	4
1	2.2	1430	8
2	2.9	3256	16
3	3.6	6909	32
4	4.5	14215	64
5	5.4	28826	128
6	6.7	58048	256
7	8.1	116493	512
8	9.7	233383	1024
9	11.4	467162	2048
10	13.5	934720	4096

Using different generation dendrimers with various functional groups as template, small size mono- and bimetallic nanoparticles can also be effectively synthesized⁴⁵. There are two

versatile methods to prepare dendrimer mediated nanoparticles: interdendrimer and intradendrimer. Crooks⁴⁶ and Tomalia⁴⁷ first introduced nanoparticles inside the dendrimers in 1998. Their result shows that complexation of tertiary amine with metal ions could be followed by reduction to metal nanoparticles inside of the PAMAM dendrimers. Esumi⁴⁸⁻⁵¹ prepared gold nanoparticles stabilized by the periphery of dendrimers using photoreduction of H₂AuCl₄. Amis et al⁵² systematically investigated the reduction of H₂AuCl₄ from various generations of PAMAM dendrimers in aqueous solution by chemical reduction. They found that the lower generation of PAMAM dendrimers act as colloidal stabilizers whereas the higher generation of dendrimers acts as nanoreactors for nanoparticle formation within the dendrimers.

With dendrimers as template, palladium, platinum, and silver also have been synthesized which is shown in a large volume of research⁵³⁻⁵⁵. Moreover, if metal precursors were simultaneously added to dendrimers template before the reduction, they can form bimetal alloy; if metal precursors were added stepwise, core-shell nanoparticles can be synthesized^{56, 57}. The size of dendrimers mediated nanoparticles can be tuned by varying the dendrimer/metal ion ratio. For example, Crooks⁵⁸ have shown that a dendrimer/PdCl₄²⁻ ratio of 1:40 yields Pd nanoparticles having a diameter of 1.7 ± 0.2 nm regardless of the dendrimer generation (G_n-OH dendrimers). However, the size of Au nanoparticles synthesized within high-generation (G₆-G₉) PAMAM dendrimers correlates well with the number of gold atoms added per dendrimer⁵².

1.2.2 Polymer matrices – PEI

Polyethylenimine (PEI) is a readily available cationic polymer which has been used for more than fifty years in modern industry as adhesives, dispersion stabilizers, thickeners, and flocculating agents⁵⁹. It is a hyperbranched polymer which is simpler to synthesis on a large scale

compared with dendrimers, and is much cheaper than dendrimers. A one-pot method is generally used which generates less regular structure and much broader molecular distribution than dendrimers⁶⁰. Figure 1.6 shows the basic chemical structure of PEI⁶¹. PEI have similar functional groups to dendrimers: secondary amino groups in the main chain, tertiary amino branch points, and primary amino end groups. Because of the high degree of branching, PEI molecules have a globular structure with relatively little conformational freedom⁶². They actually present a structure with architecture very similar to PAMAM dendrimers (roughly spherical in shape for PEI with high molecular weight and high degree of branching). It should also be noted that PEI may be easily functionalized because they present a polyamine on the outer terminal groups.

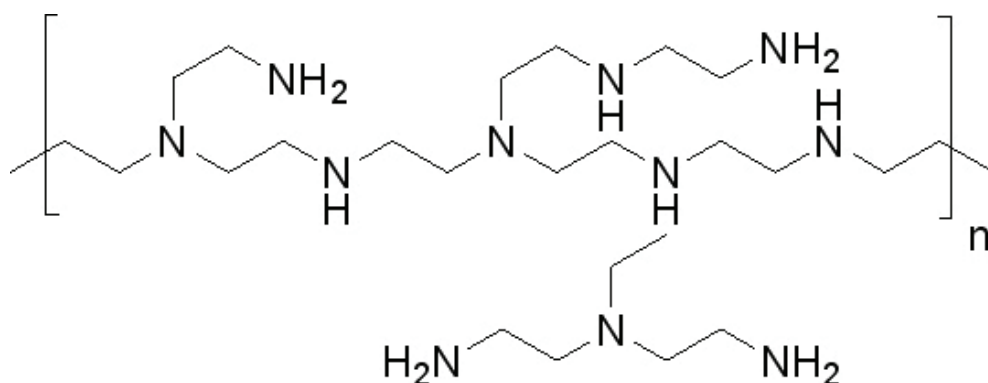


Figure 1.6 Chemical structure of PEI

PEI has plentiful amine groups which can interact with metal ions, anionic polyelectrolytes, and negatively charged colloids. PEI could also in principal be used as a reductant in the preparation of metal nanoparticles. For example, Sun et al⁶³ prepared PEI-protected gold nanoparticles by heating an PEI/HAuCl₄ aqueous solution. In their experiment, PEI served both as reducing agent and protective agent. Different initial molar ratio of PEI to gold leads to the

formation of dispersed nanoparticles, quasi one-dimensional aggregates of nanoparticles or bulk metal deposits. Moreover, the growth kinetics of nanoparticles could be tuned by changing the initial molar ratio of PEI to gold. Tan *et al*⁶⁴ used branched polyethyleneimine to reduce silver nitrate under UV irradiation for the synthesis of positively charged silver nanoparticles. Their results showed that Ag nanoparticle size and distribution can be controlled by the molar ratio between PEI and silver ions and/or by the molecular weight of the PEI chains. PEI stabilized Ag nanoparticles demonstrated superior SERS sensitivity, therefore, and promising for SERS-based detection of anions in aqueous solutions.

PEI is a polyamine, thus a weak polybase. Ionization occurs in aqueous solutions at high ionic strength, so it shows overall positive charge. Because of its cationic character, PEI readily attracts with other negatively charged species, causing charge neutralization. These properties have been widely utilized in self-assembly to form super-structures⁶⁵⁻⁶⁷.

1.3 Chemical and photoreduction methods to synthesize nanoparticles

Special attention has been paid to metal and metal oxide nanoparticles due to their unique electrical, magnetic, optical and catalytic properties^{68, 69}. They have great potential for a variety of significant technological applications, such as catalysis, labeling of biological samples, biological imaging, hydrogen storage, magnetic information storage, etc⁷⁰⁻⁷². To exploit the nano size metal and metal oxide particles, research has focused on the synthesis methodologies. The two representative technique which have been most used include modern versions of established chemical reduction of metal salts/complexes and photochemical methods⁷³. These methods are used in this work, and are discussed and compared below.

1.3.1 Chemical reduction

Chemical reduction methods are the most extensively practiced methods to prepare nanoparticles in aqueous or organic media because of their simplicity and availability. Metal precursors are normally metal salts. There are many reducing agents, such as: borohydrides, hydrazine hydrate, sodium cyanoborohydride, aluminohydrides, hypophosphites, formaldehyde, oxalic salts, and tartartic acids etc.⁷⁴ In some cases, easily oxidized solvents can also be used as reducing agents, such as ethanol. The alcohol reduction process is a simple method for the production of transition metal nanoparticles which are often stabilized by polymers, for example, poly(vinyl alcohol), poly(vinylpyrrolidone), and poly(methyl vinyl ether)⁶³.

NaBH_4 is the most used reducing agent in non-reducing solvents⁷⁵. Using NaBH_4 for the synthesis of aqueous suspensions of metal nanoparticles is a well established method. Various metal nanoparticles⁷⁶⁻⁷⁹, including platinum, gold, silver, copper, and alloys have been prepared using NaBH_4 because of its high redox potential compared to the standard reduction potential of these metal ions. The reduction is a complex process and depends on temperature, pH and diffusion and sorption characteristics. The reduction mechanism has been well studied⁸⁰. The process begins with the formation of bridge bond M-H-B, then redox process happen with transfer electron from H^- to metal ions and the breakage of B-H bond to give borane. In the last step, borane will hydrolyze and decompose on the surface of metal nanoparticles.

Hydrogen is another effective reducing agent for metal nanoparticles synthesis. With hydrogen, hydrosols of Pd, Ru, and Pt stabilized by PVA were successfully produced^{22, 81, 82}. For example, Moiseev synthesized Pd nanoparticles with uniform size by using hydrogen as a reducing agent^{83, 84}.

There are several advantages of chemical synthesis using reducing agents in aqueous phase: production of high concentrations of metal nanoparticles, the conditions are mild (generally at room temperature and regular pressure). They also show some disadvantages, such as, broad size distribution, and relatively poor stability.

Chemical methods can also be used in organic solvents with organic or organometallic reagents. For synthesis in organic phases, surfactants are used as stabilizers to control particle size. For example, the reaction of chloroauric(III) acid and dodecanethiol with THF solution of 2-propylmagnesium bromide produces thiol-capped gold nanoparticles⁸². The nanoparticles obtained by this method are spherical with an average diameter of 5.5 nm. The size, size distribution and surface state of these nanoparticles are better controlled in organic solvent than when they are produced in aqueous.

1.3.2 Photoreduction methods

While chemical reduction is an effective method for the formation of nanoparticles, there are challenges in synthesizing finely and homogeneously dispersed nanoparticles of electropositive metals. In chemical methods, strong reducing agents are used, and inhomogeneity in their distribution can alter rate of nucleation and growth resulting in polydisperse particles. This should be avoided in the preparation of monodisperse nanoparticles. One solution to the problem was the use of strong reducing agents with slow kinetics^{85, 86}. But this leaves the issue of byproducts of the redox reaction contaminating the products. Photoreduction was proposed to overcome these issues⁸⁷.

The photoreduction method to produce nanoparticles is a strategy which uses the reduction of metal salts by photochemically produced reducing agents such as solvated electrons or free

radicals. Photoreduction of metal ions in solution is most widely used for synthesizing noble metal nanoparticles⁷³. These kinds of reactions are carried out in water, alcohol or organic solvents⁸⁸. Without stabilizing agents, the nanoparticles produced by photoreduction also aggregate as chemical reduction methods. Light stimulated aggregation was observed⁸⁹. It was agreed that the aggregation was caused by the appearance of light-generated particles with opposite charges as a result of photoemission.

In photoreduction processes, a large number of nucleation sites are produced homogeneously and instantaneously, favoring for the formation of monodisperse nanoparticles. The use of excess reductant is avoided, making it a clean and effective method. The chemical compatibility of added reducing agents is not an issue. Pt, Au, Ag nanoparticle has been formed by UV irradiation in polymer solution or surfactant solutions⁹⁰⁻⁹². Kapoor⁹³ synthesized Cu nanoparticles by photochemical method in presence of PVP or gelatin as stabilizing agents. Murakata⁹⁴ reported on the preparation of Cu nanoparticles in water/ethanol solution with TiO₂ as catalysts.

1.4 Assembly of nanoparticles on surfaces

Although the synthesis and stabilization of monodisperse nanoparticles have been well studied, it is still a challenge to assemble the nanoparticles into predefined and sophisticated patterns of precisely controlled geometry. The assembling of nanomaterials into complex two and three-dimensional ordered structures offers a special pathway for design of materials that have potential applications in optical and microelectronic devices, chemical and biosensor technology, optical energy transport, and in advanced spectroscopy^{95,96}, such as in light emitting diodes, full color displays, electronic switches, biological label, high density recording media,

and surface-enhanced Raman scattering⁹⁷. The ability to direct the position of nanoparticles onto a substrate would be an advantage in these kinds of applications. A number of promising techniques have been proposed to fabricate these kinds of complex assemblies, including the manipulation of nanoparticles using lithography, sedimentation, capillary forces, flow fields, electrophoretics, dip-coating, physical confinement, and microfluidics⁹⁸. Many forces and interactions can be used to direct assembly, including hydrogen bonding, Columbic forces, hydrophobic/hydrophilic interaction, and biospecific interactions¹⁸. The essential feature of these methods is fabrication of surface functionality for templating and directing nanoparticles assembly.

1.4.1 Adsorption of nanoparticles on surfaces

Nanoparticles can be adsorbed on various substrates. There must be some force to hold nanoparticles on the substrate as mentioned above. So the substrate is normally decorated with various chemical function groups. For glass, silanization is a typical method. Silanized glass substrates have chemical groups that are capable of binding of nanoparticles either by electrostatic interactions or covalent bond⁹⁹. Figure 1.7 shows this process. When a silanized glass substrate is put in a nanoparticle solution, the nanoparticles will bind to the glass surface and form a saturated monolayer over a period of time. For conductive substrates, there is a special electrophoretic method¹⁰⁰. When the colloidal nanoparticles are subjected to a dc electric field, they receive an external force induced by electric field which cause them move to the electrode with opposite charge quickly. As time increases, more particles reach the anode surface to form arrays¹⁰¹. With electrophoretic method, very regular, close-packed monolayer structures can be formed, but the nanoparticles are not truly bond to the surface and thus the structures are not very stable¹⁰².

Polyelectrolyte assisted deposition of nanoparticles has been the subject of a large number of investigations in recent years¹⁰³⁻¹⁰⁵. The most widely used polyelectrolytes are Poly(diallyldimethylammonium chloride) (PDDA), PEI, poly(acrylic acid) (PAA). The construction of polyelectrolyte film on various substrates is well known. This is a very general method, and many kind of metal nanoparticles have been assembled on the substrates^{106, 107}. But with this kind of method, monolayer nanoparticles tend to show less coverage and are less organized because the charges prevent them from forming dense structures. Langmuir-Blodgett and other surface tension driven techniques have also been used for the assembly of nanoparticles by virtue of their high degree of control over nanoparticle order and density over large areas, although they are not suitable for mass production or on non-flat substrates¹⁰⁸⁻¹¹².

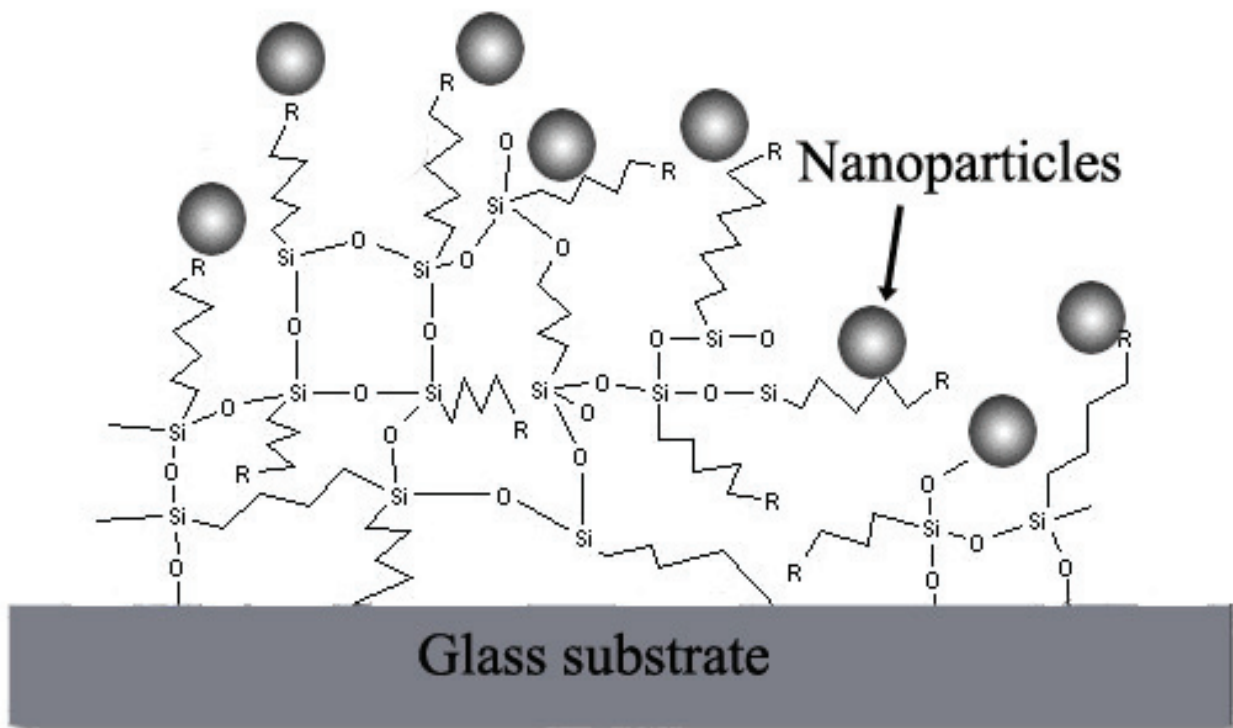


Figure 1.7 Schematic representation of nanoparticles assembled on silanized glass.

(Adapted from Ref 99)

1.4.2 Lay-by-layer (LBL) assembly

In order to increase the amount of nanoparticles on the substrate, multilayer assembly is used. To form multilayer assembly, a surface monolayer must be functionalized. Multilayer assembly can form complex structures with different types of nanoparticles to realize designed functional materials. Polyelectrolyte assisted deposition is an effective method to form monolayer assemblies of nanoparticles. If this procedure is repeated, multilayer assembly will be fabricated. This is called layer-by-layer assembly. For example, Figure 1.8 shows negatively charged gold nanoparticles assembled in multilayer configuration using positively charged PEI¹¹³. Charge on nanoparticles causes them adsorb onto the polymer (and vice versa), which allows multilayer assembly. LBL has three major advantages: simplicity, universality and nanoscale thickness control. This technique is very simple and no sophisticated instruments are needed. Almost all aqueous dispersions of polymers, nanoparticles, oligomers can be assembled. In each step, only one layer is deposited, so it is possible to create any sequence of nanoparticles monolayers^{114, 115}.

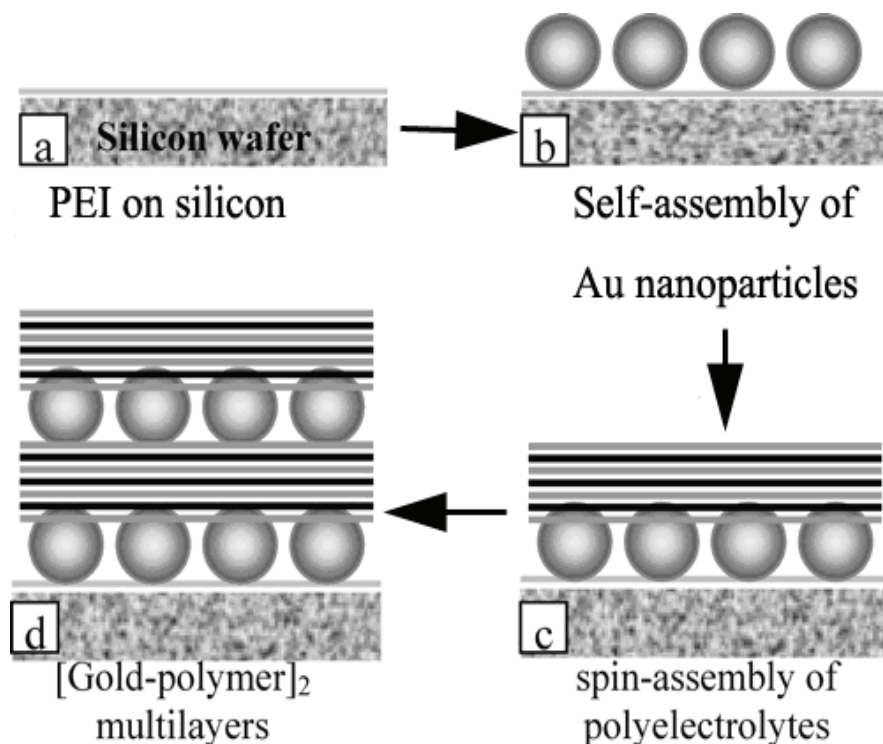


Figure 1.8 Scheme of fabrication of gold nanoparticle–polyelectrolyte multilayers

(a) Assembly of PEI on the silicon wafer; (b) gold nanoparticle monolayer assembly by adsorption on the PEI surface; (c) Au/(PAH–PSS)_nPAH multilayers fabricated with SA-LBL assembly of polyelectrolyte layers; and (d) assembly of the [Au/(PAH–PSS)_nPAH]₂ multilayer structure.

(Adapted from Ref 113)

1.4.3 Patterning of nanoparticles arrays

Patterning of nanoparticles arrays is very important for the use of nanomaterials in electronics, data storage or sensors. Various methods have been designed to fabricate patterns of nanoparticles arrays⁹⁶. Fabrication of surface pattern functionality were realized by template surface with different regions of hydrogen bonding, charged, hydrophilic, hydrophobic and other specific groups in which nanoparticles with complementary functionality can deposit onto the corresponding regions⁸⁹.

Physical engineering methods are intuitive ways which use microscopic tools such as STM and AFM tips to move the particles to required positions^{116, 117}. Mass production and cost is a major barrier for this method¹¹⁸. Lithography is a well-known technique used to create pattern structures¹¹⁹. Some researchers have successfully used this technique to fabricate nanoparticle patterns. In this method, substrates are functionalized and exposure to the lithographic medium forming the patterned substrates, then standard nanoparticles assembly procedure are used to create nanoparticle patterns.

Soft lithography is a method to fabricated pattern structures, which can be used to create patterning of nanoparticles arrays^{120, 121}. A patterned poly(dimethylsiloxane) (PDMS) stamp is often used. Figure 1.9 illustrates the preparation procedure for casting PDMS replicas from a master having relief structures on its surface. The master, fabricated by standard lithography techniques is filled with liquid PDMS prepolymers. After curing, PDMS is peeled from the master. Using the PDMS stamp, various polyelectrolyte and nanoparticle inks¹²² can be printed on to the substrate introducing a pattern of functionality, as shown in Figure 1.10 . In this technique, patterns with feature sizes as small as 15 nm over areas as large as $\sim 1 \text{ m}^2$ can be produced. The elasticity of the PDMS stamp facilitates conformal contact between the stamp and the substrate, which makes it possible to pattern non-planar surfaces (such as porous, rough or curved surfaces).

Micromolding in capillaries (MIMIC)¹²³ is a technique that uses a patterned layer of PDMS in contact with a surface to form a network of microchannels where nanoparticles form ordered arrays. In this method, the PDMS stamp is brought into conformal contact with a solid substrate, and the nanoparticle solution is placed at the edge of the PDMS layer (Figure 1.11). The solution is drawn into the channels by capillary action, and the solvent is subsequently

evaporated to produce pattern structures. By peeling the stamp away carefully, micropatterned arrays of nanoparticles is left on the substrate surface.

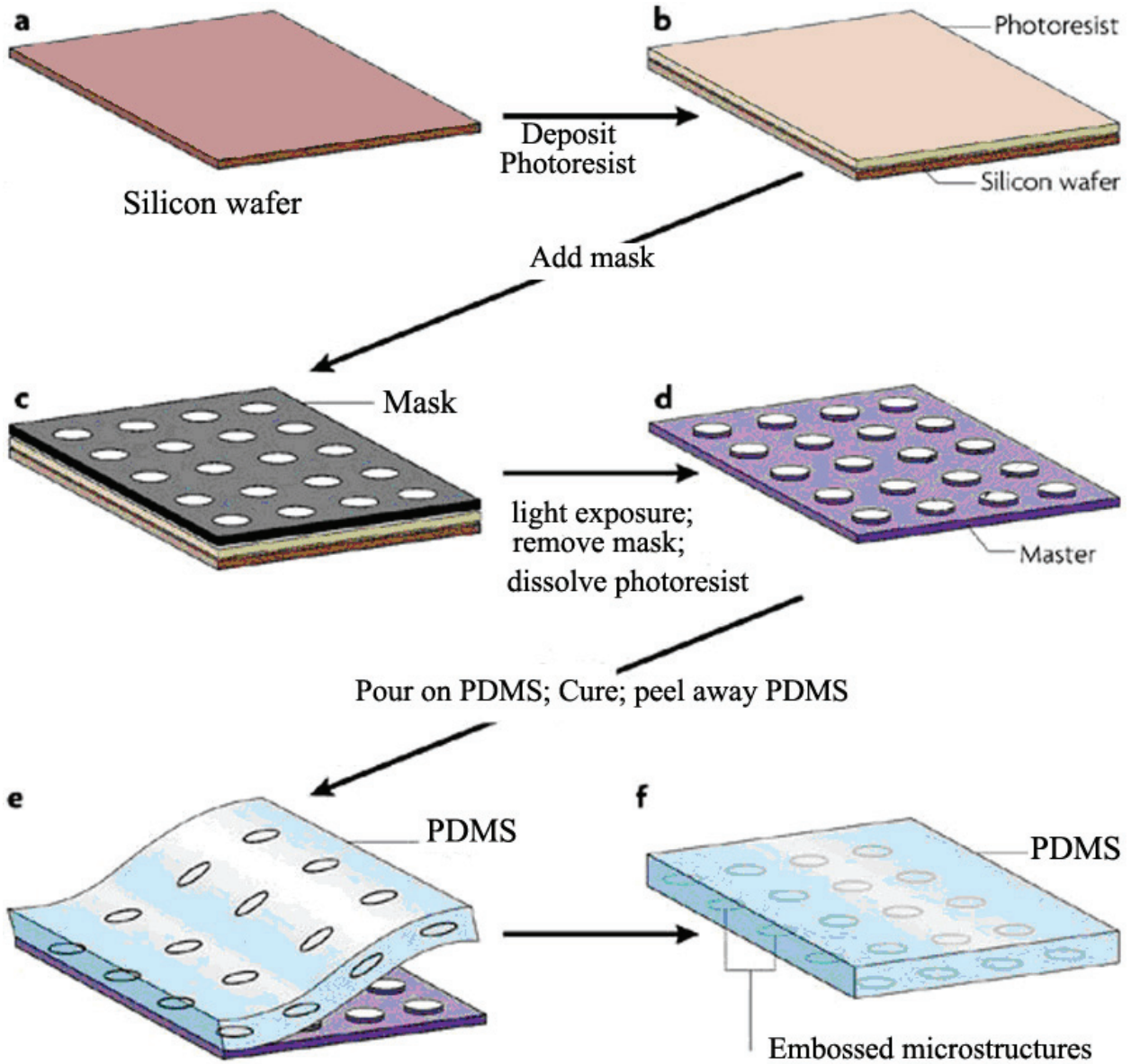


Figure 1.9 The preparation procedure of PDMS stamp structures.
(Adapted from Ref 123)

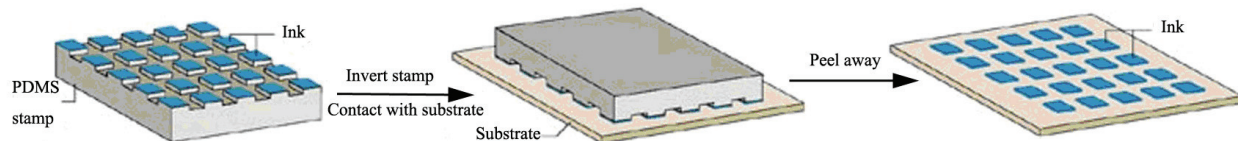


Figure 1.10 Microcontact printing.
 (Adapted from Ref 123)

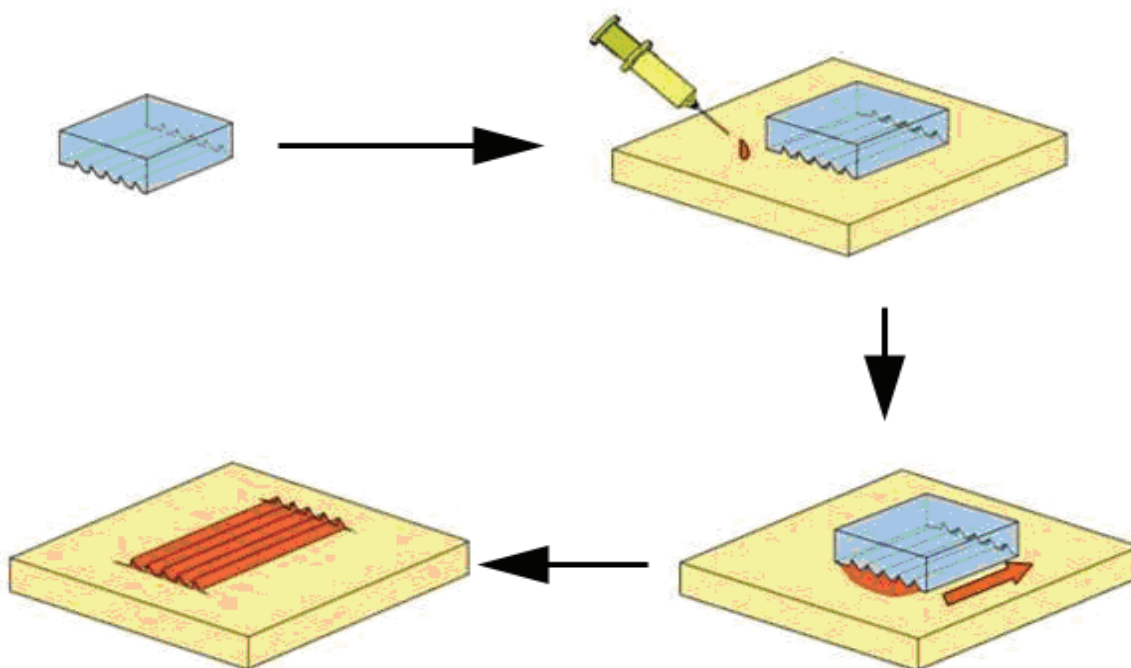


Figure 1.11 Schematic of MIMIC used to fabricate pattern structures.
 (Adapted from <http://vpd.ms.northwestern.edu/memberpages.asp?url=members/Zixiao/Project%20Q%20and%20A.htm>. Accessed on Aug 19, 2009)

1.5 Objectives of this study

Polymer mediated nanoparticles represent one of most the important nanomaterials in current nanotechnology. The understanding of polymer mediated nanoparticles and how their properties are affected by synthesis could play a crucial role in applying these nanomaterials into technological applications. This dissertation explores polymer templated pathways to synthesize polymer-encapsulated nanoparticles which serve as a tool to gain both fundamental and application oriented information about polymer templates and nanoparticles.

The first objective of this study was to synthesize novel polymer encapsulated nanomaterials. Two kinds of polymers were chosen for this study: dendrimer and hyperbranched polyelectrolytes. Several metal and metal oxide nanoparticles were chosen, such as Pt, FePt, Co_3O_4 , and Fe_3O_4 . With this platform, the interaction of metal ions with polymer, and the reaction mechanism was studied.

The polymer encapsulated nanomaterials were expected to have special properties. Control of structures of metal parts, especially in bimetallic nanoparticles is known to change the properties of nanoalloys. The second objective was to investigate the chemical, catalytic magnetic and other properties of polymer encapsulated nanomaterials which are influenced by synthesis.

The third objective was to explore potential applications of these kinds of polymer encapsulated nanomaterials, such as in fuel cells and magnetic data storage materials.

The fourth objective of this study was to build highly ordered assemblies of polymer mediated nanomaterials by MIMIC technique. Methods to increase pattern resolution were studied.

1.6 Overview of this dissertation

In the first part of this dissertation (Chapter 1), the dissertation begins with introducing the background of nanoparticles including their novel properties, synthesis methods, stabilization problems, polymer stabilizers, and their assembly together with a survey and evaluation of related work. Then a brief motivation and overview of this dissertation is given.

The second part (Chapter 2) introduces the experimental techniques and instruments used in this research.

The third part of this dissertation (Chapter 3, 4) involves the photochemical method used to prepare hyperbranched PEI mediated nanoparticles. In chapter 3, polymer-mediated platinum nanoparticles were synthesized by photoreduction in the presence of PEI. The formation process of the Pt nanoparticles and the formation mechanism is discussed. Both chemical and electrochemical catalysis activity are carefully studied, and it is shown that PEI mediated Pt nanoparticles exhibit very high catalytic activity. In Chapter 4, a photochemical method was used to synthesize PEI-mediated Co_3O_4 nanocrystals. High quality rod-shape Co_3O_4 nanocrystals were synthesized at room temperature and ambient pressure. In this process, PEI was used as a stabilizer, leading to the growth of nanocrystals to nanorods. The research result demonstrates that the morphology of nanorods is dependent on the molar ratio of PEI to metal precursor. The shape, size, and morphology and crystal structure of the Co_3O_4 nanorods were studied. The possible formation mechanism is discussed.

The fourth part (Chapter 5, 6) presents studies on the using of chemical methods to prepare dendrimer mediated alloy nanoparticles and multicomponent microspheres. In chapter 5, PAMAM-OH dendrimers were used as templates, and FePt nanoparticles with narrow size

distribution were prepared by a chemical reduction method at room temperature in aqueous solution. The structural and magnetic properties of the as-made and annealed samples were characterized. In Chapter 6, PAMAM dendrimers act as templates in which metal ions are coordinated, and NaBH_4 is the reductant. CoPt nanoparticles were synthesized in aqueous solution. The dendrimer mediated CoPt nanoparticles were subsequently encapsulated in silica spheres. These silica spheres show interesting magnetic properties. The relationship between synthesis condition and the magnetic properties of silica multicomponent spheres were studied.

Preparation and assembly of PEI mediated Fe_3O_4 nanoparticles are demonstrated in part five (Chapter7). A scalable technique for controllable two-dimensional ordered assembly of magnetite nanoparticles at the individual particle level is presented. PEI mediated Fe_3O_4 were first synthesized by a chemical method. Polyethyleneimine coating of the magnetite nanoparticles can effectively prevent aggregation. PEI was used as stabilizer and then the charge on the PEI was used to direct particle assembly. Individual magnetite nanoparticle arrays were formed by capillary filling technique induced by a magnetic field. Individual magnetic particles were patterned on silica wafers which doubled the resolution of PDMS pattern.

Chapter 8 summarizes this dissertation and gives future directions of these studies.

CHAPTER 2 Experimental

2.1 Chemicals

Poly(amidoamine) (PAMAM) dendrimers were used in this work. Hydroxyl-PAMAM dendrimers having an ethylenediamine core were provided as 10% methanol solutions by Aldrich, Inc. The dendrimer solution was put in vacuum, so that methanol can be evaporated before use. 200-proof absolute ethanol was obtained from Adapter Alcohol and Chemical Co. H₂SO₄ (concentrated, Fisher Scientific), H₂O₂ (30%, Fisher Scientific), and Si wafer (Wafer World, Inc.) were used as received. Ultrapure deionized (18 MΩ·cm Milli-Q, Millipore) water was used for all sample preparations and adsorption experiments.

Other chemicals used in this work are discussed in particular chapters.

2.2 Substrates

Silicon substrates were used for nanoparticle assembly, X-ray photoelectron spectroscopy (XPS) and XRD experiments. Before use, silicon wafers were cleaned with piranha solution (H₂SO₄/H₂O₂=3:1) by boiling the solution 30 min to 1h. (Piranha solution is very dangerous, with the majority of its components acidic and highly corrosive. It must be handled with extreme care.) Then the silicon wafers were cleaned with distilled water.

PDMS stamps were rinsed with methanol and distilled water, dried in a flowing stream of N₂ gas, and then cleaned in a low-energy ozone cleaner for 10 min (Jelight Company, Inc., model 42) immediately prior to use.

2.3 Techniques

2.3.1 Ultraviolet-Visible Spectroscopy (UV-vis)

UV-Vis involves the spectroscopy of photons in the UV-visible region which corresponds to electronic excitation. A UV-vis spectrophotometer scans the wavelengths in the visible and the UV region. It produces a plot of absorbance against wavelength, which is called a UV-vis spectrum¹²⁴. The UV-vis spectral range is approximately 190 to 900 nm. UV-vis absorption spectroscopy obeys Beer's Law (equation 2.1), where the absorbance (A) of a molecule is a function of the molar absorptivity (ϵ), the path length (l), and the concentration (c). P is the power of light after it passes through the sample and P_0 is the initial light power.

$$A = \epsilon l c = -\log (P/P_0) \quad (2.1)$$

UV-vis is a routine analytical technique for the characterization of the complexation between polymers and transition metal ions, the formation of the clusters upon reduction of metal-ions as well as the size and band structure of clusters^{125, 126}. Due to the excitation of plasma resonances or interband transitions, nanoparticles may exhibit absorption bands or broad regions of absorption in the UV-vis range. Nanoparticles, such as copper, gold, and silver, have distinct absorption bands in the visible region which have bright color^{127, 128}. However, platinum only exhibits broad absorption continua according to Mie theory¹²⁹.

In this dissertation, absorption spectra were recorded with a Cary 50 UV-vis spectrometer. The optical path length was 1.0 cm and deionized water was used as a reference for all measurements.

2.3.2 Fourier Transform Infrared (FT-IR)

FT-IR is the preferred method of infrared spectroscopy. Infrared spectroscopy detects the vibrational characteristics of chemical functional groups in a sample. By interpreting the infrared

absorption spectrum, the chemical bonds in a molecule can be determined¹³⁰. It is a straightforward tool to identify organic compounds¹³¹.

In this study, Fourier transform infrared spectra were acquired on Nicolet 560 Magna IR spectrometer, which was equipped with a liquid nitrogen cooled mercury cadmium detector. Samples were prepared by dropping chemicals onto KBr crystals. Background of KBr was collected and subtracted. The number of scans was set at 200. The relative humidity inside of the sample box was approximately 2%. Samples were allowed to purge inside the IR spectrometer for 20 min before analyses.

2.3.3 Raman Spectroscopy

Raman spectroscopy is a another spectroscopic technique used to study vibrational, rotational, and other low-frequency modes in a system¹³². Raman spectroscopy yields similar, but complementary information compared with infrared spectroscopy¹³³. In this technique, when the sample is illuminated with a laser beam, light of a known frequency and polarization is scattered from a sample. Raman scattered light is frequency-shifted with respect to the excitation frequency. Raman shift corresponds to excitation energy of the sample (such as vibrational energy transition in a molecule).

The Raman measurements in this dissertation were obtained using a LabRam HR800 UV spectrometer (Horiba Jobin-Yvon) with a 633 nm laser line.

2.3.4 Transmission Electron Microscopy (TEM)

TEM is a tool to characterize the size, shape and crystal structure of nanoparticles, and can provide a real space image of the atomic distribution in the nanocrystal and its surface^{134, 135}. TEM can also give chemical information at a spatial resolution of less than 1 nm, and this allows

direct identification the chemistry of single nanoparticles¹²⁹. As shown in Figure 2.1, TEM is composed of an electron source, an electromagnetic lens system, a specimen stage, and the imaging system. The electron gun is the source of electrons. A monochromatic electron beam is generated by LaB₆ thermionic emission source or a field emission source. A condenser lens is used to form coherent and narrow beam. The condenser aperture is used to remove the high-angle electrons. The focused electron beam then interacts with the sample. The objective lens are the key part of TEM, determining the resolution of TEM image. High angle electrons can be blocked by the objective aperture, enhancing the contrast. Then electrons pass through magnification system which consists of intermediate lenses and projection lenses. Finally, the TEM image can be formed on CCD or phosphor screen.

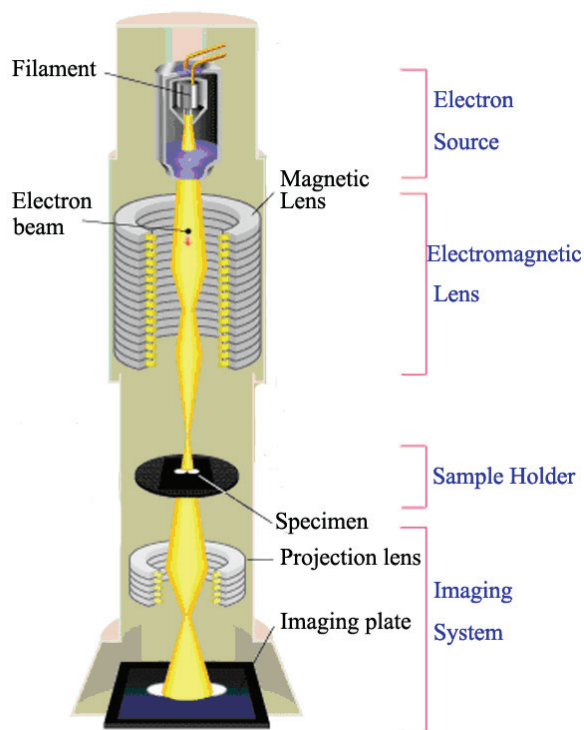


Figure 2. 1 The schematic outline of a TEM

(Adapted from http://www.hk-phy.org/atomic_world/tem/tem02_e.html. Aug. 18, 2009)

The TEM can be operated in high resolution mode (HRTEM)^{136, 137}. This mode allows the imaging of the crystallographic structure at atomic scale. Because of its high resolution, it is a powerful tool to study nanoscale properties of crystalline materials. In this dissertation, the crystallographic structure of polymer mediated nanoparticles is characterized by HRTEM. Unlike conventional TEM, HRTEM images are formed from a number of diffracted beams. This allows phase-contrast imaging, which is necessary to construct an image of the crystal lattice. So HRTEM image formation relies on phase-contrast, not absorption by the sample.

In this work, TEM images and selected area electron diffraction (SAED) patterns were obtained using a FEI TECNAI F20 microscope with an accelerating voltage of 200 kV. Samples were prepared by placing a drop of dilute solution on the grid, which was placed on a paper towel, and allowing the water to evaporate in air. Standard carbon-coated 400-mesh and 300-mesh copper grids (Electron Microscopy Sciences, Hatfield, PA) were used throughout the study.

2.3.5 Scanning Electron Microscope (SEM)

Scanning electron microscope gives the information about a sample's surface topography, composition and other properties such as electrical conductivity¹³⁸. A beam of high-energy electrons impinging on the surface produces secondary electrons, back scattered electrons, characteristic x-rays, specimen current and transmitted electrons¹³⁹. With suitable detectors, these signals can be collected. Generally, secondary electrons are used to form images of a sample surface, which can reach a resolution about 1 nm. Because the signals come from interactions of the electron beam with atoms at or near the surface of the sample, it is a surface-specific technique.

Back-scattered electrons are electrons that are scattered from the sample due to elastic scattering. The intensity of the back-scattered electrons signal is strongly related to the atomic number of the sample. Therefore, BSE images can provide information about the elemental distribution in the sample. EDS (see below) can be also equipped on SEM to get the composition information.

In this study, a Philips XL30 SEM was used. In most cases, it was operated at 20kV. Samples were prepared on silicon wafers. Carbon conducting tape was used to fix the silicon wafers on sample holder.

2.3.6 Energy Dispersive X-ray Spectroscopy (EDS)

Energy dispersive X-ray spectroscopy (EDS, also called EDX) in TEM is a very useful technique for performing microanalysis, particularly of heavier elements¹⁴⁰. In TEM, a focused electron beam interacts with the atoms in a sample. The electron beam displaces electrons in the sample, and the resulting vacancies are filled by electrons from higher energy shells; energy lost during these transitions is emitted as X-rays, as shown in Figure 2.2. X-rays emitted from atoms are characteristic of the elements and the intensity distribution represents the thickness-projected atom densities in the samples. Measuring the X-ray spectrum allows identification of the sample composition¹⁴¹. Since the electron beam in TEM can be as small as 1 nm, the composition of one individual nanoparticle can often be tested¹⁴². EDS also has multiple mapping option to generate the elemental distribution information in samples.

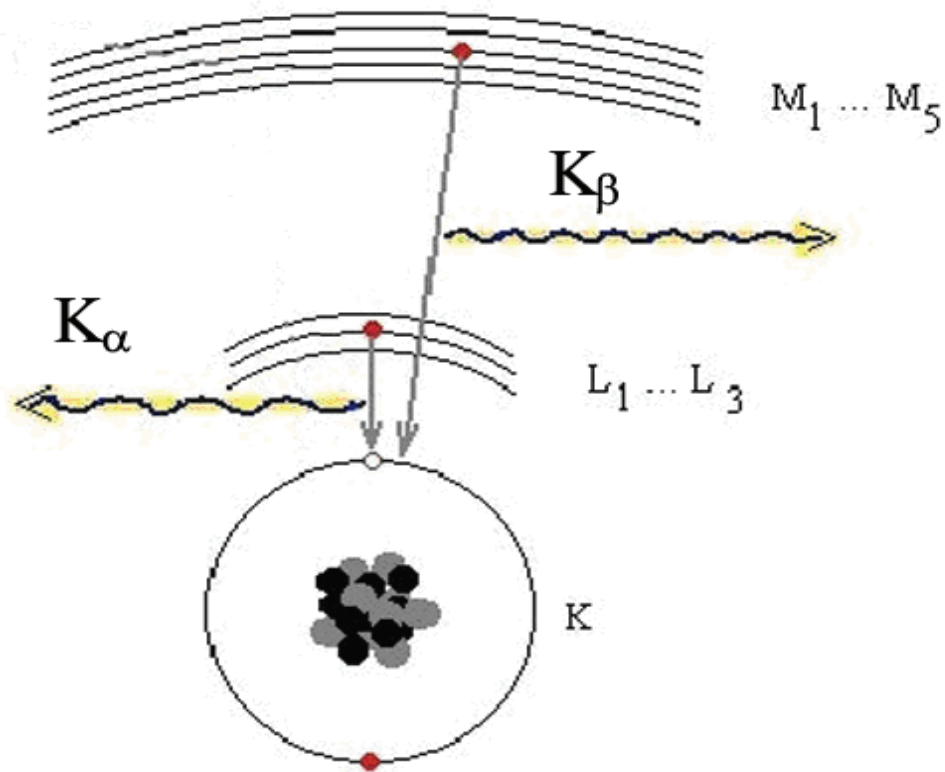


Figure 2. 2 Production of characteristic EDS radiation.

(Adapted from <http://microanalyst.mikroanalytik.de/info1.phtml>. Accessed On Aug. 20, 2009)

2.3.7 X-ray Photoelectron Spectroscopy (XPS)

XPS, also called electron spectroscopy for chemical analysis (ESCA), is a surface analytical technique commonly used to determine elemental composition and chemical state of the surface elements¹⁴³⁻¹⁴⁵. If X-rays impinge on the sample (as shown in Figure 2.3), the energy ($h\nu$) overcomes the work function (ϕ) and binding energy (BE) of the electron, inner-shell orbital electrons will be ejected (Figure 2.4). This process can be expressed by:

$$h\nu = BE + KE + \phi \quad (2.2)$$

Here, KE is the kinetic energy of ejected photoelectron; binding energy (BE) is the energy required to remove the electron from its original atomic orbital to vacuum level; work function (ϕ) is energy needed to move an electron from the Fermi energy level into vacuum. After the photoelectron is ejected from its orbital, the atom will relax by either fluorescence or Auger electron emission. The kinetic energy of the photoelectron can be measured by a hemispherical electrostatic energy analyzer. By convention, spectra as a function of binding energy are collected. The characteristic binding energy associated with each core atomic orbital is unique for every element. Therefore, every element has a set of characteristic peaks in the photoelectron spectrum. The intensity of the peaks in photoelectron spectrum is related to the concentration of the element within the sample volume. So, the XPS technique is also capable of yielding quantitative analysis. Because the electron binding energies are dependent on the chemical environment of the atom, the binding energies exhibit small chemical shifts due to interaction of the core electron with valence electrons and surrounding atoms. Thus XPS is also useful in identifying the chemical state and ligands.

In this study, XPS analysis was used to investigate chemical states and composition before and after reduction of polymer mediated particles. XPS analyses were made using a Kratos Analytical Axis 165 system which was equipped with a monochromatic Al K_{α} source (1486.6 eV). Survey scans were recorded at 160 eV pass energy, 1.0 eV/step; high resolution scans were recorded at 80 eV pass energy, 0.1eV/step. The samples for XPS were prepared by depositing several drops of particle dispersions on silicon substrates followed by evaporation of the solvent.

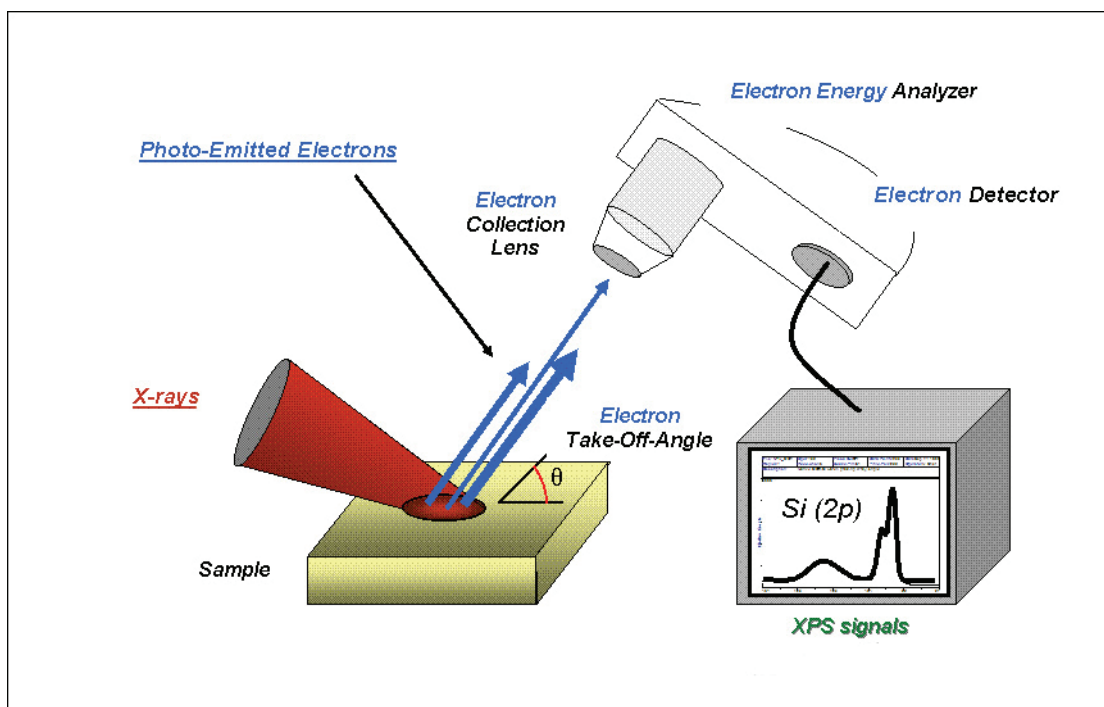


Figure 2.3 A schematic of XPS.

(Adapted from http://en.wikipedia.org/wiki/X-ray_photoelectron_spectroscopy)

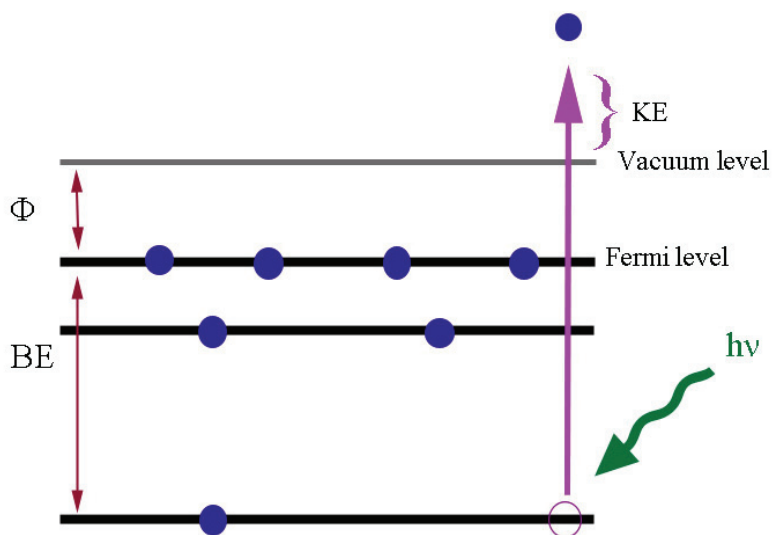


Figure 2.4 Energy level diagram of XPS process

2.3.8 X-ray Diffraction (XRD)

XRD is a convenient technique for characterizing the crystallographic structure and phase of materials¹²⁹. The scattered intensity of an X-ray beam hitting a sample is observed as a function of incident angle. The directions and intensities of scattered X-ray are related to the structure of samples and the intensities also depends on the sizes and shapes of the samples¹⁴⁶. Figure 2.5 illustrated the principle of XRD. When X-rays impinge on the sample, the path difference between two waves is equal to $2d\sin(\theta)$. For constructive interference between these waves, the path difference must be an integral number (n) of wavelengths:

$$n \times \text{wavelength} = 2d\sin(\theta) \quad (2.3)$$

Equation (2.3) is called the Bragg equation.

By scanning the angle of θ , the Bragg's Law conditions will be satisfied by different d -spacings in samples. Then, plotting θ and intensities of the resultant diffracted peaks of radiation produces a diffraction pattern. This pattern is characteristic of the sample. For acquired diffraction patterns, d -spacing can be calculated and peaks can be indexed according to Joint Committee on Powder Diffraction Standards (JCPDS) database.

A Rigaku D/Max-2BX X-ray diffractometer with monochromatic Cu K_{α} radiation ($\lambda = 0.15418$ nm) was used for this work. The operating voltage is 39 kV and current was 38 mA. Another XRD used in this study was Philips X'pert-MRD with Cu K_{α} radiation ($\lambda = 0.15418$ nm). The samples for XRD were made by dropping particle dispersions on silicon wafers (1×2 cm) followed by evaporation of solvents at room temperature.

To calculate the size of nanoparticles, Scherrer equation¹⁴⁷ can be used:

$$d = k\lambda/B \cos\theta \quad (2.4)$$

Here, λ is the wavelength of incident X-ray; d is the size of particles; k is a coefficient; B is the full width at half maximum of the peak, θ is the diffraction angle.

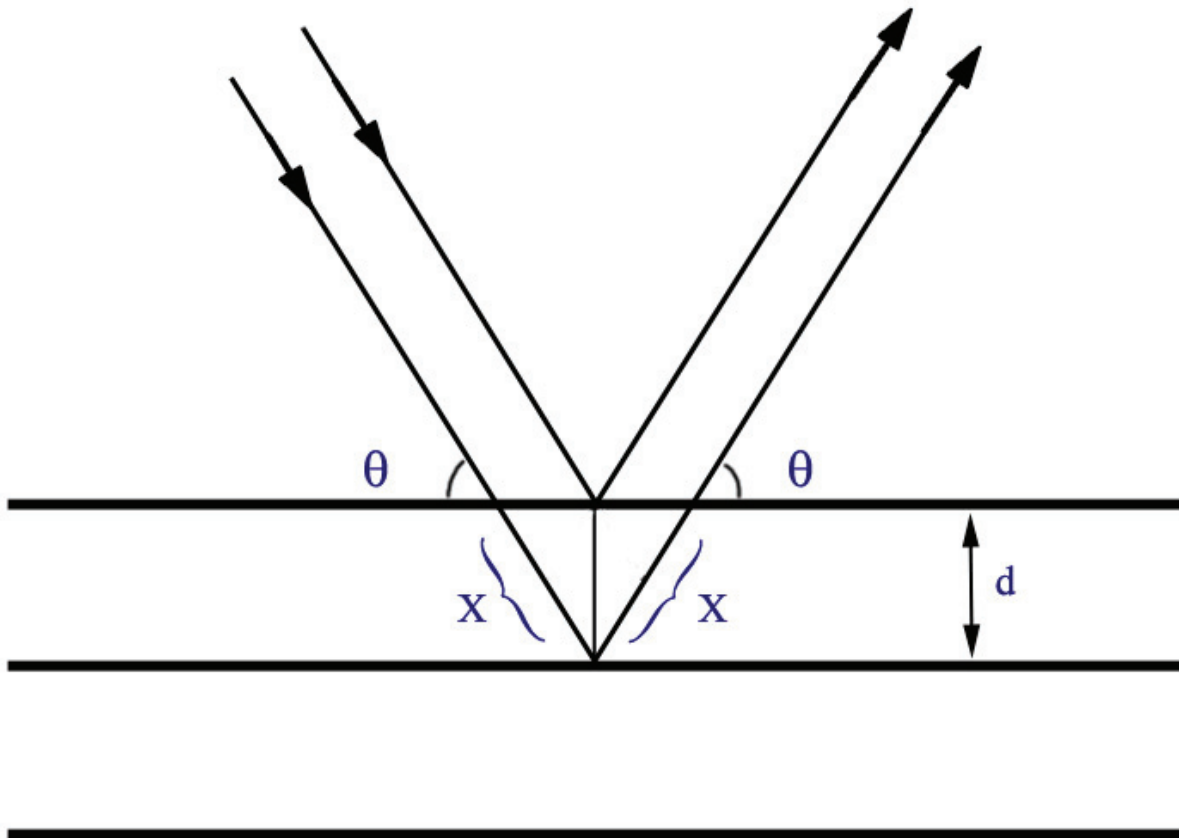


Figure 2.5 Schematic illustration of reflection of x-rays from two planes.

2.3.9 Atomic Force Microscopy (AFM)

AFM is a commonly used high-resolution scanning probe microscopy. It can produce a topographical map of surface features on the nanometer scale. AFM consists of a very small cantilever with a sharp tip (probe) at its end which is used as a probe to scan the surface of the

sample^{148, 149}. The tip is made of silicon or silicon nitride with a radius of curvature on the order of tens of nanometers. The cantilever is oscillated at a certain frequency. When the tip is brought into proximity of a sample surface, forces between the tip and the sample lead to changes in the amplitude of oscillation of the cantilever. A sensor detects this change and the position of the tip is adjusted according to the signal. In this way, the tip is rastered across the sample to collect surface topography information.

For this, a Nanoscope D-3000, Digital Instruments, Inc AFM was employed to test the surface topography of Fe₃O₄ arrays on the surface of silicon in tapping mode.

2.3.10 Alternating Gradient Magnetometry (AGM)

The magnetometry of the as-prepared nanoparticles was studied with a MicroMag 2900 alternating gradient magnetometer from the Princeton Measurement Corporation at room temperature using a parallel probe. In AGM¹⁵⁰⁻¹⁵², a sample is mounted on the end of a rod and put in a uniform dc field. A pair of coils produces a uniform field gradient over the region of the sample. Ac current in these coils produce a force on the sample. This force is proportional to its magnetic moment. A piezoelectric element is used to measure force and give voltage output. When operated near the mechanical resonance frequency, the signal can be amplified about 100 times, and a very high sensitivity can be achieved. The samples in this work were prepared on small piece of silicon wafer (3×3 mm).

2.3.11 Cyclic voltammetry (CV)

Cyclic voltammetry is an electrochemical measurement method. CV can rapidly provide information about the thermodynamics of redox processes and the kinetics of heterogeneous electron-transfer reactions^{153, 154}. CV also offers rapid location of redox potentials of

electroactive species. A three-electrode system is used to obtain stable voltammograms in CV. Current as a function of potential is measured. Figure 2.6 shows a CV setup. One of the three electrodes is the working electrode, which is typically made of platinum, gold, silver, or glassy carbon. This is the electrode at which the electrochemical phenomena (redox processes) being investigated are taking place. The second electrode is the counter or auxiliary electrode, which is often a platinum wire that serves to conduct electricity from the signal source through the solution to the other electrodes. The third electrode is reference electrode, whose potential is constant enough that it can be taken as the reference standard. The common used reference electrodes include standard hydrogen electrode (SHE), saturated calomel electrode (SCE) and silver chloride electrode. As shown in Figure 2.7, the electrode potential is changed linearly as a function of time. In the forward scan, a current peak can be detected which is responsible for analytes that can be reduced in the range of the potential scan. The current will increase when the potential approaches the reduction potential of the analyte, but then decreases because the concentration of the analytes is depleted near the surface of the electrode. If the reduction reaction is reversible, the deoxidation of the products can be observed when the applied potential is reversed. This data is then plotted as current vs. potential.

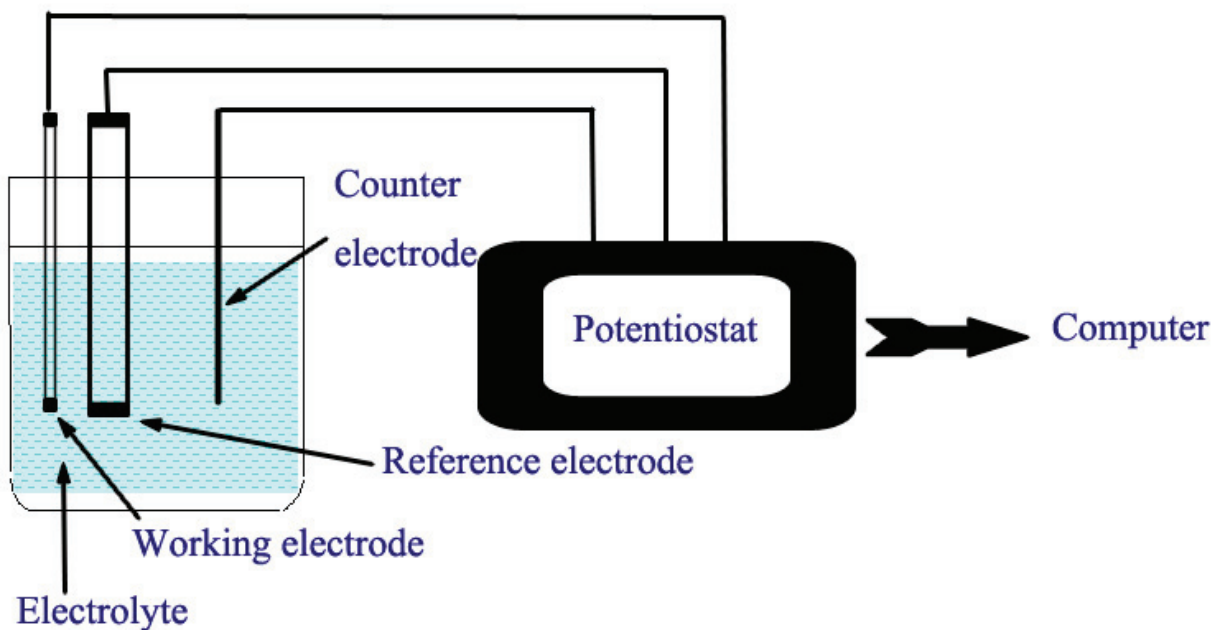


Figure 2.6 Schematic illustration of CV setup.

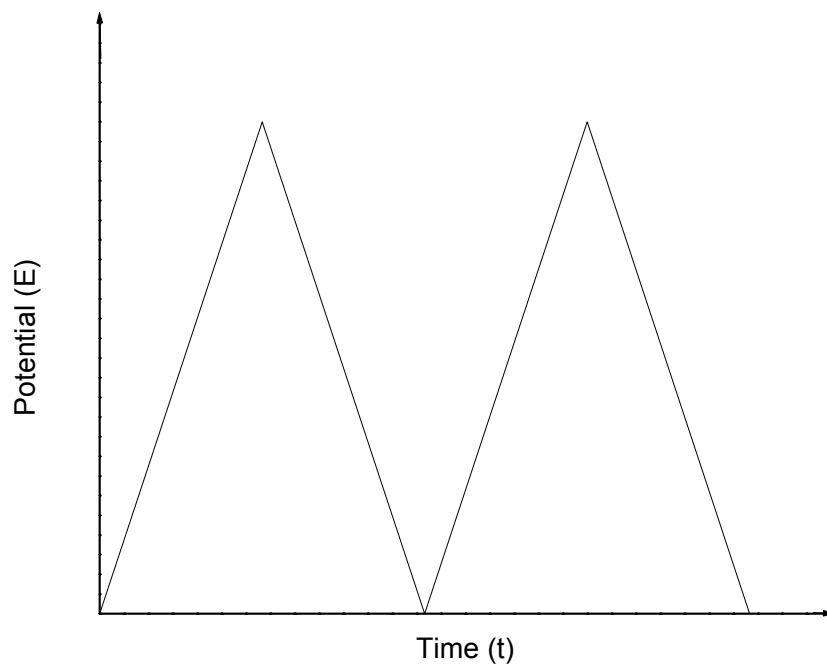


Figure 2.7 Cyclic voltammetry potential waveform.

In this work, all electrochemical measurements were performed in a conventional three-electrode cell at room temperature. A Pt wire was used as a counter electrode. An Ag/AgCl (saturated KCl solution) reference electrode was used for all electrochemical measurements, and all electrochemical potentials in the present study are given versus Ag/AgCl reference electrode. The working electrode was Pt coated glassy carbon electrode (diameter 3 mm). In order to minimize the effects of impurities during the measurements, the electrode was cycled in 1 M H₂SO₄ solution at 50 mVs⁻¹ between 0 and 1.2 V until reproducible cyclic voltammograms were obtained prior to any electrochemical measurements. Cyclic voltammograms and chronoamperometry were recorded using a computer-controlled CHI 660 electrochemical workstation (CH Instruments, Austin, TX). Hydrogen adsorption cyclic voltammograms were recorded in nitrogen protected 1M sulfuric acid aqueous solution. The solution was purged with nitrogen to deplete dissolved oxygen before the test. The region for hydrogen adsorption was used to estimate the electrochemical active surface areas. Fresh 1M H₂SO₄ + 2M CH₃OH was used in every methanol electro-oxidation methanol measurement to get reliable and reproducible results.

Glassy carbon electrodes were used as a substrate for the immobilization of Pt nanoparticles. The glassy carbon working electrode with a geometrical surface area of 0.07cm² was polished with 1μm and 0.05μm Al₂O₃ powders successively on nanocloth followed by sonication in deionized water. PEI/Pt NP solution prepared by UV irradiation was pipetted on to the surface of the glassy carbon electrodes. After water was evaporated overnight at room temperature, the PEI/Pt NP coating was irradiated for 1 hour in the Rayonet photochemical reactor. Then the electrode was washed carefully with deionized water before measurement.

CHAPTER 3 Synthesis and Catalytic Activity of Photoreduced Platinum Nanoparticles in Polyethylenimine Matrix

3.1 Synopsis

Monodisperse polymer-mediated platinum (Pt) nanoparticles were synthesized by photoreduction in the presence of polyethylenimine (PEI), a hyperbranched polymer. The formation process of the Pt nanoparticles was pursued by UV-Vis spectroscopy and the formation mechanism is discussed in this chapter. The morphology and size of the Pt nanoparticles were characterized by transmission electron microscopy (TEM). The catalytic activity of the platinum was evaluated by using UV-Vis spectroscopy to monitor the platinum-catalyzed reduction of 4-nitrophenol by sodium borohydride. Electrocatalytical properties of PEI mediated Pt nanoparticles (PEI/Pt NPs) have also been studied. The PEI/Pt NPs were immobilized on glassy carbon electrodes and electrocatalytical activity toward methanol oxidation reaction was investigated by cyclic voltammety (CV). PEI/Pt NPs exhibit very high catalytic activity for methanol oxidation reaction. PEI/Pt NPs on glassy carbon electrodes are also robust. They survive and show good tolerance to poisoning even after many cycles. Electrocatalytical activity of PEI/Pt NPs was also compared with that of other polymer mediated Pt nanoparticles. It shows better electrocatalytic activity than most others. The results indicate that PEI is a good capping, reducing agent and carrier to immobilize the nanoparticles on the electrode.

3.2 Introduction

With the recent surge in technological research and development, the use of platinum nanoparticles in optics, imaging, electronics, and as catalysts has dramatically increased¹⁵⁵. Pt nanoparticles are especially attractive for direct methanol fuel cells (DMFCs). DMFC using liquid methanol are promising candidates for the future power source to compete with the conventional batteries for portable electronic devices due to their high energy conversion efficiency, low operation temperatures, and low pollutant emission¹⁵⁶. In a DMFC, methanol and oxygen are combined electrochemically over catalysts to produce electrical current. Although progress has been made in the development of DMFCs, practical applications of DMFCs still face severe performance and durability challenges¹⁵⁷ because of poor electrocatalyst performance¹⁵⁸ of both anode and cathode reactions and crossover of methanol¹⁵⁹ from anode to cathode through the proton-exchange membrane. All of these effects lead to high over potentials on both the anode and cathode, and thus reduction of the cell voltage¹⁶⁰. The slow kinetics of oxygen reduction reaction¹⁶¹, which is responsible for overpotential loss of ~0.3-0.4 V under typical conditions of operation, and poor methanol electrooxidation reaction kinetics¹⁶² still seriously affect the DMFC performance. Pt and Pt based alloy catalysts are the best catalysts to date used for oxygen reduction at the cathode and methanol oxidation at the anode,¹⁶³ but even with the platinum-based catalysts, the activity is still not high enough. This drives the utilization of the Pt loading high, thus increasing the costs. The high catalyst costs and limited supply of Pt constitutes a barrier to the commercial application of DMFC. For eventually widespread application of DMFC, material costs need to be lowered while performance and reliability need to be improved. The effective way to lower the cost of the catalyst is to reduce the amount of Pt used in DMFC without sacrificing performance.

Particle shape and size¹⁶⁴, as well as dispersion, are key factors to determine Pt-based catalysts' ORR activity and cell performance for DMFC.^{165,166} Small and uniform Pt nanoparticles with high surface-to-volume ratios are preferred to achieve reliable catalytic performance and to increase efficiency. The active surface area of the catalyst can be greatly increased by reducing the size of the Pt nanoparticles and therefore creating a larger number of catalytically active centers. Therefore, the synthesis of platinum nanomaterial with specific morphology¹⁶⁷ and controlled size is great important in the practical synthesis of Pt particles¹⁶⁸. Substantial effort has been devoted to the development of new synthetic methodologies of catalyst¹⁶⁹, especially in the diameter range of 2-10 nm, to improve catalytic performance¹⁷⁰.

A number of chemical routes have been employed to synthesize platinum nanomaterial with controlled size and catalytic properties, such as the use of chemical reductants in aqueous¹⁶⁹ and organic-phase solvents¹⁷¹, electrochemical approach¹⁷², thermal reduction approach¹⁷³, sonochemical method¹⁷⁴, radiolytic¹⁵³, microwave¹⁷⁵ and photochemical method¹⁷⁶ etc. Chemical methods with NaBH₄ as reductant for the preparation of platinum nanoparticles are convenient, but the quantity of Pt nanoparticles is dependent on solution conditions, the rate and the sequence of reductant addition, and the local over-concentration of reductants etc¹⁷⁷. It is difficult to produce monodisperse nanoparticles with controlled morphology by this kind of method. Furthermore, the excess reducing agents and their oxidation products may contaminate the final products. For electrochemical methods, the main advantage is that they can produce anisotropic platinum nanoparticles. To synthesize size-controlled platinum particles, the photochemical methods have been proved to be a promising method¹⁷⁸. Colloidal dispersion of platinum particles has been obtained through photoreduction of Pt complexes in the presence of a protective polymer under mild and controllable conditions. The photoreduction of Pt complexes

is an attractive method because (i) large number of platinum nuclei are homogeneously and instantaneously produced, so the reduction reaction arises uniformly performed in the solution, thus the size of final nanoparticles is very uniform; (ii) controlled reduction of metal ions can be carried out without using excess reducing agent, and no adsorbing contamination on the product occurs in the preparation process; (iii) the photochemical method can be cost-effective and convenient. Therefore, many studies have been focused on synthesizing platinum particles by photochemical reduction method. In 2005, Harada and Einaga¹⁷⁶ used PVP as a stabilizer in a water-ethanol solution and synthesized platinum nanoparticles by UV radiation, and the formation mechanisms were studied. Their research showed that this process is a promising method to prepare small Pt nanoparticles with a narrow particle size distribution, which can be easily deposited on a substrate and show high catalysis activity for CO photooxidation. In most cases of photoreduced Pt nanoparticles, the reaction only takes place in alcohol solution. It was thought that alcohol is the source of reducing agents under UV-irradiation¹⁷⁸. But Luo¹⁷⁹ et al. show that using PAMAM as a stabilizer, platinum ions can be photoreduced to platinum nanoparticles in water, although the reaction mechanisms was not identified. The problem with this system is that PAMAM is very expensive and requires complex preparation prior to use. Also, Pt nanoparticles prepared by this method only show crown-shape with a size range of 100-130 nm because of PAMAM dendrimer aggregation in this system.

Platinum nanoparticle preparation methods involve the reduction of platinum ions into nanoparticles in protective media to prevent the metal nanoparticles from aggregating. Water-soluble polymers such as poly(vinyl alcohol) (PVA)¹⁸⁰ and poly(N-vinyl-2-pyrrolidone) (PVP)¹⁸¹ have been widely used as protective media for colloidal dispersions. Stabilizers play an important role in controlling the formation of nanoparticles as well as their dispersion stability.

On the other hand the presence of too strong capping agents on the nanoparticles surfaces can produce a detrimental impact on the particle's catalytic properties. For example, PVP capped Pt nanoparticles do not show any electrocatalytic activity toward oxygen reduction or methanol oxidation because of too strong affinity of PVP to Pt¹⁸¹.

Polyethylenimine (PEI) is a hydrophilic polymer with primary, secondary and tertiary amino groups and overall positive charge in neutral aqueous solution. Because of abundant positive charge, it is a widely used stabilizer to coat nanoparticles to achieve surface functionalization¹⁸². The positively charged amine groups stabilized the nanoparticles in solution and can also be used to form self-assembled monolayers on common electrodes. S. Laschi et al¹⁸³ developed glassy carbon electrodes modified with a dispersion of multi-wall carbon nanotubes in PEI. It exhibits excellent electrocatalytic activity towards the analyte. PEI contains one of the highest densities of amine groups among all polymers, this is the reason for the highly efficient dispersion of nanoparticles in PEI as well as for the high electroactivity of the PEI/CNT immobilized on the electrode surface¹⁸⁴.

Polyelectrolyte-capped Pt nanoparticles can be synthesized in aqueous solution, and their assembly on electrodes can allow control of size distribution, shape, and surface density¹⁸⁵. Thus, assembling charged Pt nanoparticles on an electrode may increase efficiency and utilization. Pan et al¹⁸⁶ demonstrated that self-assembled Pt nanoparticles electrode and membrane-electrode-assembly of polymer electrolyte fuel cells can be prepared by using charged Pt nanoparticles with an ultra low Pt loading. Zaki¹⁸⁷ showed that nanostructured Pt electrodes were assembled from solution-prepared polyacrylate-capped Pt nanoparticles by virtue of electrostatic and hydrophobic interactions with a cationic polyelectrolyte: poly(diallyldimethylammonium) (PDDA). Electrochemical characterization of polyelectrolyte-stabilized Pt nanoparticles showed

that these surfaces are catalytically active for many reactions such as oxygen reduction, methanol oxidation, and hydrogen oxidation¹⁸⁸.

In this chapter, a simple, facile, clean and efficient route was designed to prepare PEI/Pt NPs. PEI/Pt NPs were prepared by photoreduction procedure. First, PEI and PtCl_6^{2-} ions are mixed with the desired ratio. PtCl_6^{2-} will complex with functional groups of PEI in an aqueous solution. Then, UV irradiation results in conversion of PtCl_6^{2-} to Pt^0 nanoparticles. The PEI/Pt NPs with average diameter of 3 nm were prepared. The mechanism for the photoreduction of PEI mediated PtCl_6^{2-} to give Pt nanoparticles in aqueous solution was also studied. Our research shows that this process is an excellent procedure to prepare small Pt nanoparticles with a narrow particle size distribution. PEI/Pt NP were deposited on glass carbon electrode and the electrocatalytic activities are investigated. The methanol oxidation reaction in acid electrolytes is examined by using electrochemical techniques. The Pt nanoparticles immobilized on the glassy carbon electrode show extraordinary electrocatalytic activity and stability.

3.3 Experimental methods

3.3.1 Materials

Hexachloroplatinum (IV) acid hydrate ($\text{H}_2\text{PtCl}_6 \cdot 6\text{H}_2\text{O}$; guaranteed reagent) was obtained from Fisher Chemical Company. Polyethylenimine (PEI) with a weight-average molecular weight of 25000 was purchased from Aldrich. The 4-nitrophenol was purchased from Riedel-de Haën AG, while the sodium borohydride was purchased from Fisher Scientific. High-purity nitrogen was used in all experiments. Sulfuric acid (H_2SO_4 , 99.99%) and methanol (CH_3OH , anhydrous) were analytical grade. All chemicals were used as received without further purification. The concentration of the polymer solution is based on the monomer unit.

A Rayonet photochemical reactor (model RPR-600, Southern New England Ultraviolet Inc.) was used as a UV-irradiation system in our experiments. The photochemical reactor is supplied with eight 253.7 nm light sources (8 W per lamp), equipped with a merry-go-round unit, which holds samples for equal irradiation at one time at 5 RPM, and a cooling fan keeps the temperature at ambient.

3.3.2 Synthesis of PEI/Pt NP

Colloidal dispersions of Pt nanoparticles were synthesized from H_2PtCl_6 complexed with PEI by UV irradiation. Each photoreduced particle sample was prepared from 0.3 mL of a 10 mM hexachloroplatanic acid solution, the source of the Pt^{4+} ions used in the reduction. To this solution was added an amount of a 20 mM PEI solution ($\text{C}_2\text{H}_5\text{N}$ monomer concentration), which was varied depending upon the ratio desired. Each sample was diluted to 5 mL using deionized water and placed in a quartz test tube. Under these experimental conditions, the initial reaction mixtures were yellowish in color. The sample was bubbled with nitrogen for twenty minutes, sealed tightly using parafilm, and irradiated by 254 nm light. The merry-go-round unit in the photochemical reactor held multiple samples at one time for even irradiation and the cooling fan kept the temperature at room temperature. The samples were irradiated for 1 day. The growth of Pt nanoparticles was monitored at different intervals using UV-visible absorption spectroscopy.

3.3.3 Characterization of PEI/Pt NP

Transmission electron microscopy (TEM) images of Pt nanoparticles were obtained from a transmission electron microscope (FEI TECNAI F20). The electron beam acceleration voltage was set at 200 KV. Samples for TEM were prepared by deposition of a drop of solution onto a

carbon-coated 300 mesh copper grid resting on absorbent filter paper, which rapidly wicked away the water and allowed the nanoparticles to be dispersed on the grid, followed by air-drying under ambient conditions. All images were digitally recorded with a CCD camera (1024×1024 pixels), and image processing was carried out using a Digital Micrograph (Gatan) and Digimizer. The histogram of the particle size distribution and average diameter were obtained by measuring about 100 particles in arbitrarily chosen areas in the enlarged Digimizer. The data collected by the program was tabulated and analyzed. This procedure was repeated for several different ratios of the photoreduced platinum particles. The UV-vis absorption spectra of the nanoparticles solution were measured by Cary 50 UV-vis spectrophotometer (Varian, USA) using 1 cm optical path length quartz cuvette to pursue the reaction in solution.

3.3.4 Testing of the catalytic ability of Pt nanoparticles

In order to test the catalytic ability of the photoreduced platinum nanoparticles, a reduction reaction was used. This reaction was that of 2 mL of 0.17mM 4-nitrophenol, 0.5 mL of 1.2 M sodium borohydride and 0.5 mL of the photoreduced platinum solution. The reduction reaction was monitored by UV-Vis spectroscopy. For this reduction reaction, the absorbance of the peak at approximately 400 nm was observed and recorded every minute for 10 minutes. A plot was made with the natural log of the absorbance on the y-axis and the time in minutes on the x-axis.

3.3.5 Immobilization of PEI/Pt NP on GC electrode for CV test

Glassy carbon electrodes were used as a substrate for the immobilization of Pt nanoparticles. The glassy carbon working electrode with a geometrical surface area of 0.07 cm² was polished with 1µm and 0.05 µm Al₂O₃ powders successively on Nanocloth, and followed by sonication in Millipore deionized water. PEI/Pt NP solution prepared by UV irradiation was

pipetted on to the surface of the glassy carbon electrode. After water was evaporated overnight at room temperature, the PEI/Pt NP coating was irradiated for 1 hour in the Rayonet photochemical reactor. Then the electrode was washed carefully with ultrapure water before measurement.

3.3.6 Electrochemical instrumentation and measurements

All electrochemical measurement was performed in a conventional three-electrode cell at room temperature. A Pt wire was used as a counter electrode. An Ag/AgCl (saturated KCl solution) reference electrode was used for all electrochemical measurements, and all electrochemical potentials in the present study were given versus Ag/AgCl reference electrode. The working electrode was PEI mediated Pt coated glassy carbon electrode (diameter 3 mm). In order to minimize the effects of impurities during the measurements, the electrode was cycled in 1 M H₂SO₄ solution at 50 mVs⁻¹ between 0 and 1.2 V until reproducible cyclic voltammograms were obtained prior to any electrochemical measurements. Cyclic voltammograms and chronoamperometry were recorded using a computer-controlled CHI 660 electrochemical workstation (CH Instruments, Austin, TX). Hydrogen adsorption cyclic voltammograms were recorded in nitrogen protected 1 M sulfuric acid aqueous solution. The solution was purged with nitrogen to deplete dissolved oxygen before the test. The region for hydrogen adsorption was used to estimate the electrochemical active surface areas. Fresh 1 M H₂SO₄ + 2 M CH₃OH was used in every methanol electro-oxidation methanol measurement to get reliable and reproducible results.

3.4 Results and discussion

3.4.1 Preparation and characterization of PEI/Pt NP

Synthesis of PEI/Pt NPs. It is well-known that transition metal colloids can be formed by photochemical reactions in water/alcohol solutions, in which the reduction of metal salts takes place by solvated electrons and free radicals produced under irradiation. The photochemistry of platinum complexes has been widely investigated in the past because of the virtue of slow and controllable photoreduction process to produce small and well dispersed Pt nanoparticles. Methanol is the reducing agent under UV-irradiation in most cases of Pt photoreduction¹⁸⁹. It is suggested that organic free radicals are produced from adsorbed methanol under UV-irradiation and the radicals reduce Pt salts¹⁹⁰. In this investigation, a photoreduction method was performed to synthesize colloidal Pt nanoparticles by reduction of PtCl_6^{2-} in PEI aqueous solution without ethanol. PEI was used as both stabilizer and reducing agent.

Absorption spectra. PtCl_6^{2-} aqueous solutions are yellow in color. When PtCl_6^{2-} mixed with PEI, the yellow color became less intense. Irradiating with UV light for a few minutes change the solution color to orange, which is the typical color of PtCl_4^{2-} . Then the solution changes to dark brown slowly with further UV irradiation. The color change in formation process of PEI-Pt colloidal via photoreduction of PtCl_6^{2-} was followed by UV-vis spectroscopy. Figure 3.1 presents the UV-vis spectra of the Pt solutions with PEI and without PEI before and after UV irradiation in dilute solution. Figure 3.1 (a), shows a typical electronic absorption spectrum of H_2PtCl_6 in aqueous solution which displays a strong absorption band in 250 nm. After mixing with PEI, as shown in Figure 3.1 (b), the peak at 250 nm disappears, and a new shoulder peak at 235 nm appears due to LMCT (ligand to metal charge transfer)¹⁹¹, which is assigned to the absorption band of a complex of PtCl_6^{2-} with PEI (chloride ligands were replaced by the amine groups of PEI). After only 5 minutes irradiation, the peak at 235 nm totally disappeared, and another shoulder peak at 210 nm appear, as shown in Figure 3.1 (c). This is the typical

absorption position of PtCl_4^{2-} .¹⁹² We can get a conclusion that Pt^{4+} was reduced to Pt^{2+} in the first 5 minutes, a fast reaction. Curve d in Figure 3.1 shows the adsorption of the solution after 60 minutes irradiation. The spectra of solution irradiated for 60 min are similar to the solution irradiated for 5 minutes. It only shows a little increase in 210 nm and slightly increases in baseline compare with curve c. This means that almost no further reduction happens for Pt^{2+} until almost all of Pt^{4+} was reduced to Pt^{2+} . The further reduction of Pt^{2+} to Pt^0 is a slow process compared with the speed of reduction of Pt^{4+} to Pt^{2+} . This is consistent with Cameron's NMR test of photoreduction of platinum in ethanol/water solution¹⁹³. Cameron indicated that photoreduction of PtCl_6^{2-} complexes to Pt^0 via Pt^{2+} and Pt^0 metal formation does not occur until a ~90% yield of PtCl_4^{2-} has accumulated. Irradiation for 1 day resulted in the complete disappearance of the absorption band and a significant increase of the baseline absorbance. The spectrum of solution after 1 day UV irradiation was present in curve e, which implies formation of platinum nanoparticles.¹⁷⁹ This feature has been observed for PVP-stabilized Pt by photoreduction and heat treatment in alcohol-water solution and hydrogen reduction in water, indicating that PtCl_6^{2-} complexes were reduced to metallic species.¹⁹⁰ The resulting solution was stable and no large aggregates or precipitate were observed for at least several months.

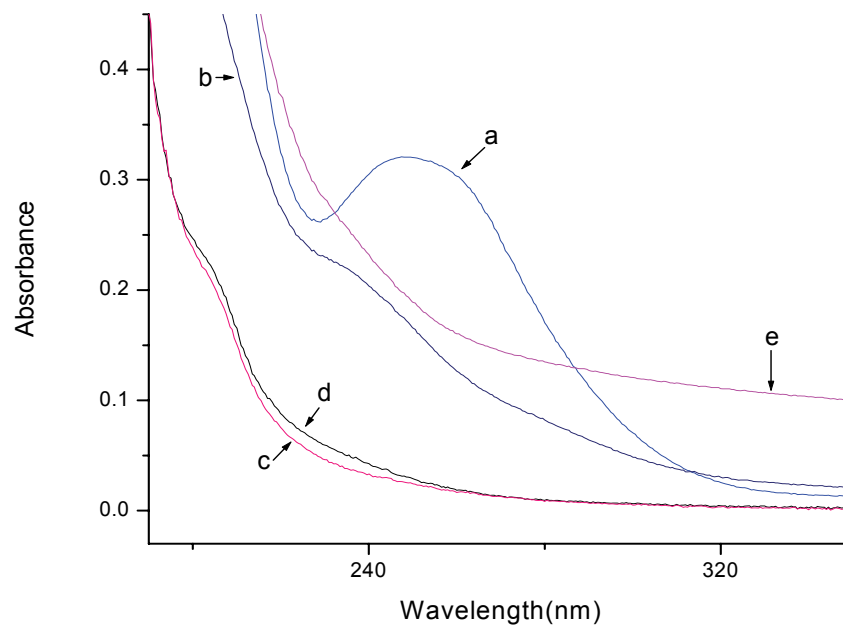


Figure 3.1 Variation of UV-Vis absorption spectra during the photoreduction of H_2PtCl_6 .

a) H_2PtCl_6 aqueous solution; b) mixture of H_2PtCl_6 with PEI; c) complex of H_2PtCl_6 with PEI after 5 minutes UV irradiation; d) complex of H_2PtCl_6 with PEI after 60 minutes UV irradiation; e) complex of H_2PtCl_6 with PEI after 1 day of UV irradiation

TEM images and size distributions. Figure 3.2a shows a typical TEM image at moderate magnifications and the corresponding size distribution histograms of the PEI/Pt NP after photoirradiation. The average particle diameter is 2.97 ± 0.68 nm. The isolation of the PEI/Pt NP is quite good in the colloidal solutions. It can be found that the majority of the Pt nanoparticles have a nearly isometric morphology with very narrow size distribution in the image, and only a very few aggregated particles were observed. Fig 3.2b displays an HRTEM (High-resolution electron microscopy) image. The spacing of lattice fringes measured from the image is 0.25 nm which is about same as (111) inter plane of fcc (face center cubic) Pt nanoparticles. The inset image shows a representative diffraction pattern obtained from FFT (Fast Fourier Transform)

analysis of that particle. The HRTEM image shows that the photoreduced Pt nanoparticles are well ordered at the atomic scale.

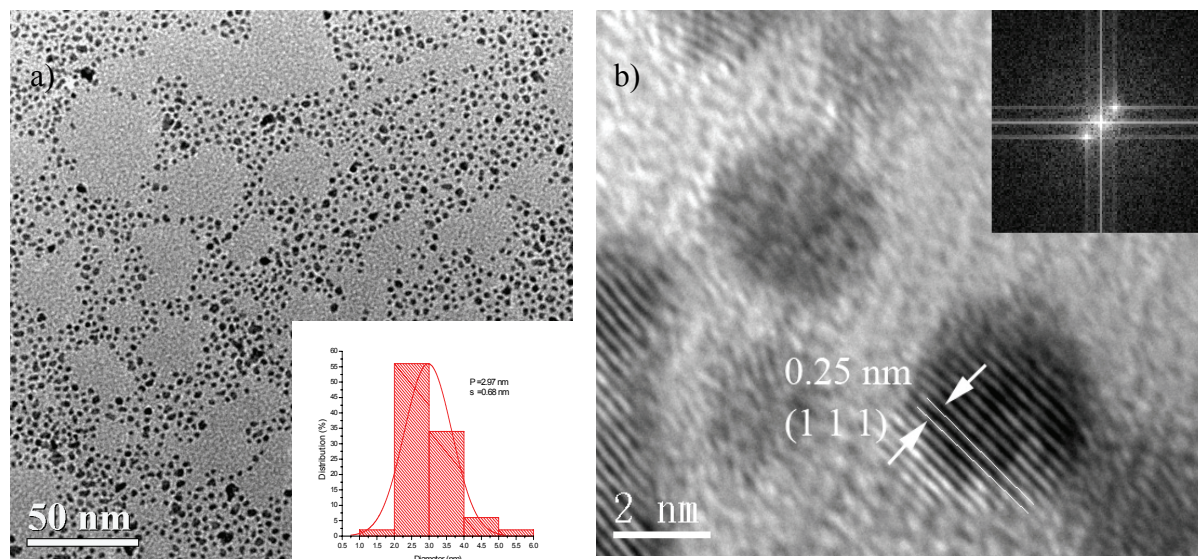


Figure 3.2 TEM images of PEI/Pt NP synthesized by photoreduction.

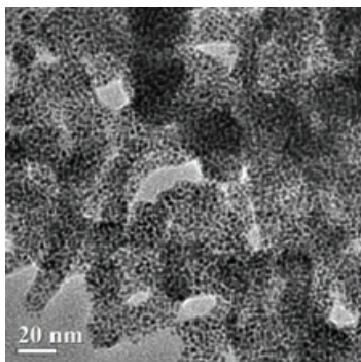
a) Image in moderate magnifications, the inset at the bottom show it's corresponding size distribution histograms of the PEI/Pt NP; b) HRTEM of Pt nanoparticles and the inset on the top right show FFT pattern, the fringe spacing of 0.25 nm corresponds to the interplanar separation between the (111) planes.

Effect of initial molar ratio (PEI: Pt) To investigate the influence of initial molar ratio of PEI to Pt on as-prepared Pt nanoparticles, samples 1–9 with corresponding initial molar ratio 1:1, 3:1, 6:1, 8:1, 10:1, 15:1, 17:1, 18:1 and 20:1 of PEI (repeating unit) to Pt were prepared. Low molar ratio (1:1 to 6:1) and high molar ratio (19:1 or higher) resulted in unstable solutions. After a few days, black metal deposits that precipitated from solution due to the coagulation of as-prepared particles were observed from these unstable solutions. However, the solutions with moderate molar ratio of 8:1 to 18:1 are stable at least for several months. These samples were characterized by TEM. Figure 3.3 show the images with different PEI to Pt ratio. As seen in the images, the particles produced with smaller amounts of PEI (ratios 1:1- 6:1, Figures 3.3 (1)-(6))

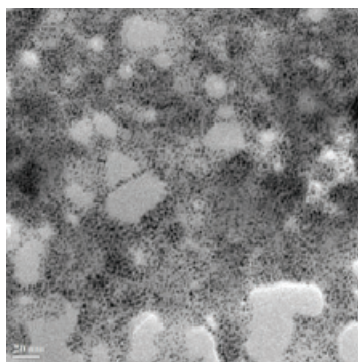
are more clumped together. It is believed that this is due to the nanoparticles sticking to each other without enough PEI stabilization. The particles formed using the 8:1 to 15:1 ratio show much better disperse. The particles formed using the 17:1 and 18:1 ratios (Figures 3.3 (7) and (8)) are best dispersed and do not overlap each other. This is most likely because there is just enough PEI to disperse the particles evenly. At the highest ratio (20:1 or higher, the particles are clumped again, possibly due to the bridge of the PEI by Pt nanoparticles. These TEM images explained the stability difference of these samples: clumped sample are not stable, while the better dispersed samples are more stable. This result is similar as thermal reducing of gold in PEI⁶³: lower PEI to gold molar ratio (2:1, 3:1) and higher molar ratio (8:1 and 9.5:1) resulted in the formation of gold particle aggregates; coagulation of as-prepared particles were observed when initial molar ratio was lower than 1.5:1 or higher than 10:1.

The size and size distribution of samples with different PEI to Pt ratio was analyzed and compared. Table 3.1 show the diameter analysis of TEM images. It can be seen that the ratio of PEI to Pt almost does not affect the size and size distribution of as-made Pt nanoparticles although the ratio of PEI to Pt affect the stability of final products. This result is different from the thermal process of PEI mediated gold nanoparticles. In the case of thermal reducing of gold with PEI⁶³, nanorods and large particles (~ 100 nm) with hexagonal shape are observed in sample with low PEI to Pt ratio, and at a moderate molar ratio of 5:1, only dispersed nanoparticles (~ 25 nm in diameter) were obtained. But at higher ratio of 9.5:1, the formation of quasi one-dimensional aggregates is again noticed.

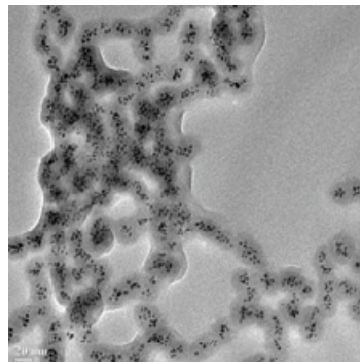
(1) 1:1



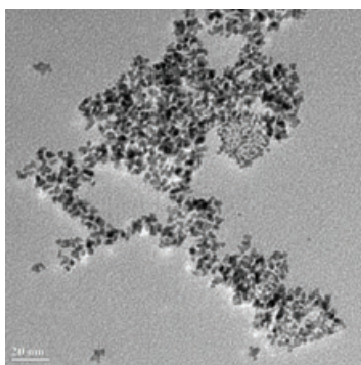
(2) 3:1



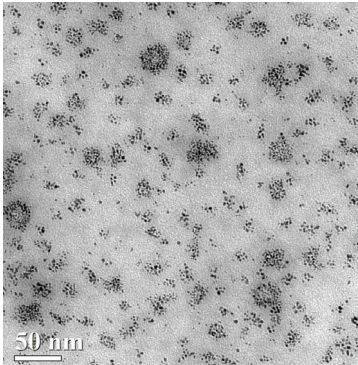
(3) 6:1



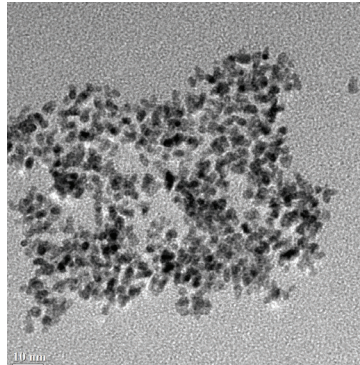
(4) 8:1



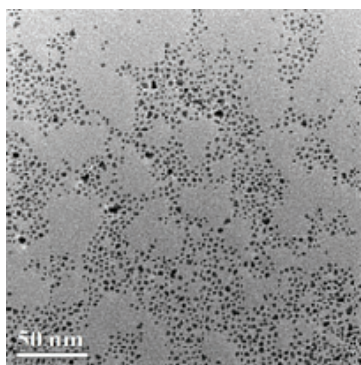
(5) 10:1



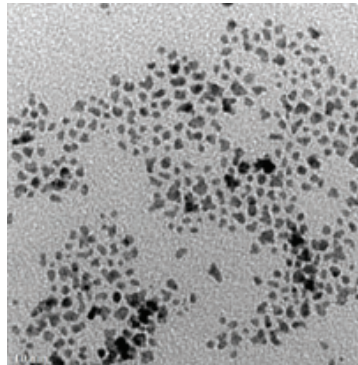
(6) 15:1



(7) 17:1



(8) 18:1



(9) 20:1

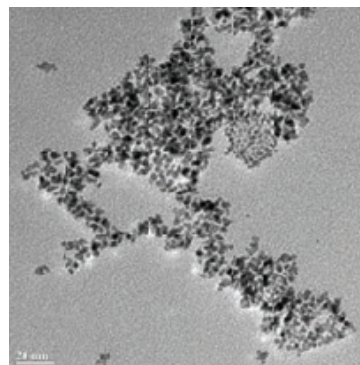


Figure 3.3 TEM images of sample 1-9 with PEI:Pt ratio of (1) 1:1; (2) 3:1; (3) 6:1; (4) 8:1; (5) 10:1; (6) 15:1; (7) 17:1; (8) 18:1; (9) 20:1

Table 3.1 Tabulated diameter analysis of samples with different PEI to Pt ratio

Ratio	Mean size (nm)	SD	Relative error
1:1	2.79	0.36	13%
3:1	2.52	0.50	20%
6:1	3.20	0.57	18%
8:1	3.18	0.74	23%
10:1	3.00	0.61	20%
15:1	2.83	0.43	15%
17:1	3.01	0.64	21%
18:1	3.28	0.61	19%
20:1	2.96	0.41	14%

3.4.2 Catalysis analyzation of photoreduced Pt nanoparticle

In order to test the catalytic ability of the photoreduced nanoparticles, a reduction of 4-nitrophenol was chosen as a model. This reaction was that of 2mL of 0.17mM 4-nitrophenol, 0.5mL of 1.2M sodium borohydride and 0.5mL of the reduced platinum solution. 4-nitrophenol aqueous solution itself shows a spectral profile with an absorption maximum at 310 nm¹⁹⁴.

Addition of sodium borohydride solution results in the shifting of the peak position to 400 nm which corresponds to the formation of 4-nitrophenolate ions in alkaline condition caused by the addition of NaBH_4 . The mixture, initially yellow, became colorless as the 4-nitrophenol was successive reduced to 4-aminophenol, allowing the reaction to be monitored using UV-Vis spectroscopy. In the absence of Pt catalyst, the absorbance value and the peak position of remained the same even for a couple of days. For this reduction reaction, the changing of the peak absorbance at approximately 400nm can be observed and recorded periodically. The concentration of the sodium borohydride greatly exceeds those of 4-nitrophenol, therefore it should remain essentially constant during the reaction. A pseudo-first-order kinetics with respect to 4-nitrophenol can be used to evaluate the catalytic rate in this condition¹⁹⁵. A plot can be made with the natural log of the absorbance on the y-axis and the time in minutes on the x-axis, with linear correlation should be obtained for all the samples studied. The absolute value of the slope of the fit line running through the linear points on the graph was considered the rate of the reaction which can be used to evaluate the catalytic activity.

Figures 3.4 (a) and (b) demonstrate this procedure for determination of catalytic ability. Figure 3.4 (a) shows the resulting spectra from the catalytic reaction using a photoreduced sample with a 18:1 PEI monomer to platinum ratio. The absorbance of the peak at 400nm was recorded after each minute of reaction time. Figure 3.4 (b) shows the plot of the natural log of the absorbance at each time versus the time it was taken at. The absolute value of the slope of the fit line running through the points is 0.19 for this 18:1 ratio sample. The values of the pseudo-first-order rate constants determined from different samples are given in Table 3.2. It was find that the apparent first-order rate law fitted reasonably well to most of samples.

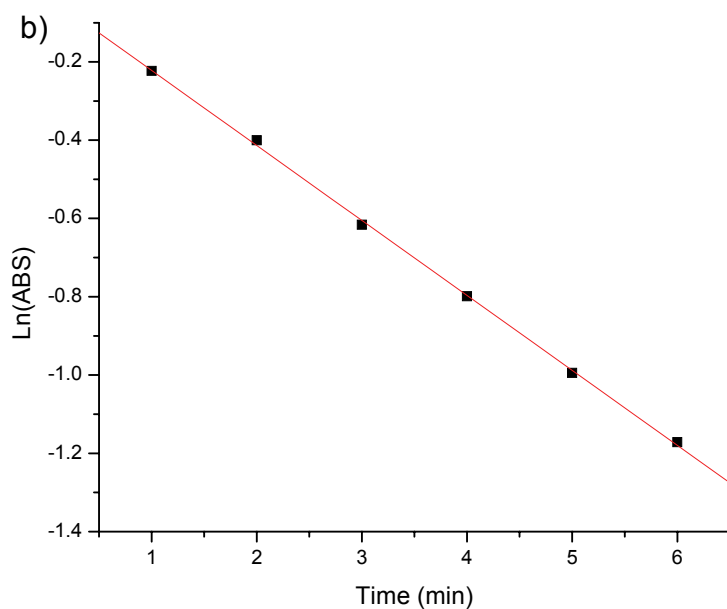
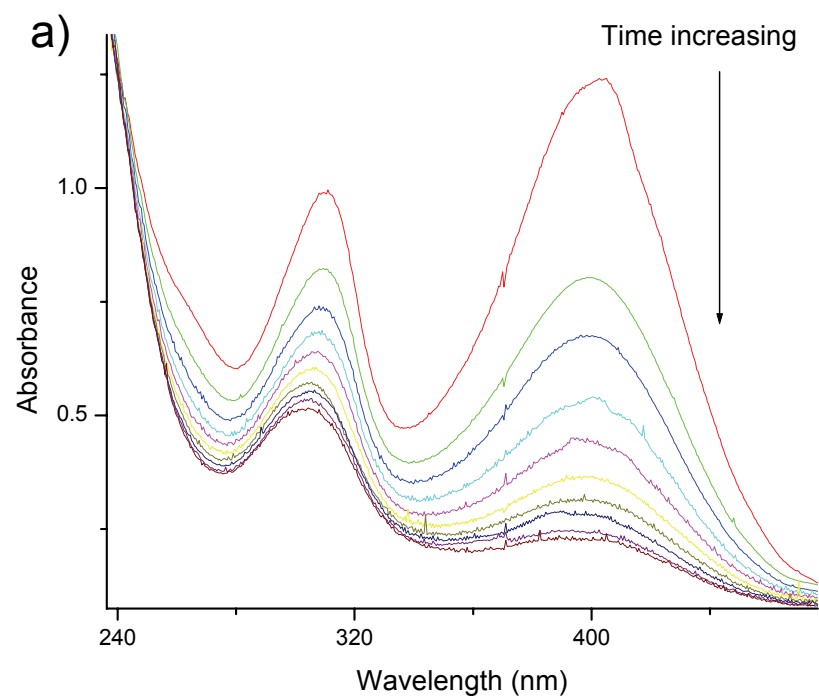


Figure 3.4 a) Successive UV-Vis spectra of reduction of 4-NP by Pt nanoparticles with a PEI to Pt ratio of 18:1. Time of interval is 1min; b) Plots of $\ln A$ versus time for the reduction of 4-nitrophenol by Pt nanoparticles prepared by a PEI to Pt ratio of 18:1

Table 3.2 Rate Constant for the Reduction of 4-Nitrophenol with different PEI to Pt ratio

PEI to Pt Ratio	Rate constants K (1/min)	Stability
1	0.075	Unstable
3	0.090	
6	0.138	
8	0.166	Stable
10	0.171	
13	0.188	
15	0.207	
17	0.265	
18	0.192	
19	0.098	
20	0.087	
24	0.079	
28	0.074	

Figure 3.5 summarized the relation of the PEI to Pt ratio, catalytic activity and stability of the Pt nanoparticles. It has been shown that there are three region in this figure: two unstable regions and a stable region. When the PEI to Pt ratio increases, the pseudo-first-order rate constants increase too. There is a maximum value of pseudo-first-order rate constants at ratio of 17:1. After this ratio, the pseudo-first-order rate constants decrease with the increasing of PEI to Pt ratio. It is supposed that the diffusion of 4-nitrophenol mainly controls the rate of reduction¹⁹⁵. As seen from the TEM results, Pt dispersed not very well in low PEI to Pt ratio because of not enough stabilizing agent (PEI), thus it is a unstable solution. As a result, 4-nitrophenol can not effectively reach the surface of Pt nanoparticles because of aggregation of Pt nanoparticles in low PEI to Pt ratio. While for very high PEI to Pt ratio, PEI with rich amino groups are considered to be adsorbed on the platinum nanoparticles, the high density of adsorbing PEI would affect the diffusion of 4-nitrophenol to the platinum nanoparticle surfaces. So pseudo-first-order rate constant can only reach maximum in moderate PEI to Pt ratio. Accordingly, it can be concluded that the stability of the solution and rate constant of the reduction reaction is predominantly controlled by the amount of PEI adsorbing on the platinum nanoparticles.

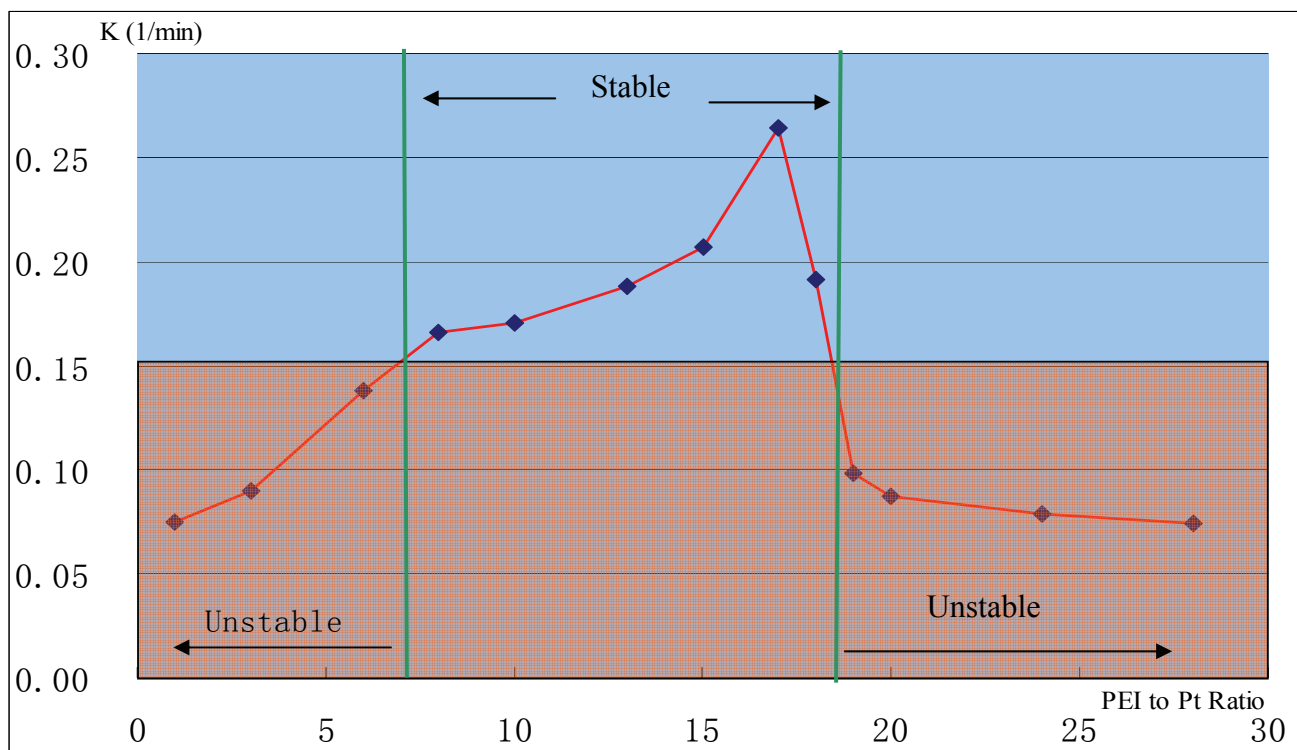


Figure 3.5 The relation between the PEI to Pt ratio and catalytic activity.

3.4.3 Electrocatalytic activity of photoreduced Pt nanoparticle

Deposition of Pt nanoparticles on GC electrode. The preparation of polymer-coated electrodes has been a relevant subject of interest recently. The catalytic activity of Pt nanoparticles is generally affected by their size, shape and stabilizing agents controlled by the preparative conditions. The polymer matrix might provide an efficient pathway for electron and photonic species for fuel cells. Many kinds of polyelectrolyte assembled on electrodes were studied¹⁹⁶. Among them, PEI is a polyelectrolyte which has been used widely for the preparation of multilayer assemblies yielding novel multifunctional materials. The procedure in this study for polyelectrolyte coating of electrode with PEI is based on solvent evaporation. The PEI/Pt NP

solution was applied directly on the glassy carbon surface. After the solvent evaporated, PEI coating layer was irradiated by UV light. It has been shown that γ -irradiation or UV radiation can generate free radicals on the polymer chains which react to covalently cross-link the chain¹⁹⁷. Cross-linking combines the polymer chains into a continuous network extending over the entire electrode makes it intractable in that it is more stable on the surface of the electrode and will not be soluble in the medium. It has been show the Pt nanoparticles with a PEI to Pt ratio of 17 have highest catalytic ability by above tests, therefore all of next electrocatalytic activity experiments use the sample with the PEI to Pt ratio of 17.

Cyclic Voltammetry Profiles of PEI/Pt NP. Figure 3.6 presents the cyclic voltammograms for PEI/Pt NP coating electrodes at different scan ranges in 1 M H₂SO₄ solution. The PEI coated electrode does not show any characteristic peak in the potential range shown (Figure 3.7), whereas the PEI/Pt NP coating electrodes display the characteristic voltammetric profile of Pt surfaces¹⁹⁸: hydrogen adsorption-desorption, the double-layer and formation and removal of platinum surface oxides. These cyclic voltammograms features are in good agreement with the cyclic voltammograms curves for other Pt electrodes¹⁹⁹. This demonstrates that the voltammetric features of Pt nanoparticles electrode are due to the presence of Pt in PEI on the electrode. Hydrogen underpotential (H_{upd}) deposition is very sensitive to crystallographic orientation of the platinum surface²⁰⁰. The adsorption peaks of hydrogen are distinctly resolved when the potential was scanned to the region of oxide formation, while when the potential was scanned below the oxide formation region the adsorption states peaks of hydrogen are not well resolved (figure 3.6 b). The corresponding hydrogen adsorption-desorption peaks H_{A1} and H_{D1}, are associated with the Pt (110) crystal plane, and hydrogen adsorption-desorption peak a H_{A2} and H_{D2} are associated with the Pt (100) crystal plane¹⁸⁷. The broad H-adsorption below the Pt (110) and Pt (100) peaks

possibly indicates the presence of Pt (111) sites. Resolved hydrogen adsorption states at the PEI/Pt NP assembled on the electrode is a significant signal because it indicates that PEI is a good capping agent which does not block H_{upd} catalytic sites, while in the case of PVP mediated Pt colloidal, H_{upd} states can not be resolved¹⁸¹. The O_{O1} and O_{O2} peaks show typical Pt oxidation at high potential, while peak O_R was associated with the reduction of platinum oxide. This is an evidence of the presence of platinum on the electrode surface²⁰¹. It may be concluded that the platinum nanoparticles have a clean active surface.

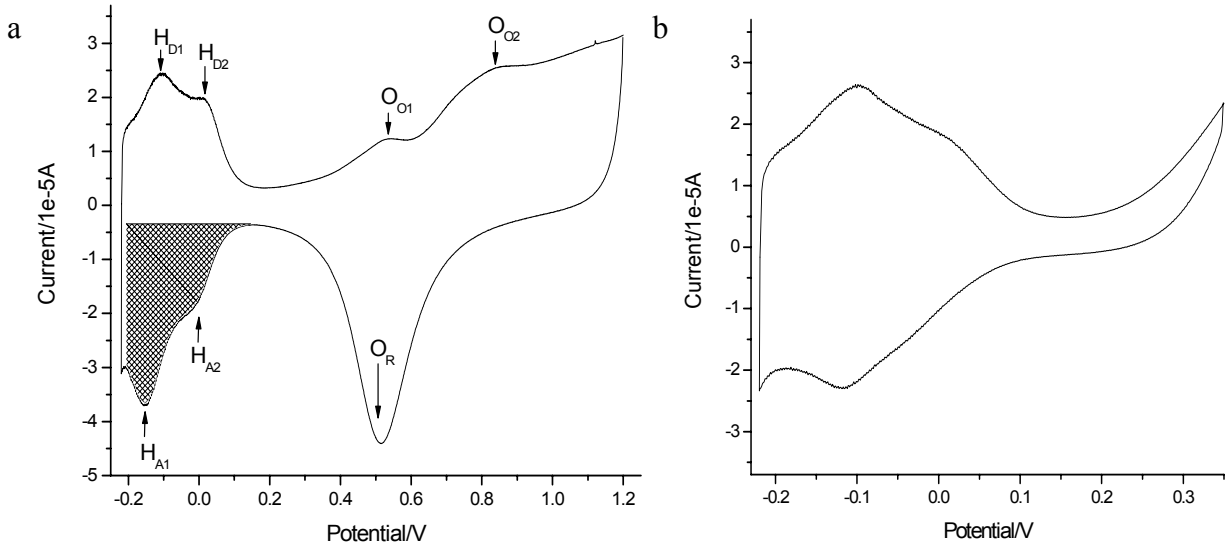


Figure 3.6 CV of the as-prepared PEI/Pt NP coated electrode.

Supporting electrolyte: N_2 saturated 1M H_2SO_4 , scan rate: 20 mV/ s and electrode area: 0.07 cm^2 .
a) Potential between -0.22 V and 1.2 V; b) Potential between -0.22 V and 0.35 V.

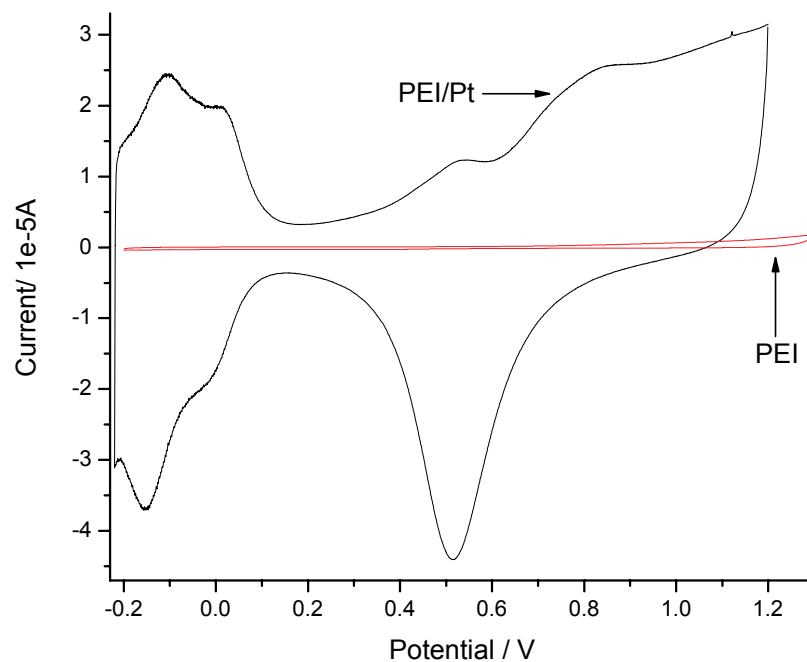


Figure 3.7 Comparison of pure PEI with PEI/Pt NP coated electrode response in 1 M H₂SO₄.

The catalytic activity of Pt nanoparticles was evaluated by its active surface area. The active area of Pt nanoparticles can be estimated by the hydrogen underpotential deposition. This area is calculated by integrating the cathodic current for hydrogen adsorption reaction with correction for the “double layer” charging current²⁰² (as show in the net shaded region in Figure 3.6a). A reported clean polycrystal Pt electrode’s charge density of 210 $\mu\text{C}/\text{cm}^2$ was used, assuming adsorption of one hydrogen atom per platinum atom.²⁰³ The area of the electrochemically accessible nanoparticles was calculated to be 1.32 cm^2 . The roughness factor (f) was defined as the ratio of the true active surface area to the apparent geometric area. From this procedure, the roughness factor is about 20.

Electrocatalytic Activity of Methanol Oxidation Reaction It is well known that Pt nanoparticles have good catalytic activity and stability for the electrochemical oxidation of methanol in the acidic environment of DMFC.¹⁵⁷ The catalytic properties of PEI mediated Pt was studied by cyclic voltammetry. Figure 3.8 presents the cyclic voltammograms obtained from the oxidation of methanol at PEI mediated Pt coated electrodes in 1 M H₂SO₄ containing 2 M methanol. Voltage sweeps were scanned in the range of 0-1 V at a rate of 20 mV/s. A well-defined symmetric anodic peak for the oxidation of methanol at 0.66V in the forward scan is apparent. In the reverse sweep direction, an anodic reverse peak was recorded at 0.47 V. This reverse anodic peak is attributed to the removal of surface adsorbed, incompletely oxidized intermediate species generated during the oxidation of methanol, mainly CO. The peak current at 0.66 V and 0.47 V, which are consistent with that reported in the literature²⁰¹, are not observed at pure PEI electrode (Figure 3.9), demonstrating that the Pt nanoparticles are responsible for the electrocatalytic activity.

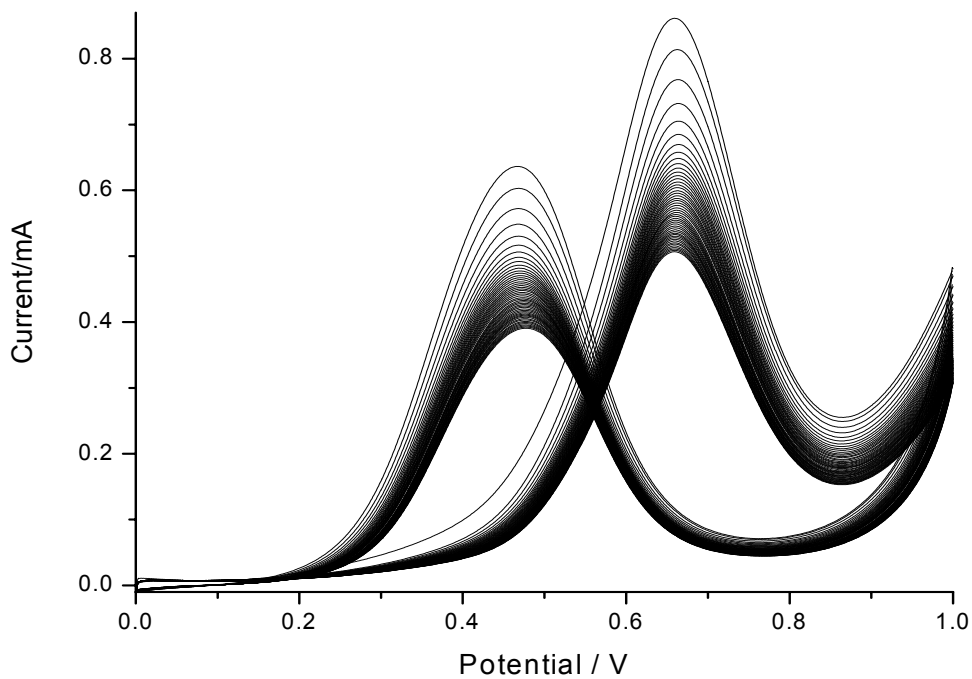


Figure 3.8 50 consecutive cycle scans of methanol oxidation obtained from PEI/Pt NP coated electrode with a scan rate of 20 mV/s in 1 M H₂SO₄, 2 M methanol at 298 K. The peak current decreases with the number of scans. The voltammograms were recorded at 2 second intervals.

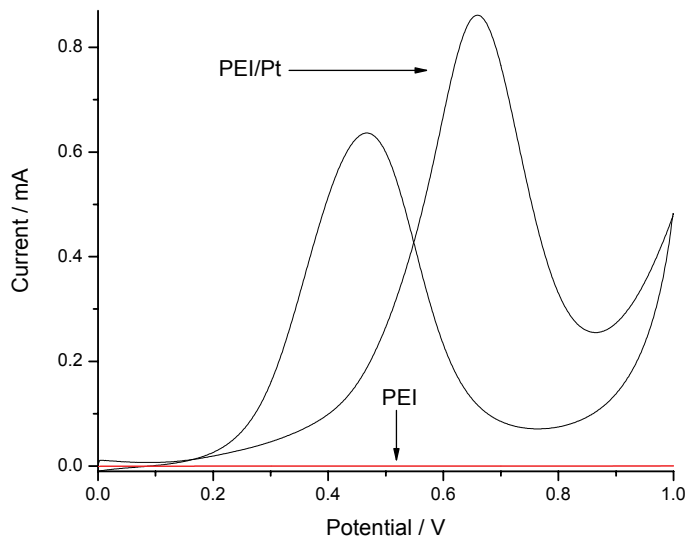


Figure 3.9 Comparison of pure PEI with PEI/Pt NP coated electrode response in 1 M H₂SO₄ and 2M CH₃OH.

Electrooxidation of methanol is a complicated chemical reaction. Even after several decades of study, the mechanism of the oxidation of methanol is still not completely understood. Several different reaction mechanisms have been proposed¹⁶⁰. Spectroscopic studies²⁰⁴ indicate that methanol molecules are first absorbed on the surface of Pt and disassembled as intermediates such as Pt-(CHO)_{ads} and Pt-(CO)_{ads}; H₂O is absorbed to the surface of Pt as intermediate Pt-(OH)_{ads} which reacts with carbonaceous intermediates to give CO₂ producing the stripping peak in the backward scan. It is generally agreed that the most abundant surface intermediate is CO, which can poison the catalyst. The ratio of the magnitude of the anodic peak current in the forward sweep to the reverse sweep has generally been used to evaluate catalyst tolerance to intermediate species accumulation on the surface of the electrode.²⁰⁵ The higher the ratio of the forward anodic peak current to the backward anodic peak current (I_f/I_b), the more methanol is oxidized to carbon dioxide which means that the concentration of intermediate species on the electrode is relatively lower, thus a better tolerance to the poisoning²⁰¹. In our experiments, the ratio is about 1.3. This is much higher than those reported for most of other Pt-based electrodes. For example, the ratio of 0.87 was reported with nanosize Pt on carbon.²⁰⁵ Such a high value indicates that most of the CO is oxidized to CO₂ in the forward scan and that the Pt nanoparticles coated electrode does not undergo serious poisoning by the accumulation of CO.

The onset potential for the oxidation of methanol in our experiments is about 0.1 V (Figure 3.10a), which is 0.3 V less positive than the bulk Pt electrode (Figure 3.10b shows a CV comparison of PEI/Pt NP with Pt electrodes. Both of them were recorded in 1 M H₂SO₄ containing 2 M CH₃OH at 20mV/s). The onset potential for the oxidation of methanol on our PEI/Pt NP coated electrode is also much lower than those of the other Pt based nanoparticles based electrodes. For example: Geng et al²⁰⁶ studied the onset potential of methanol

electrooxidation for various Pt based multicomponent electrocatalysts and most onset potential of their catalysts are in the range of 0.12-0.39 V; the onset potential on iridium-Pt nanoparticles based²⁰⁷ and the nanoporous Pt network¹⁴ electrode were observed at 0.2 V; it was also shown that the onset potential of carbon nanotube/Pt nanoparticles electrode²⁰⁸ was 0.2 V. Although such a comparison is not very precise because the catalytic activity is related to many factors such as preparation technique, surface area, particle size and distribution, pretreatment etc, the low onset potential and larger I_f/I_b ratios conclusively indicates that PEI/Pt NP show superior electrocatalytic activity for methanol oxidation and good tolerant to CO poisoning.

In our study, the peak current in the first forward scan at 0.66V is 0.861mA. Based on the geometric electrode surface of 0.07cm^2 , we obtain a current density of 12.3 mA/cm^2 for 2 M of methanol (scan rate of 20 mV/s) on the Pt nanoparticles coated electrode with a very low Pt loading. For comparison, Liang¹⁸¹ found that PVP coated Pt nanoparticles produce almost no response to methanol with no oxidative or hysteresis phenomenon observed. Their work indicates that the poor signal arising from the PVP stabilized nanoparticles can be attributed to the presence of the strong capping agent on the Pt nanoparticles surface, inhibiting the particles' catalytic properties. The strong affinity of PVP for the Pt nanoparticles hinders the diffusion of methanol to the Pt surface, and thus inhibits electron transfer from Pt. In contrast, our PEI coated Pt nanoparticles show good catalytic properties for methanol oxidation. The reasons may be that the affinity of PEI for Pt is not as strong as PVP, or that UV irradiation lessens the affinity of PEI with Pt. In the other side, the homogenous distribution of Pt nanoparticles and smaller size are also expected for producing high electrocatalytic activity.

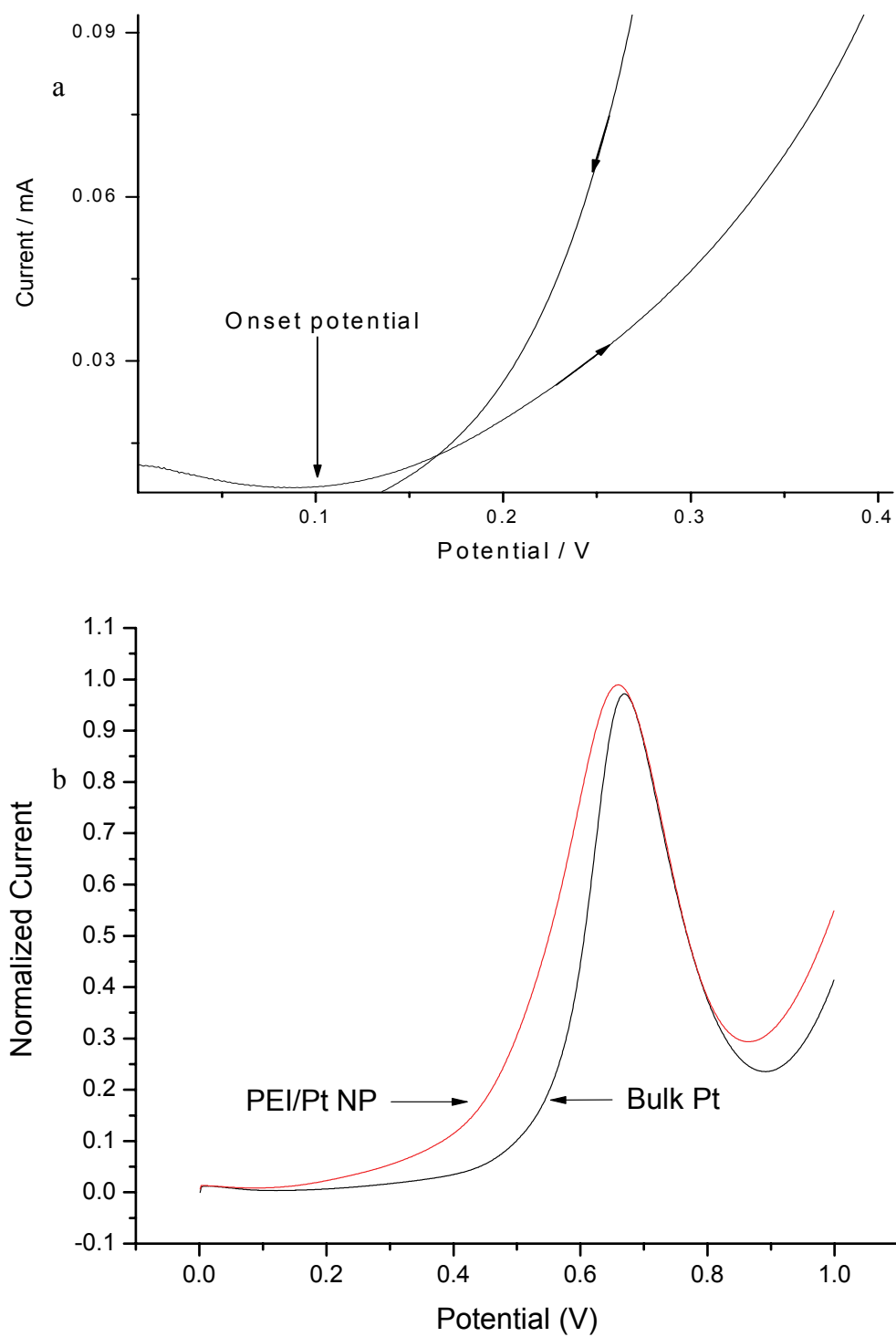


Figure 3.10 a) Magnified CV image of PEI/Pt NPs coated electrode. Onset potential is labeled in the image. The arrows show the scan directions. b) Comparison of PEI/Pt NPs with bulk Pt electrode. CV was scanned in 1M H_2SO_4 and 2M CH_3OH .

The long-term stability of the Pt nanoparticles coated electrode is particularly important for the development of DMFCs. The long-term stability of the electrode was tested by using the same electrode for 50 repetitive cycles. The forward and backward peak currents (Figure 3.8) on Pt nanoparticles coated electrodes were measured as a function of the number of cycles, as shown in Figure 3.11a. It can be seen that the shape and peak potential of the curves show no evident changes, but the peak current decreases with increasing cycle number. The gradual decrease in catalytic activity after successive cycles of potential scan could result from the consumption of methanol during the electrochemical oxidation reaction. A better measure of stability comes from the ratio of the forward anodic peak current to the backward anodic peak current (I_f/I_b), calculated as a function of the number of cycles as shown in Figure 3.11b. Only a 3.7 % decrease in I_f/I_b was observed after 50 cycles, demonstrating that the electrode does not undergo serious deactivation by the oxidation/reduction product, and still shows good catalyst tolerance to poisoning.

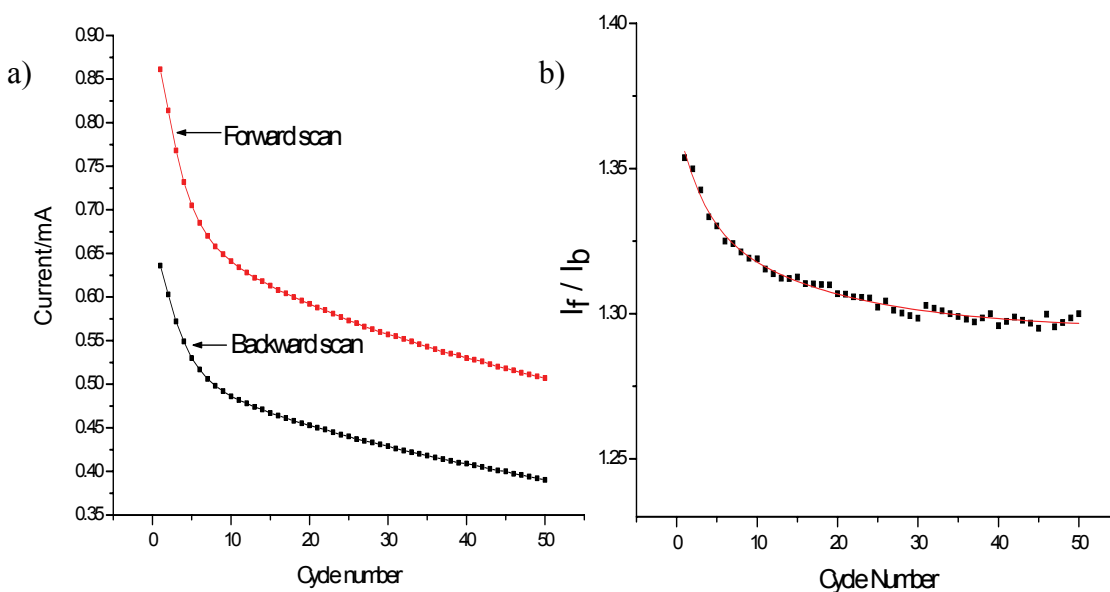


Figure 3.11 Long-term cycle stabilities of PEI/Pt NPs coated electrode over 50 scan in N_2 saturated 1 M H_2SO_4 + 2 M CH_3OH at scan rate of 20 mV/s. a) The variation of the forward and backward scan peak current with cycle number. b) Plot of I_f/I_b versus cycle number.

In order to understand more about the nature of oxidation product, the scan at different potential limits were obtained which shown in Figure 3.12. When the scan limit is higher than 1.2 V, a new shoulder peak appears at about 1.18 V, which is associated with oxidation of carbonaceous species. The backward anodic peak potential and peak current density decrease. This is consistent with results of the Pt/C and Pt/carbon nanotubes^{201, 205}. The ratio of I_f/I_b increasing with the anodic scan limit confirmed that the reverse anodic peak current is associated with residual carbon species on the Pt nanoparticles coated electrode.

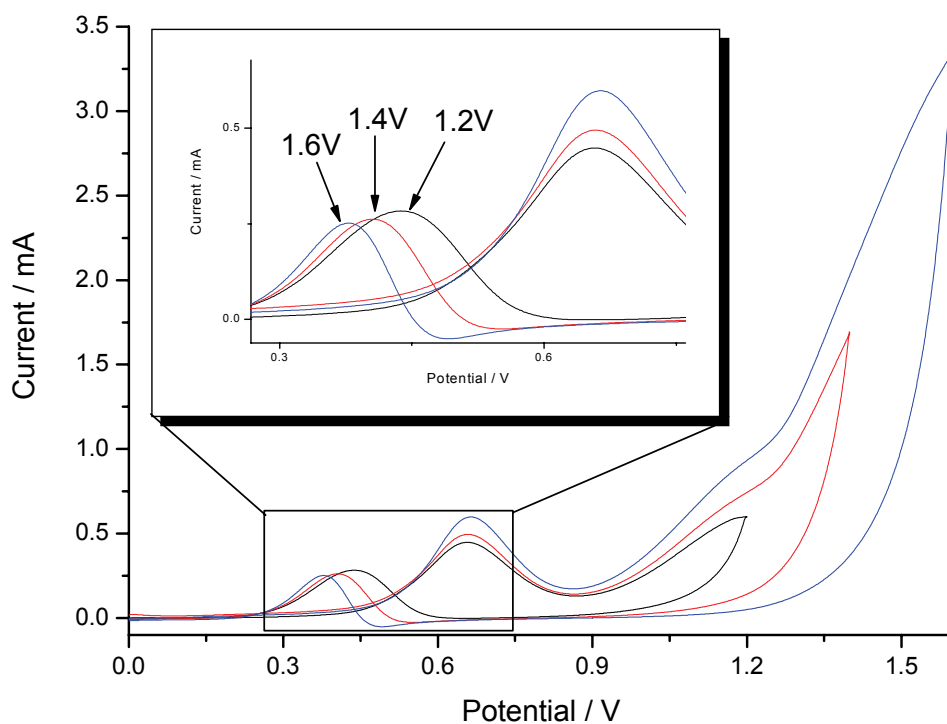


Figure 3.12 Cyclic voltammograms of methanol oxidation on PEI/Pt NP coated electrode at 20 mV/s in 1M H₂SO₄, 2M CH₃OH with different potential scan limits labeled in the inset figure. The inset shows a magnified peak region.

Chronoamperometry scans were measured at different potentials for 600 seconds on the Pt nanoparticles coated electrode and the results are shown in Figure 3.13. It was found that the largest current occurs at 0.6 V compared to 0.8 V and 0.3 V. This is consistent with the above result from cyclic voltammogram tests. The current gradually decreases with time because the methanol is electro-oxidized continuously and the concentration of methanol decreases with time.

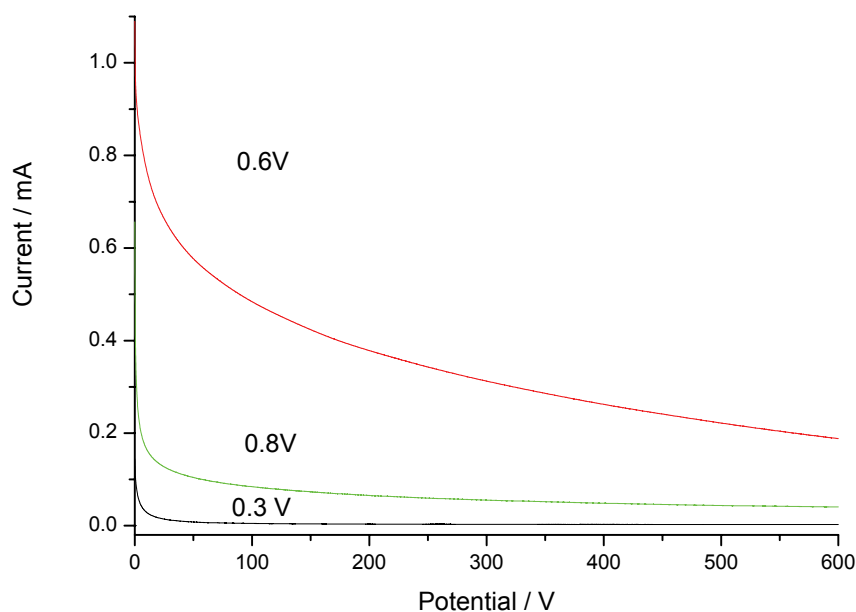


Figure 3.13 Chronoamperometry curves of PEI/Pt NP coated electrode for methanol oxidation recorded at 0.3 V, 0.6 V and 0.8 V in 1M H₂SO₄ and 2M CH₃OH, at 298K.

3.5 Conclusions

In this study, we have demonstrated that monodisperse Pt nanoparticles can be synthesized in PEI aqueous solution by a photoreduction method. The results obtained from UV-vis spectroscopy and TEM clearly demonstrate the photoreduction of PtCl₆²⁻ to Pt nanoparticles. Photoreduction of PtCl₆²⁻ complexes to Pt⁰ metal particles via Pt²⁺. Pt⁰ metal formation occurs

only after almost all of PtCl_6^{2-} converts to PtCl_4^{2-} , and the reduction from PtCl_6^{2-} to PtCl_4^{2-} is a fast process, while the reduction of PtCl_4^{2-} to Pt^0 metal particles is a slow process. It has been shown that PEI play an important role in the preparation of Pt nanoparticles. Different ratio of the ratio of PEI to Pt results in the product with similar diameter but with different stability. Testing the catalytic ability of photoreduced particles by reduction of 4-nitrophenol showed that there is strong relation between the the ratio of PEI to Pt and the cataytic activity. PEI/Pt NP can be assembled on the surface of a glassy carbon electrode, and the electrocatalytic activity was also studied. Hydrogen adsorption states were observed and well resolved at as-prepared PEI/Pt NP assembled on electrode surfaces, without subjecting the nanoparticles decapping. The high current density, I_f/I_b value and lower onset potential for methanol oxidation show that the PEI/Pt NP exhibit excellent catalytic properties for methanol oxidation reactions. It partly overcomes the accumulation of intermediate carbonaceous species on the catalysts' surface which leads to catalyst poisoning in fuel cell. The system is highly stable toward the oxidation of methanol for long term cycles. These results present in this study indicate that PEI is a good candidate to be used as a capping and reducing agent in photoreduction of Pt nanoparticles. At the same time, it can work as a good carrier to immobilize the nanoparticles on the surface of the electrode. The presence of PEI in this system not only mitigates the CO poisoning of Pt catalyst, but also enhances the electrocatalytic activity and stability of the catalyst. PEI assisted photoreduction synthesis appears to be a promising method for the preparation of well-dispersed Pt nanoparticles, and this method provides an attractive route to Pt catalysts with good electrocatalytic activity and reliable catalytic performance.

CHAPTER 4 UV Irradiation Strategy for Synthesis of Spinel Co₃O₄ Nanorods at Room Temperature

4.1 Synopsis

A UV-assisted method was used to synthesize polyelectrolyte-mediated Co₃O₄ nanocrystals. High quality rod-shape Co₃O₄ nanocrystals were synthesized at room temperature and ambient pressure. Polyethylenimine was used as a stabilizer, leading to the growth of nanocrystals to nanorods. UV-vis absorption spectra were obtained to pursue the formation process of Co₃O₄ nanorods. The research results demonstrate that the morphology of Co₃O₄ nanorods is dependent on the molar ratio of PEI to precursor Co²⁺. The shape, size, and morphology of the Co₃O₄ nanorods dispersed in the PEI matrix were characterized by TEM. The crystal structure was also determined by powder XRD and Raman spectroscopy. HRTEM and XRD studies show that the nanorods are spinel phase single-crystal materials. The possible formation mechanism is discussed.

4.2 Introduction

Synthesis of one-dimensional (1D) nanomaterials has attracted considerable attention²⁰⁹, owing to their intriguing properties, unique structures, and potential applications in electronic, magnetic, optical and catalytic materials^{210, 211}. 1D nanomaterials such as nanobelts^{212, 213}, nanorods²¹⁴, nanotubes²¹⁵, and nanowires^{216, 217} have been synthesized by various methods, including structure-directing hard templates (such as alumina²¹⁸, silica^{219, 220}, polymer²¹⁵ etc); soft templates (such as surfactants²²¹,) and coordinating ligands²²²; vapor-liquid-solid (VLS) growth²²³; and the self-assembly of spherical nanoparticles by oriented attachment²²⁴. These

methods have successfully synthesized 1D nanostructured metals, metal oxides, and metal chalcogenides.

The p-type semiconductor Co_3O_4 is an important functional material and has been widely used in anode materials^{225, 226}, solid-state sensors^{227, 228}, heterogeneous catalysts²²⁹, solar energy absorbers²³⁰, pigments²³¹, and other applications. Nanostructured Co_3O_4 is especially popular because of its high surface-to-volume ratio. Nanostructured Co_3O_4 displays very high discharge capacity as the anode material in Li-ion rechargeable batteries²³², and exhibits good sensitivity to certain reactants²²⁸, such as hydrogen and alcohol. For most applications it would be highly desirable to prepare nanostructured Co_3O_4 with well-defined morphology in a narrow size distribution.

Much effort has been devoted to developing new methods for preparation of Co_3O_4 on the nanoscale. The thermal decomposition of inorganic precursors^{214, 233}, crystallized cobalt alkoxides²³⁴⁻²³⁶, or polymer fibers²³⁷ at high temperature are traditional methods. For example, Hou et al.²³⁸ synthesized cobalt oxide by cobalt hydroxide route. First, cobalt hydroxide nanoplatelets were prepared by precipitation and hydrothermal treatment. Then cobalt oxide nanoplatelets were obtained by thermal decomposition. Nanosized cobalt oxide can also be synthesized by heating polished Co foils in ambient conditions at 200-350 °C²³⁹. But cobalt oxide nanoparticles prepared by this method are irregular in shape. These kinds of high temperature methods usually led to sintering and aggregation of the nanocrystals at the high reaction temperature. Low-temperature synthesis of nanoscale Co_3O_4 has been a recent focus. Various new experimental procedures have been reported in the literature for the synthesis of nanostructured Co_3O_4 at temperatures as low as 150- 260°C. The new low temperature methods include sol-gel²⁴⁰, spray pyrolysis²⁴¹, chemical vapor deposition²²⁹, and hydrothermal reaction

preparation²⁴². With ionic liquid assistance, Co₃O₄ nanoparticles have been formed in solution at room temperature²⁴³. Shape and size control are still a challenge for the synthesis of regular Co₃O₄ nanoparticles.

Co₃O₄ nanoparticles can also be prepared via irradiation. In microwave-assisted synthesis²³³, the reaction temperatures are still as high as 100-140 °C, so the thermal effects produced by microwave irradiation are thought to contribute to the reaction, although some researchers²⁴⁴ believe there are non-thermal effects. In the γ -irradiation method²⁴⁵, investigators claim that Co₃O₄ nanoparticles are prepared at room temperature and ambient pressure. The proposed reaction mechanism was divided into two steps: Co²⁺ is reduced to cobalt atoms by γ -irradiation and then the cobalt atoms are oxidized to Co₃O₄. However, the Co₃O₄ powders produced by this method only show amorphous structure.

UV irradiation is widely used to synthesize Ag, Au and Pt nanoparticles^{190, 246}. Photo-driven processes have some advantages over other methods. Controlled reaction of metal ion precursors can be carried out without using excess reducing agent, for example, and there is no adsorbing contamination in the product. Photo-driven processes are usually slow, such that the reduction reaction arises uniformly in solution and the final product will be more uniform, and the reactions are more controllable. To the best of our knowledge, there are no reports of the synthesis of Co₃O₄ nanorods by UV-irradiation assistant method at room temperature. In this paper, we present a method for the synthesis of water-dispersible Co₃O₄ nanorods by UV irradiation under ambient conditions in aqueous solution. Polyethylenimine (PEI) was used as a stabilizer. The as-prepared Co₃O₄ nanocrystals were systematically investigated using TEM, EDX, Raman and XRD. The method is very simple and provides for the synthesis of 1D Co₃O₄ nanocrystals at room temperature.

4.3 Experiments

4.3.1 Materials

Cobaltous chloride hexahydrate ($\text{CoCl}_2 \cdot 6\text{H}_2\text{O}$) was obtained from Fisher Chemical Company. Polyethylenimine (PEI) with a weight-average molecular weight of 25000 was purchased from Aldrich. All chemicals were used as received.

A Rayonet photochemical reactor (model RPR-600, Southern New England Ultraviolet Inc.) was used for UV irradiation. The photochemical reactor is supplied with eight 253.7 nm light sources (8 W per lamp), a merry-go-round unit which holds samples for equal irradiation rotating at 5 RPM, and a cooling fan to maintain the temperature within the reactor at room temperature.

4.3.2 Preparation of Co_3O_4 nanorods

In a typical procedure, 3 mL of 20 mM CoCl_2 was added to 9 mL PEI aqueous solution (20 mM of the $\text{C}_2\text{H}_5\text{N}$ monomer concentration). The final molar ratio of $\text{PEI}/\text{Co}^{2+}$ was 3. The mixture of aqueous solutions was diluted to 100 mL with deionized water and then was left stirring 2 hours to complete the formation of $\text{Co}^{2+}/\text{PEI}$ complex in quartz tubes. The samples in quartz tubes were placed in the photochemical reactor and irradiated for up to 2000 minutes.

4.3.3 Characterization of Co_3O_4 nanorods

UV-vis absorption spectra of the nanoparticle solutions were measured by a Cary 50 spectrophotometer to pursue the reaction in solution. The as-prepared products' morphology, dimensions and lattice fringes were observed by TEM with a FEI TECNAI F20 microscope. The electron beam acceleration voltage was set at 200 kV. Images were obtained by depositing of a

drop of the final solution onto a carbon-coated 300 mesh copper grid, followed by air-drying under ambient conditions. Particle size distribution was obtained by measuring about 100 particles in arbitrarily chosen areas in the enlarged photograph. The crystallographic information of the samples was identified by X-ray powder diffraction (XRD) analysis with a Rigaku D/MAX-2BX X-ray diffractometer using Cu K α radiation ($\lambda=0.1541874$ nm). The Raman measurements were performed using a LabRam HR800 UV spectrometer (Horiba Jobin-Yvon) with a 633 nm laser line.

4.4 Results and discussion

4.4.1 UV-vis spectroscopic studies

Co₃O₄ nanorods were prepared through a simple UV irradiation process from precursor complexes in aqueous solution. UV-vis spectroscopy was used to monitor the reaction of Co²⁺ ions in solution during photochemical treatment. Figure 4.1 shows the change in the complex UV-vis absorption spectra with increasing UV irradiation time. Formation of Co²⁺/PEI complex is the first step of nanoparticles synthesis. In Figure 4.1, spectrum (a) taken immediately after mixing CoCl₂ with PEI solution shows a typical UV-vis spectra of Co²⁺/PEI complex, with an absorbance peak at 315 nm. This peak is characteristic of an oxygen adduct of a cobalt chelate²⁴⁷. With increasing irradiation time, there is an apparent decrease in the 315 nm peak, which indicates the breaking of the complexation by exposure to the UV light. After about 30 minutes, the peak at 315 nm disappears, indicating the complex is completely dissociated. The irradiation time was extended to as long as 2000 minutes. The dashed line (h) in Figure 4.1 shows the absorption spectra of Co²⁺/PEI complex irradiated for 2000 minutes, which is a relatively flat line showing smooth exponential decay as a function of increasing wavelength with a broad rise

in absorption at long wavelengths. We believe this is attributable to scattering of light associated with the formation of nanoparticles. The spectrum after 2000 minutes exposure of the $\text{Co}^{2+}/\text{PEI}$ complex to UV light yielded no conspicuous changes either in intensity or in maximum absorption. This amount of time appears to be sufficient in obtaining Co_3O_4 nanoparticles.

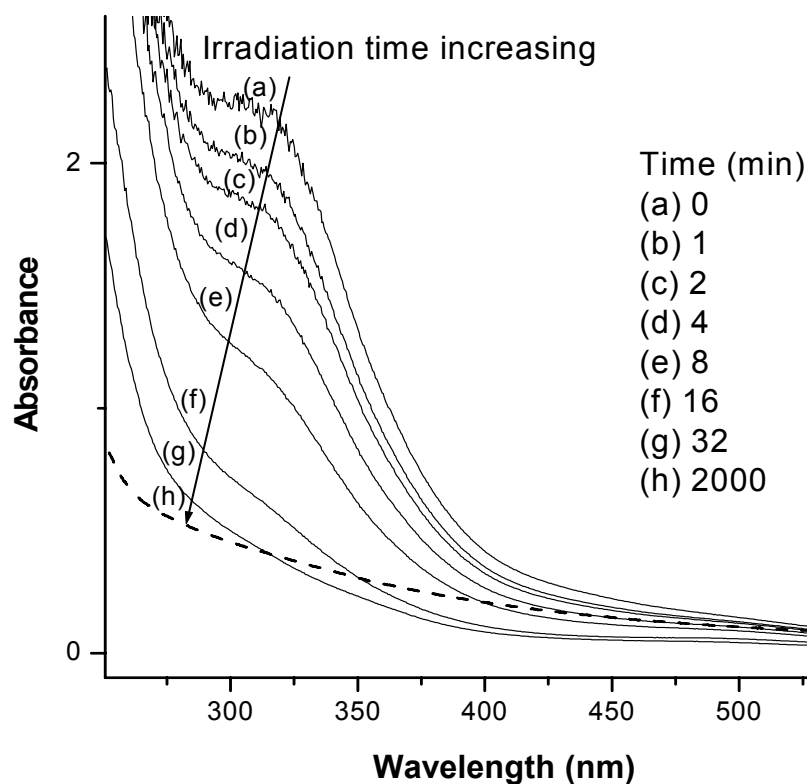


Figure 4.1 Temporal evolution of UV-vis absorption spectra after UV irradiation of $\text{Co}^{2+}/\text{PEI}$ complex.

4.4.2 TEM, STEM and EDX analysis

TEM analysis of the as-prepared samples reveals the presence of nanorods as shown in Figure 4.2. The low-magnification micrograph in Figure 4.2(a) indicates the typical

nanostructures were rod shaped. It appears that a large quantity of nanorods was encapsulated inside the polymer matrix. At this time we are not sure whether the encapsulated structures exist in solution or they form during the drying step of TEM sample preparation. There are a minority of agglomerated nanorods. Imaging statistics of nanorods in Figure 4.2 (b) suggest the length of the rod range from 50 nm to 400 nm, with an average length of 206 nm and standard deviation of 68.6 nm. The average width is 21.8 nm (aspect ratio ~ 10). The agglomerates were not counted in the imaging statistics. Figure 4.2(c) shows a single rod with a smooth surface encapsulated in the polymer matrix at higher magnification. It has a uniform diameter along its entire length, indicating good size and shape control by this method. As shown in Figure 4.2(d), the HRTEM image recorded from an individual nanorod clearly shows a lattice spacing of 0.46 nm, in accordance with the (111) plane of the cubic spinel Co_3O_4 ²⁴⁸. The inset in Figure 4.2(d) is the fast Fourier transform (FFT) pattern of the digitalized HRTEM image. The FFT diffractogram reveals the presence of lattice distances which correspond to the (220) and (111) planes of the cubic spinel Co_3O_4 .

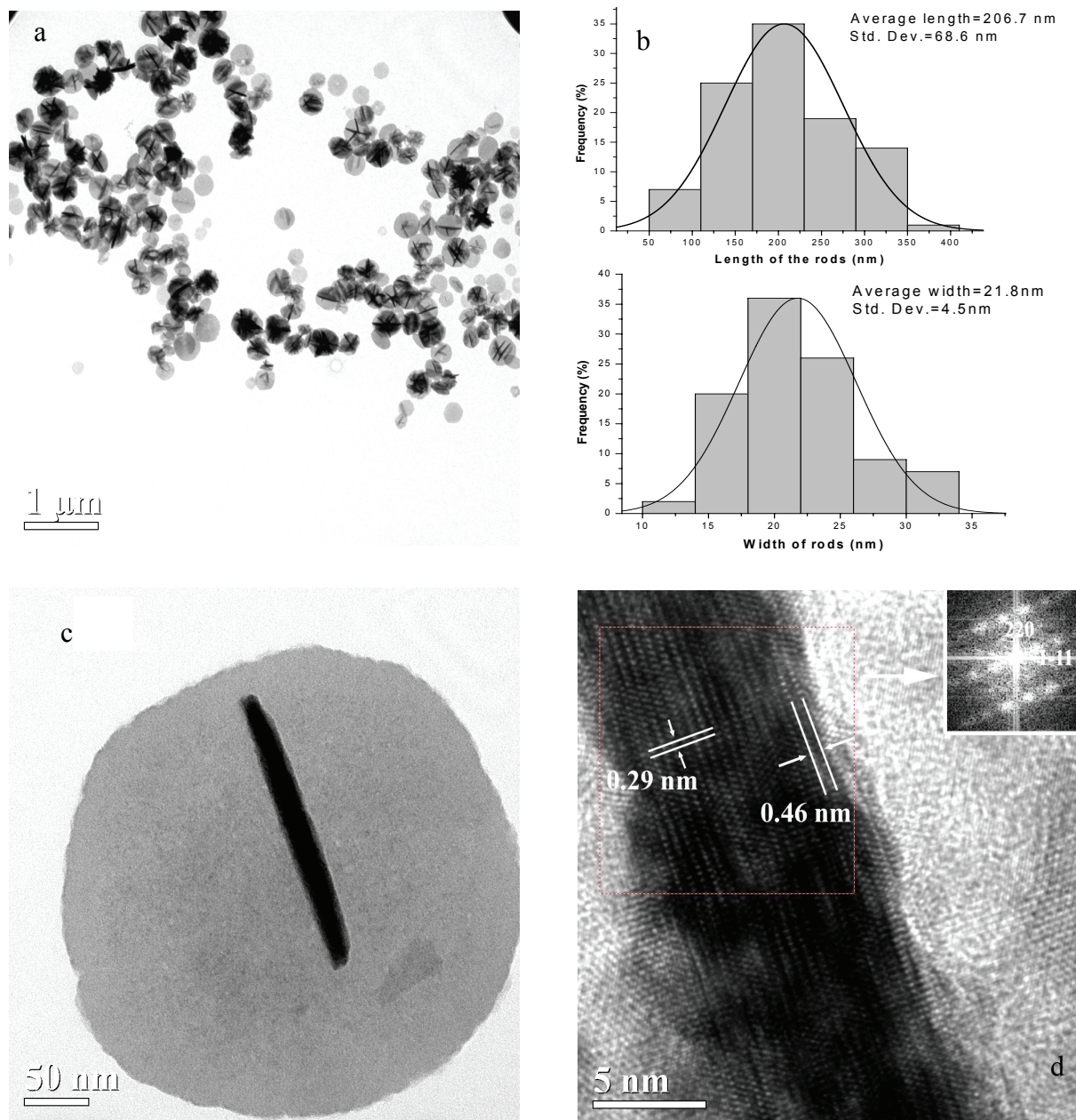


Figure 4.2 TEM characterization of as-prepared Co_3O_4 nanorods (a) low magnification image of Co_3O_4 nanorods coexisting with PEI, (b) length and width distributions of Co_3O_4 nanorods, (c) high magnification image of an individual rod, (d) a high-resolution transmission electron microscope (HRTEM) image taken from the middle part of the rod, (inset: FFT transform of HRTEM image).

Scanning transmission electron microscopy (STEM) investigations has provided further insight into the nanostructures and the chemical composition of the as prepared materials. Figure 4.3(b) shows a STEM image of the nanorods. The image shows several nanorods aggregating in the PEI polymer matrix. The particle size and shape is the same as the TEM result. The spot in the image was selected to obtain an energy dispersive X-ray (EDX) spectrum. The EDX result in Figure 4.3(a) affirms the nanorods consist of cobalt and oxygen. The ratio of cobalt to oxygen is $\sim 3:4$, in agreement with Co_3O_4 stoichiometry. The above results demonstrate that nanoparticles of Co_3O_4 with rod morphology and high aspect ratio can be selectively produced by a UV-assisted method.

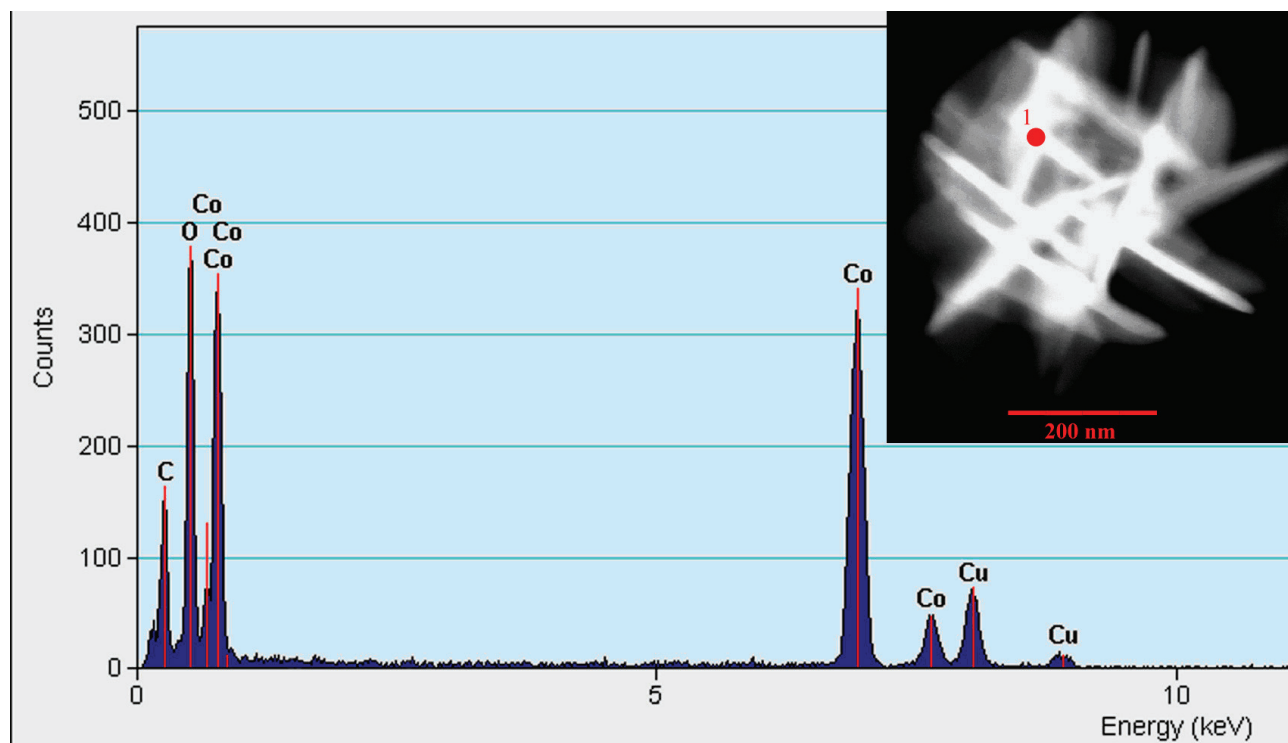


Figure 4.3 EDX spectrum of Co_3O_4 nanorods taken from the spot 1 in the middle of inset STEM image.

4.4.3 XRD and Raman analyses

The crystal structure and phase purity of the product was determined by X-ray diffraction. Figure 4.4(a) shows a typical XRD pattern of the nanocrystals. All diffraction peaks can be exactly indexed to the cubic spinel Co_3O_4 (Space group Fd-3m). The lattice constants of the nanorods ($a=b=c=0.8063$) were in good agreement with standard values (Joint Committee for Powder Diffraction Standards-International Centre for Diffraction Data (JCPDS-ICDD) card no. 74-1657). No impurities can be detected in this pattern, which indicates that pure Co_3O_4 can be obtained under the described synthesis conditions.

In order to further confirm the XRD results, the Co_3O_4 nanorods were also studied by Raman spectroscopy. Figure 4.4 (b) shows the Raman spectrum of the as-prepared Co_3O_4 nanorods. Five distinct peaks were observed. These along with their assignments are given in Table 4.1. It has been shown that Co_3O_4 spinel exhibits a cubic structure, with space group Fd3m (O_h^7). The Raman band at 688.7 cm^{-1} was assigned to the A_{1g} species in the O_h^7 symmetry²⁴⁹. The bands at 620.8 cm^{-1} , 532.5 cm^{-1} and 200.4 cm^{-1} have F_{2g} symmetry, whereas the peak at 482.7 was attributed to the E_g symmetry^{239, 250}. Different samples were measured repeatedly, and only Co_3O_4 Raman spectrum was observed, which confirms the formation of pure Co_3O_4 nanocrystals.

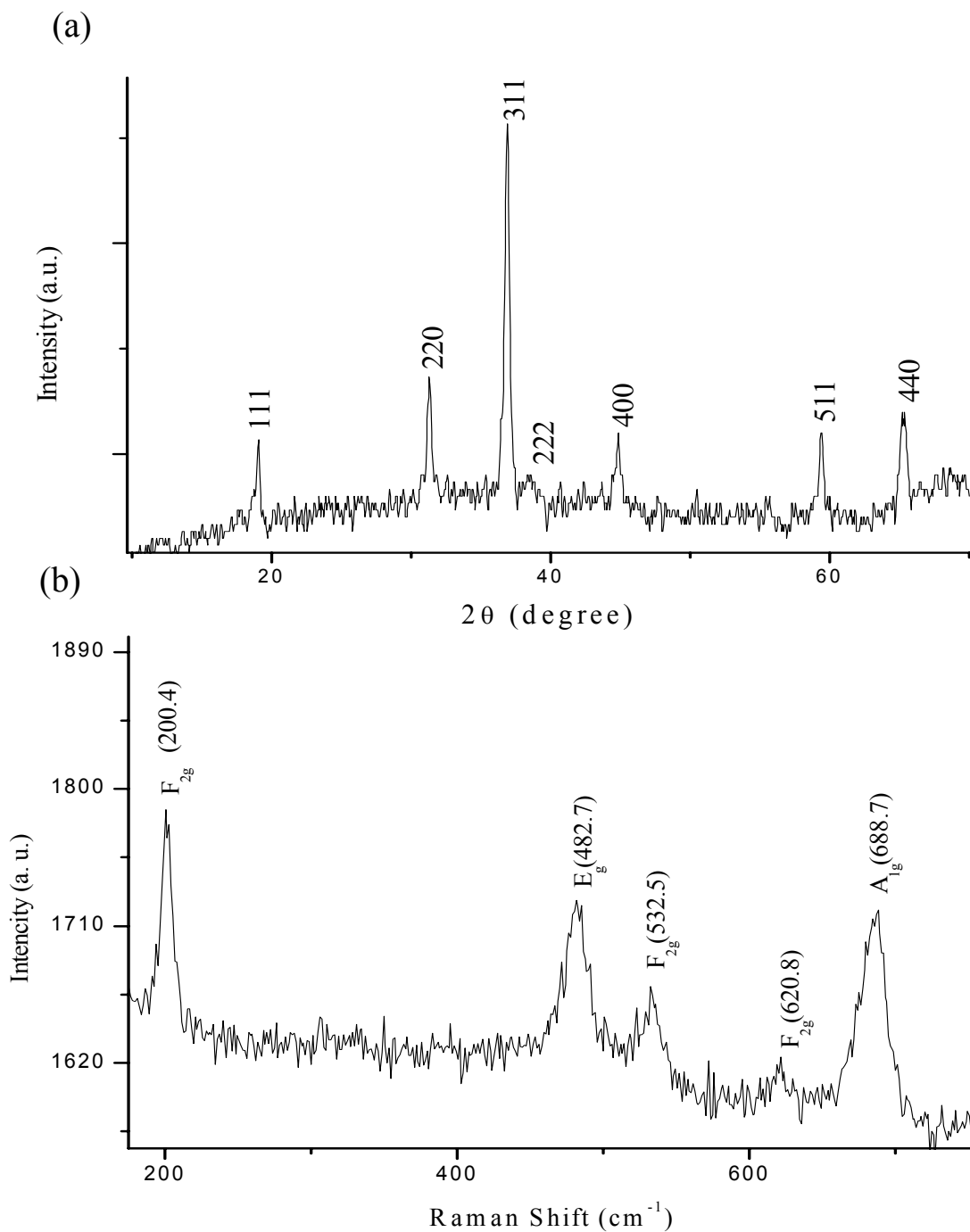


Figure 4. 4 (a) XRD pattern of nanorods, confirming the formation of pure spinel structure cobalt oxide (Co_3O_4), (b) Raman spectrum of the Co_3O_4 nanorods.

Table 4.1 Peak assignments for the Raman spectrum of Co_3O_4 nanocrystals

Peak	Assignment	Observed (cm^{-1})	Ref
1	F_{2g}	200.4	250
2	E_g	482.7	239
3	F_{2g}	532.5	250
4	F_{2g}	620.8	250
5	A_{1g}	688.7	249

4.4.4 Discussion

The formation mechanism of Co_3O_4 nanorods is not immediately clear. The literature²⁵¹ indicates that PEI shows very high ability coordinate cobalt ions, and the $\text{PEI}/\text{Co}^{2+}$ complex is one of metal complexes with oxygen-binding properties. The $\text{PEI}/\text{Co}^{2+}$ complex is capable of binding oxygen in 2:1 and 1:1 stoichiometries. UV-vis spectra in Figure 4.1 show this feature at 315 nm. When $\text{PEI}/\text{Co}^{2+}$ complex binds with oxygen and external energy is provided, an electron can transfer from cobalt to the oxygen. This oxygenation reaction can be viewed as a internal redox reaction: Co^{2+} is formally oxidized and the oxygen is formally reduced²⁵². Irradiation with 254 nm light can cause the photochemical decomposition; the O-O bonds break and free radicals can be detected²⁵³.

To confirm this mechanism, a comparison experiment was done at pH 3. It is known that the formation of the oxygen complex only occurs at pH 5 and above. This is due to strong competition by protons for the basic coordination sites on the ligand which prevents formation of the cobaltous chelates at lower pH. TEM results (Figure 4.5) show that although reduction

apparently occurs, there are no nanorods formed at pH 3. To investigate the effect of O_2 , experiments were carried out with PEI/ Co^{2+} solutions purged with nitrogen gas and compared with those through which air was bubbled prior to irradiation. The solution bubbled with nitrogen gas show very few nanorods in the TEM images while the solution bubbled with air produces many nanorods. The appearance of a small amount of Co_3O_4 nanorods indicates that oxygen was not completely removed from the solutions prior to irradiation, or some oxygen is absorbed due to imperfect quartz tube sealing. Examining the crystal structure and the above experimental results, we may propose a hypothesis for the formation of Co_3O_4 nanorods as shown in Figure 4.6: PEI was complexed with cobalt ions which bind with O_2 in solution. UV irradiation gives sufficient activation energy to transfer electrons from cobalt to oxygen. The complexes decompose and subsequently cobalt was oxidized to Co_3O_4 in the aqueous solution. The oxidizing agent is likely the dissolved oxygen in solution, which binds with PEI/ Co^{2+} complex. Further studies are still underway to confirm this mechanism.

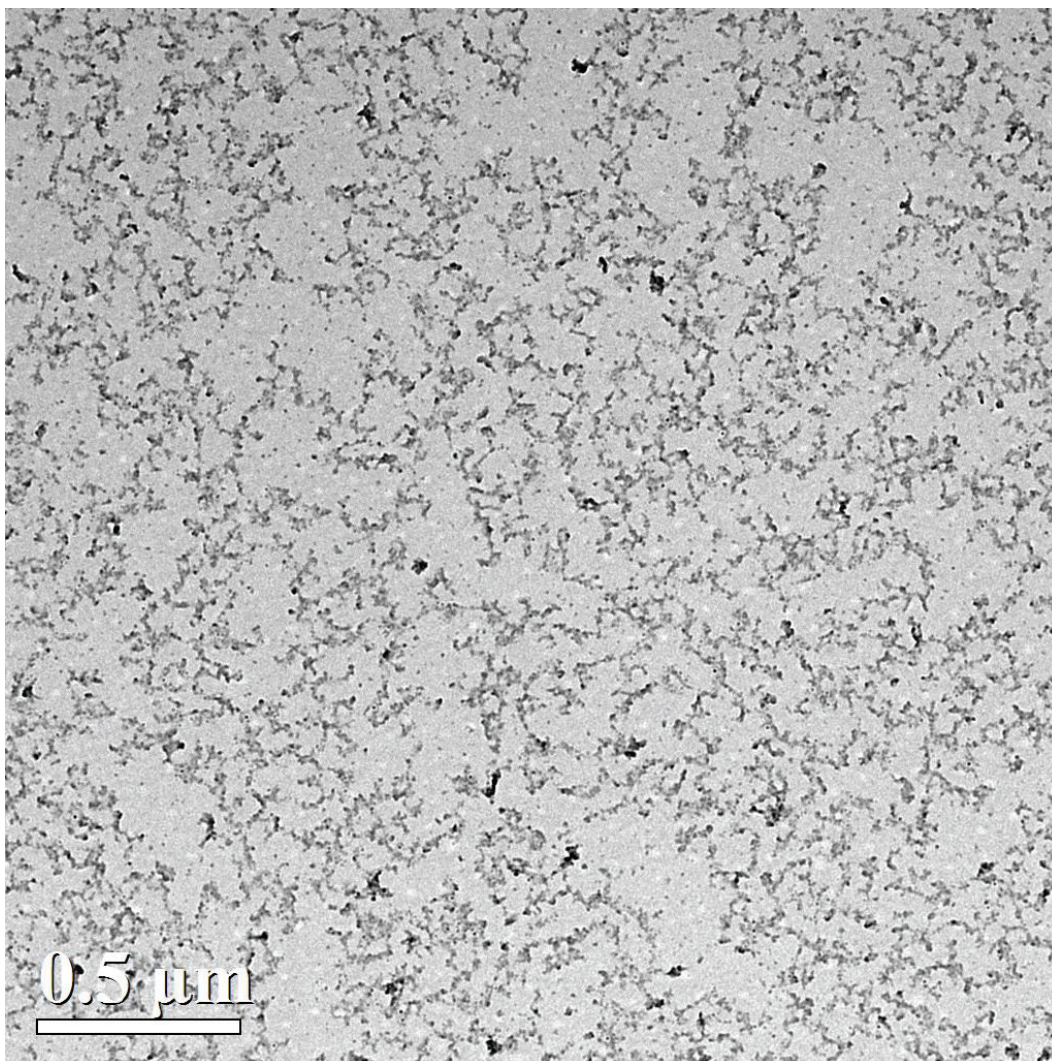


Figure 4.5 TEM image of CoCl_2 and PEI mixture at pH 3, irradiation with UV light for 34h. There is apparently no feature bigger than 40 nm in the image.

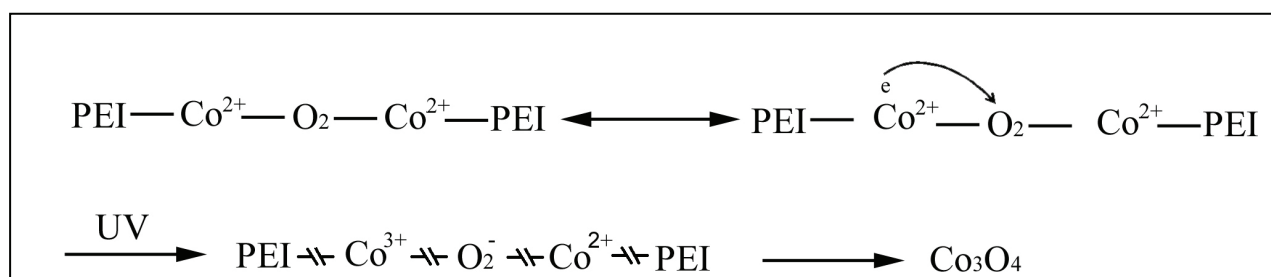


Figure 4.6 Proposed formation process for Co_3O_4 .

Further investigations on the influence of PEI in the synthesis of Co_3O_4 nanorods and confirmation of the reaction mechanism have been performed. These studies indicate that the morphology and size of the final product strongly depends on the molar ratio of PEI to Co^{2+} . As shown in Figure 4.7(a), when the molar ratio of PEI to Co^{2+} is 0.5:1, there are no detectable nanoparticles apparent in the TEM image. In Figure 4.7(b), when the molar ratio reaches 1:1, nanoparticles are observed. Experiments show that the optimum molar ratio of PEI to Co^{2+} for the formation of nanorods is 3:1. At this ratio, the synthesized nanorods show a smooth rod shape. When the molar ratio of PEI to Co^{2+} is higher than 3:1, shown in Figures 4.7(e), the nanorods are not smooth and aggregation occurs. When the ratio of PEI to Co^{2+} reaches 6, as shown in Figures 4.7(f), very few nanorods are formed, possibly because cobalt complexed with six nitrogen ligands appears to be much less efficient in complexing oxygen²⁵⁴. There is a strong relationship between the synthesis of nanorods and the molar ratio of PEI to Co^{2+} .

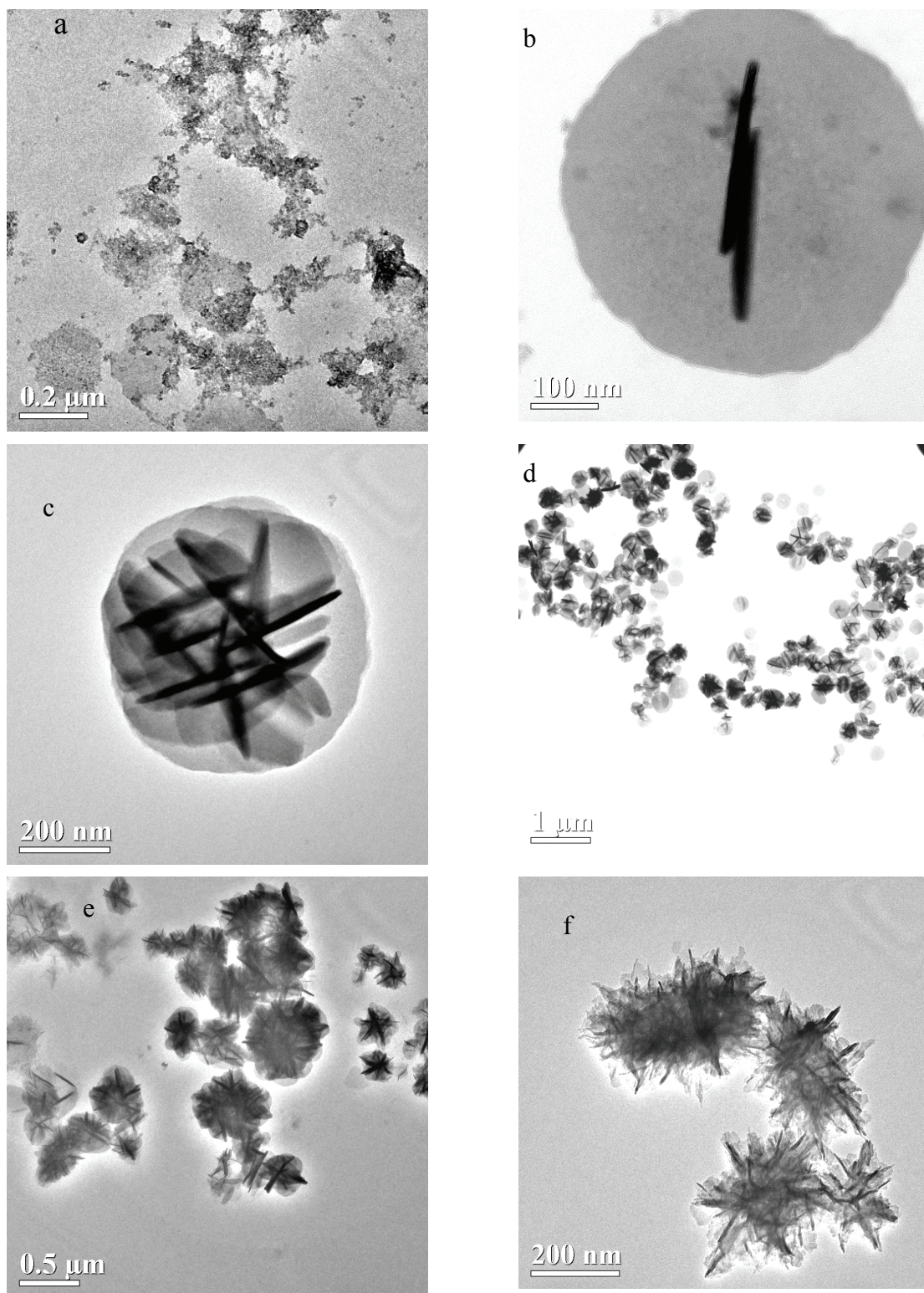


Figure 4. 7 TEM micrographs of Co_3O_4 prepared at different molar ratios of PEI to Co^{2+} : (a) 0.5:1, (b) 1:1, (c) 2:1, (d) 3:1, (e) 4:1, (f) 6:1.

4.5 Conclusions

Co_3O_4 nanorods were successfully prepared by a UV-assisted method in aqueous solution at room temperature and ambient pressure. This is the first known report of UV -assisted, room-temperature synthesis of crystalline spinel Co_3O_4 nanomaterials. The phase of the product was identified by XRD and no impurity was present. Nanorod morphology of Co_3O_4 was confirmed by TEM. A possible formation mechanism was proposed. Further studies are underway to confirm this formation mechanism. Unlike traditional chemical synthesis methods, the reactions all occur at room temperature. This method has the virtue of simplicity, mild reaction conditions, and leads to highly crystalline particles with controllable morphology. With uniform morphology, the Co_3O_4 nanorods obtained have great potential application. This approach, which is not simply the photoreduction of precursor metal ions to zerovalent metal but rather a photo-driven process from a complexed intermediate, could provide a strategy for the synthesis of other nanosized transition metal oxide materials.

CHAPTER 5 Preparation of FePt Nanoparticles by Chemical Reduction in PAMAM-OH Template

5.1 Synopsis

Using dendrimers as templates, FePt nanoparticles with narrow size distribution were prepared by a simple chemical reduction method at room temperature. In this approach, PAMAM-OH dendrimers act as templates in which metal ions are coordinated in, and NaBH₄ acts as reductant. The FePt nanoparticles were synthesized in aqueous solution. The as-made FePt nanoparticles are spherical with an average size of ~3 nm and have the chemically disordered face-center-cubic (fcc) structure. The FePt nanoparticles can be transformed to the face-center-tetragonal (fct) phase after annealing at 700 °C for 1 hour. The as-prepared fcc FePt nanoparticles are found to be superparamagnetic at room temperature. After annealing in a reducing atmosphere, the FePt nanoparticles transform to ferromagnetic and show high coercivity. The structural and magnetic properties of the as-made and annealed samples were characterized by transmission electron microscopy (TEM), X-ray diffraction (XRD), and alternating gradient magnetometry (AGM).

5.2 Introduction

Dendrimers are very attractive materials in nanotechnology and nanoscience because of their highly ordered structure, narrow size distribution and chemical versatility²⁵⁵. There are many types of dendrimers. Poly(amidoamine) (PAMAM) is one of the most widely used commercially available dendrimer. For high generation PAMAM dendrimers, they possess a high concentration of surface functional groups. The crowding surface functional groups lead to a close-packed spherical structure surrounding significant interior cavities²⁵⁶. The high density of

interior tertiary amines in PAMAM dendrimers can complex metal ions based on electrostatic interactions or complexation reactions²⁵⁷. In suitable condition, metal ions can be complexed exclusively within the dendrimers. After the metal ions are encapsulated, they can be reduced by excess of chemical reducing agent in water to yield zero-valent encapsulated nanoparticles²⁵⁸. This type of synthesis is kinetically controlled, and it does not produce broad size distributions associated with the thermodynamics of nucleation and growth. As templates, dendrimers themselves with fairly uniform composition and structure can yield nanoparticles with well-defined size and shape. So dendrimers are ideal monodisperse molecular-level reactors for nanoparticle syntheses.

Because of significant technological applications, magnetic nanomaterials have been intensively studied to develop a better understanding of their fundamental properties^{69, 259}. Magnetic nanoparticles with high magnetocrystalline anisotropies and coercivities can be used for future magnetic high-density recording applications, and high performance permanent magnets²⁶⁰, while superparamagnetic or ferromagnetic nanoparticles with low coercivities can be used in biotechnology (such as: bioseparation, biosensors, etc)^{261, 262}. Synthesis of high quality magnetic nanoparticles with desired shape and size is a prerequisite to investigate and utilize their properties. Narrow size distribution is highly desirable because magnetic properties are strongly size dependent in nanometer size range. Recently, magnetic nanoparticles including Co, Ni, CoPt, FePt and Fe₃O₄ have been prepared by solution phase synthesis²⁶³⁻²⁶⁶.

Single-phase FePt nanoparticles are especially interesting because of their high crystalline anisotropy, high saturation magnetization, and desired chemical stability. These good properties of FePt nanoparticles have inspired synthetic advances. However, synthetic approaches for preparing monodisperse FePt in 10 nm size range are very limited. Chemical routes using

organic solvents with surfactants are the most widely synthesis method for the preparation of Pt alloy nanoparticles²⁶⁷. These methods have many attractive features, such as their ease of synthesis, narrow size distribution, and chemical stability²⁶⁸. The particles are commonly synthesized via either simultaneous co-reduction of iron salt and platinum acetylacetonate, Pt(acac)₂, thermal decomposition of iron pentacarbonyl, Fe(CO)₅, or the reduction of Pt(acac)₂ in a polyol and mixed surfactants^{267, 269}. The polyol process that utilizes diol or polyol to synthesize metal particles is a good example of these kinds of approach. In this process, it is believed that Pt plays a critical role in accelerating the co-reduction of Fe species, which are considered to be difficult to reduce on their own through the polyol process. However, Fe(CO)₅ is a highly toxic, flammable liquid at room temperature. Besides the safety concerns, there are other disadvantages associated with iron pentacarbonyl which arise from its low boiling point. The reaction temperature is above the boiling point, so some of the iron is lost and not incorporated into the FePt alloy nanoparticles. Therefore the stoichiometry of the FePt particles is difficult to control by this method. The as-prepared FePt nanoparticles normally show a chemically disordered face-centered cubic (fcc) structure and are superparamagnetic at room temperature. Thermal annealing at temperatures above 500°C can converts fcc FePt to a face-centered tetragonal (fct) structure, which shows a higher magnetocrystalline anisotropy associated with a very high coercivity²⁷⁰. However, conversion of as-synthesized fcc particles to the fct phase by thermal annealing to 500°C can lead to particle agglomeration, leading to increases in both size and size dispersion²⁷¹.

Although preparative routes to magnetic FePt nanoparticles are established, most of FePt nanoparticles prepared in organic solvents are poorly water soluble. A great effort has been spent to prepare FePt in aqueous media. Most of them involve surfactant or hydrothermal synthesis.

For example, Gibot et al²⁷² synthesized CoPt and FePt nanoparticles by reduction of metallic salts with surfactant at 70 °C. Caiulo et al²⁷³ prepared glucose-encapsulated FePt by hydrothermal at 180 °C. Zeng et al²⁷⁴ tried to synthesize FePt without surfactant at room temperature, but only loosely held aggregates were formed. So Gibot²⁷² conclude that FePt nanoparticles prepared in aqueous or biphasic medium always appeared to have coalesced into spongelike agglomerates. The agglomerates deteriorate their properties and limit their applications. In our research, hydroxyl-terminated PAMAM dendrimers were used as templates to synthesize FePt nanoparticles. Terminal hydroxyl group eliminates the restrictive pH window necessitated by selective protonation, size was controlled and aggregation was avoided.

In this chapter, the synthesis of FePt nanoparticles in aqueous media at room temperature using PAMAM dendrimers as templates and NaBH₄ as reductant was studied. The as-made 3 nm nanoparticles from dendrimer template method are soluble and stable in aqueous solution. These as-made nanoparticles have the chemically disordered fcc structure and can be transformed to the chemically ordered fct phase by annealing. The structure and magnetic properties of the annealed samples were characterized and compared with as-synthesized FePt nanoparticles.

5.3 Experimental

5.3.1 Materials

H₂PtCl₆, FeSO₄, and NaBH₄ were purchased from Aldrich Chemical Company. They are used as received without further purification.

5.3.2 Preparation of FePt nanoparticles

A co-complexation and chemical reduction method was used to prepare dendrimer-mediated FePt nanoparticles. The syntheses were carried out using a standard airless technique in

nitrogen atmosphere. In a typical procedure, 1 mL of 20 mM FeSO₄ and 1 mL of 20 mM H₂PtCl₆ was mixed together and was added to 10mL 0.1 mM of Generation 4 hydroxyl-terminated PAMAM dendrimer (G4-OH) aqueous solution. G4-OH dendrimers are approximately 4.5 nm in diameter in solution and contain 64 end groups. The stoichiometric ratio of Fe to Pt was 1: 1. The molar ratio of total metal ions to the dendrimers was 40. The aqueous mixture was stirred and bubbled with nitrogen for 2 hours at room temperature. Then a 10-fold excess of 10 ml freshly prepared aqueous NaBH₄ solution was added dropwise to the mixture. In minutes, the solution changed to a dark black color. The reaction occurred at room temperature.

The dendrimer mediated FePt nanoparticles were thermally annealed in a quartz tube furnace for further characterization. Annealing transforms FePt nanoparticles from the chemically disordered fcc phase to the ordered fct phase, giving FePt nanoparticles with high magnetocrystalline anisotropy and ferromagnetism. But, the annealing will also result in the decomposition of the dendrimer around FePt nanoparticles into carbonaceous matrix. The annealing process was carried out under 95% Ar + 5% H₂ at temperatures ranging from 500 to 700 °C and duration of 60 minutes.

5.3.3 Characterization of dendrimer mediated FePt nanoparticles

The nanoparticles morphology and size were observed by TEM with a FEI TECNAI F20 microscope. The electron beam acceleration voltage was set at 200 kV. Images were obtained by depositing a drop of the particle solution onto a carbon-coated 300 mesh copper TEM grid, followed by air-drying under ambient conditions. Particle size distribution was obtained by measuring about 100 particles in arbitrarily chosen areas in the enlarged photograph. Samples for XRD and magnetic measurements were obtained by evaporating FePt particle solution on Si

wafers at room temperature. The crystallographic information of the samples was identified by X-ray powder diffraction (XRD) analysis with a Philips X'pert diffractometer in the Bragg-Brentano (θ - 2θ) geometry, using a Ni-filtered line-focused Cu K α X-ray source. Room temperature magnetic hysteresis curves were measured using a Princeton Micromag 2900 alternating gradient magnetometer (AGM).

5.4 Results and discussion

5.4.1 Morphology analysis

The as-prepared FePt nanoparticles synthesized via dendrimer template were studied by TEM. Figure 5.1 is a representative bright field TEM image and corresponding size-distribution histograms of as-prepared FePt nanoparticles. Analysis of the TEM images reveals that the as-prepared nanoparticles are spherical and uniform in size. The low magnification micrograph in Figure 5.1(a) indicates the nanoparticles are well separated although there is a minority of overlapping regions because of TEM sample preparation. High resolution TEM studies (Figure 5.1 inset) show that the FePt nanoparticles have uniform lattice fringes across the nanoparticles, which is attributed to the good crystalline quality of these nanoparticles. These kinds of particles are expected to be a single magnetic domain and exhibit superparamagnetic properties. Imaging statistics in Figure 5.1(b) suggest the monodispersity of the FePt nanoparticles. Fit with a log-normal distribution, an average diameter of 3.0 nm and a standard deviation of 0.4 nm were measured. The overlap regions were not counted in the diameter statistics. The particles have a fairly uniform diameter, indicating good size control by this method. To confirm that dendrimers play an important role in the preparation of FePt nanoparticles, a comparison experiment was done with same condition except without any PAMAM in the system. Figure 5.1(c) show the as-made FePt without dendrimers. It shows sponge-like agglomeration structure with several

hundred nanometer feature. So dendrimers is essential in the preparation of size controlled FePt nanoparticles. Since the dendrimer matrix is not visible, we are not sure whether all of the particles are inside the dendrimer molecules at this time. G4 PAMAM dendrimers are approximately 4.5 nm in diameter in solution. It can be found that almost all of the FePt nanoparticles size is smaller compared with the size of G4 dendrimer. So FePt nanoparticles may form inside of dendrimer template.

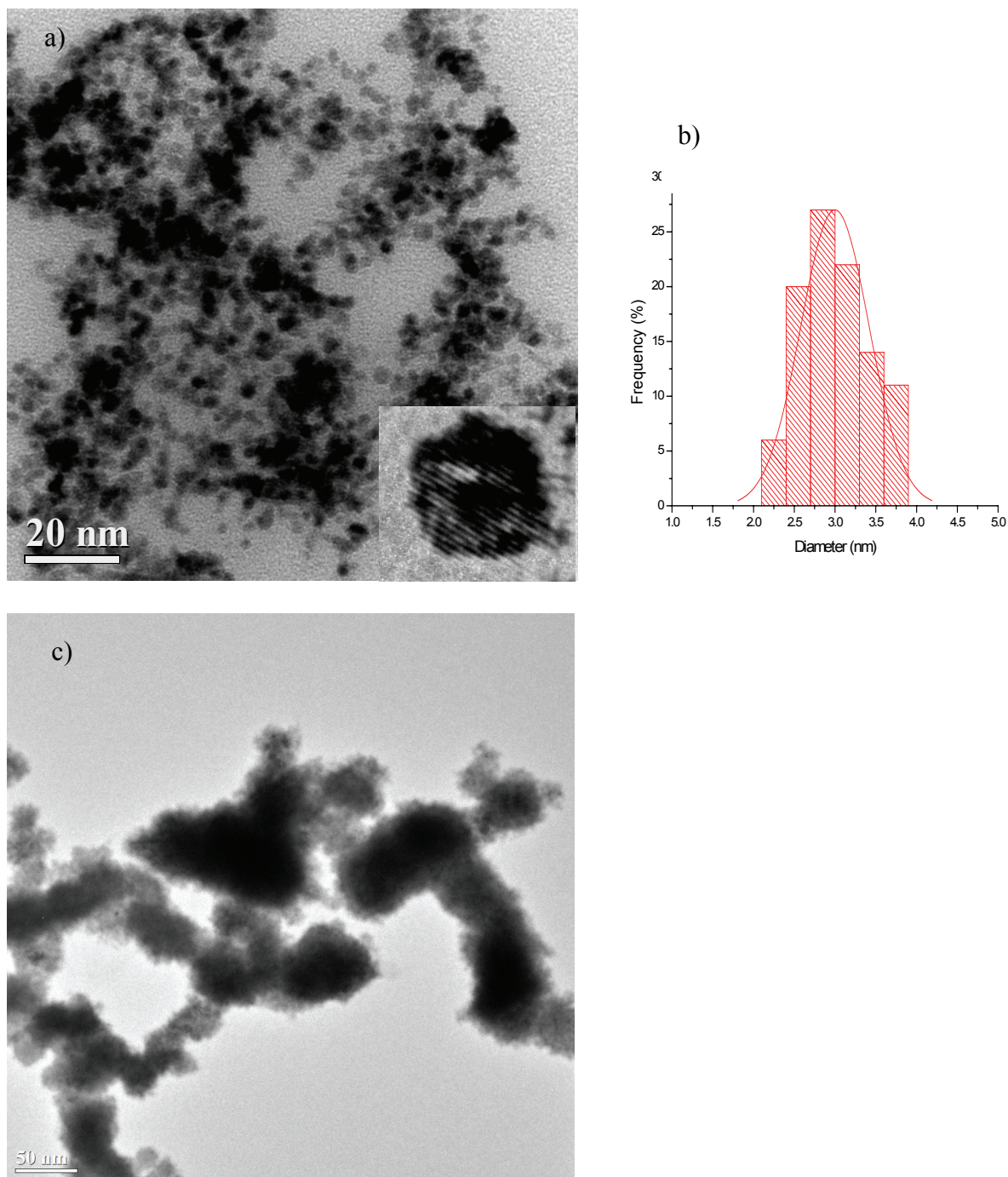


Figure 5.1 TEM images of as-prepared FePt nanoparticles, inset shows HRTEM of the same sample depicting the crystalline nature of the sample, b) Particle size distribution, curve fitting is based on the assumption of a log-normal distribution. c) TEM images of as-prepared FePt nanoparticles without dendrimers.

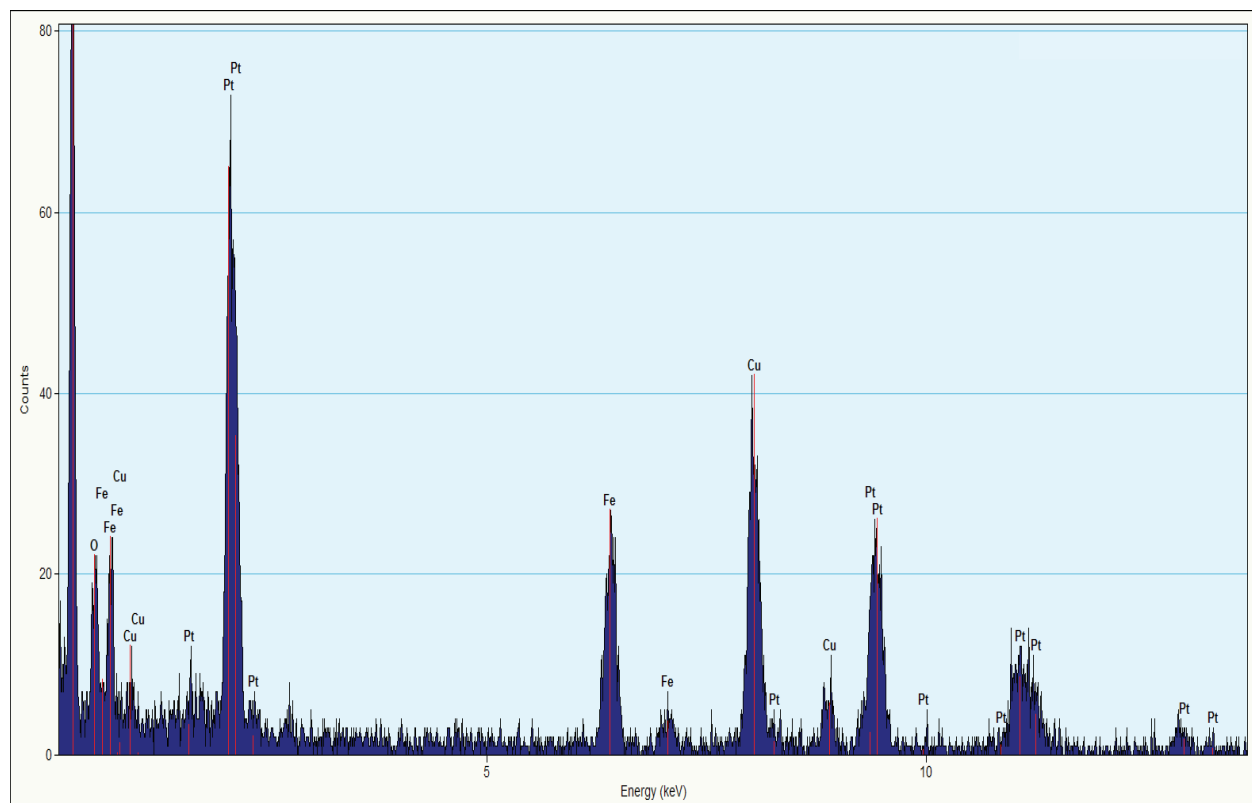


Figure 5.2 EDX of as-made PAMAM-OH mediated FePt nanoparticles.

As shown in Figure 5.2, single particle EDX was done to test the composition of as-made particles. Cu signal in Figure 5.2 come from TEM grids. Analysis show the percentage of Fe is $45.5 \pm 0.8\%$ and percentage of Pt is $54.5 \pm 2.6\%$. Pt/Fe ratio is pretty close to 1:1 which is preferred to form L10 phase with high anisotropy.

The surface of the as-made FePt nanoparticles was examined by XPS measurements. Figure 5.3 gave out the survey scan of the as-made sample. It clearly shows the Fe and Pt signal. The Si signal comes from the substrate. Figure 5.4 show the high resolution C1s peak in FePt. As seen in the figure, C1s was composed of three components, which is corresponds to three kind of chemical environments of C in dendrimer: C-C; C-N; and C-O. For the case of Fe, it shows a broad line with a significant shift in binding energy. It is worth to noting that two components

were found for Pt 4f in the as-made FePt nanoparticles (Figure 5.5). A binding energy of 71.3 eV is the typical state of Pt⁰ metal. Another component at 72.4 eV is the nonzero charge state²⁷⁵. This state only can be found in the composite state indicating the existence of charged atoms due to coordination bonds with dendrimer ligands. Sun et al²⁷⁶. reported that amine and carboxylate ligands form coordination bonds with FePt nanoparticles and that Fe tends to bind with -OOC, while Pt binds to NH₂.

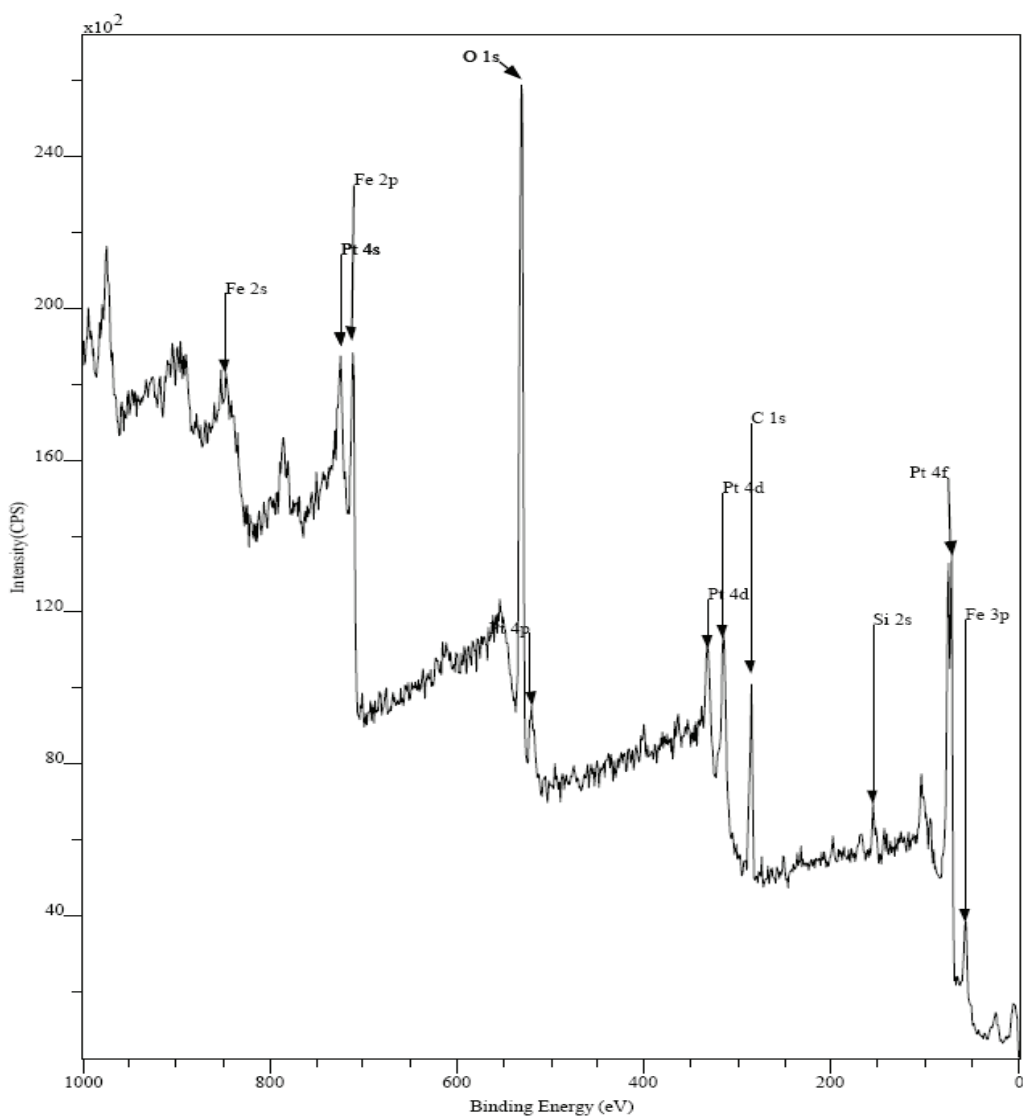


Figure 5.3 XPS of as-made FePt nanoparticles.

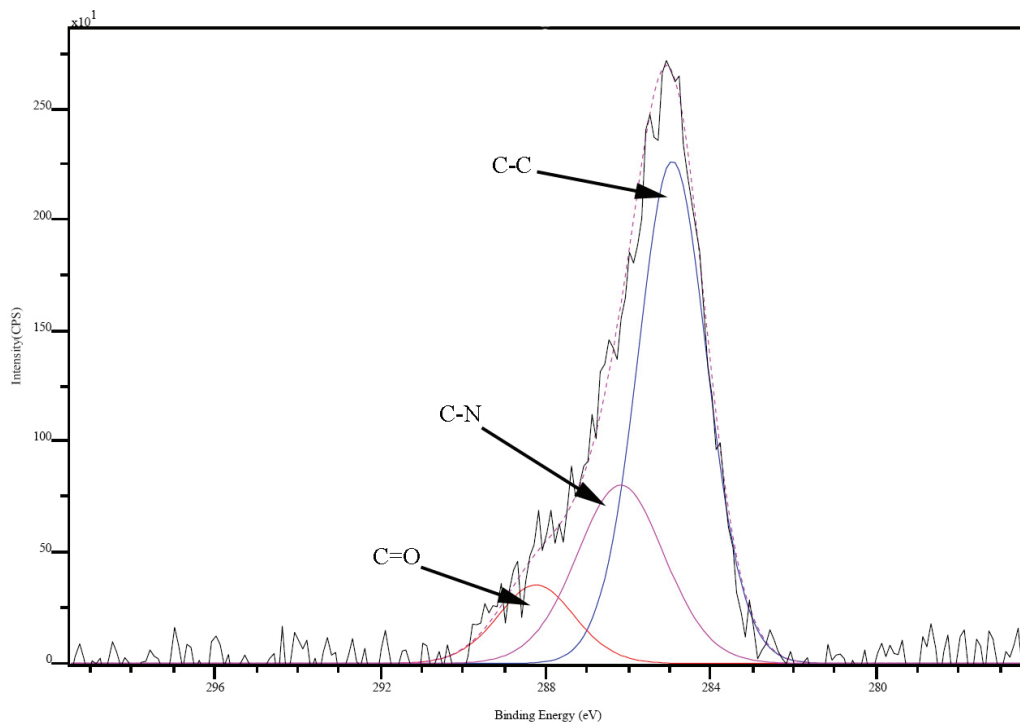


Figure 5.4 XPS of C1s for as-made FePt nanoparticles.

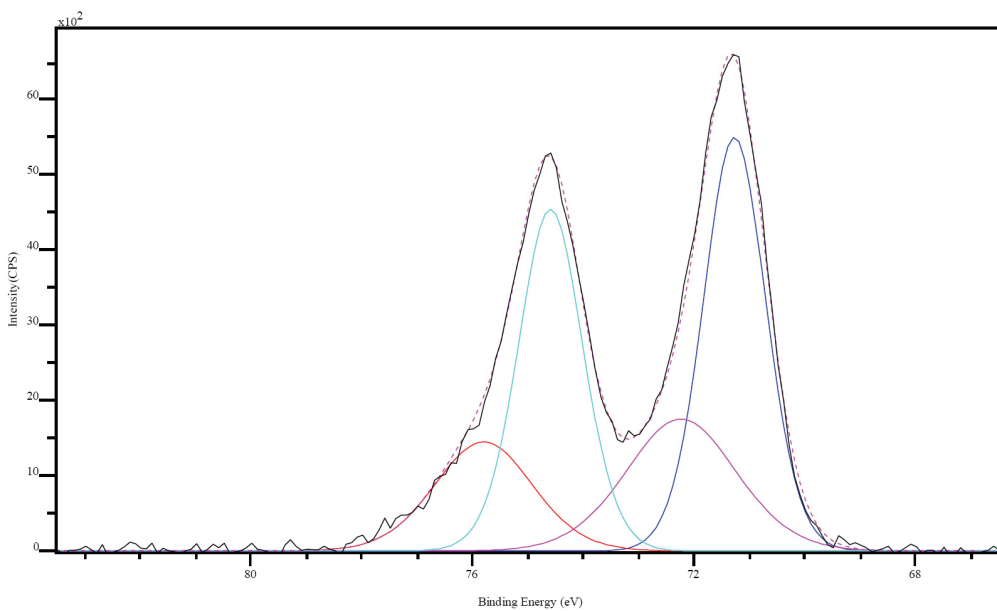
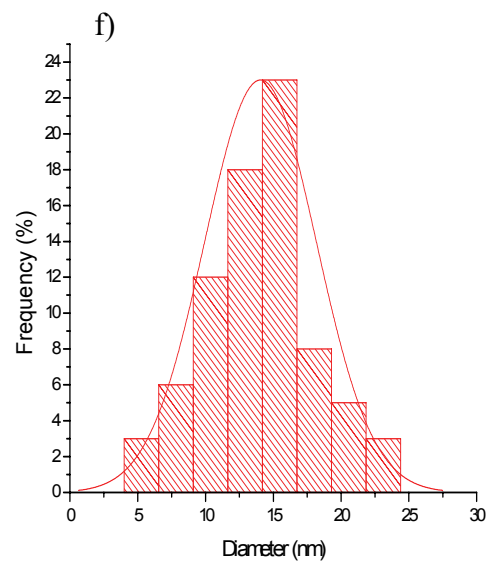
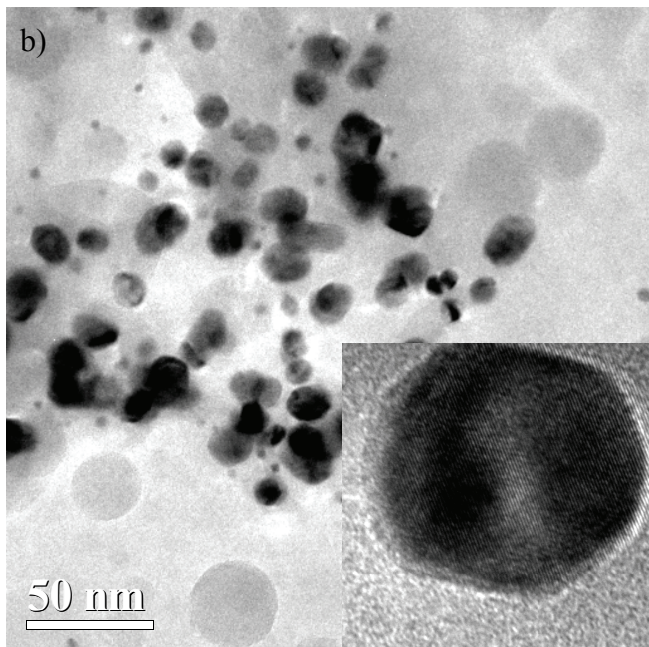
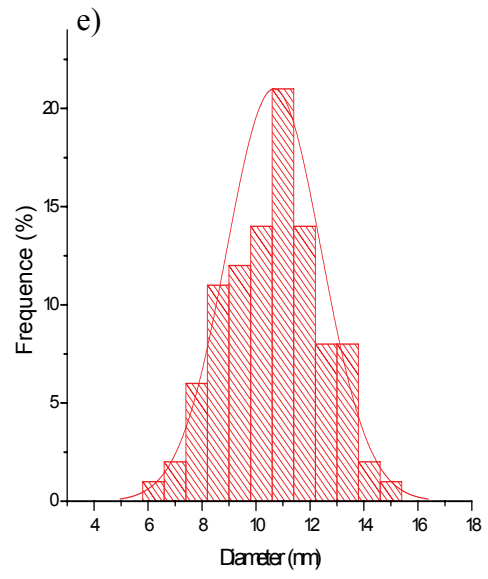
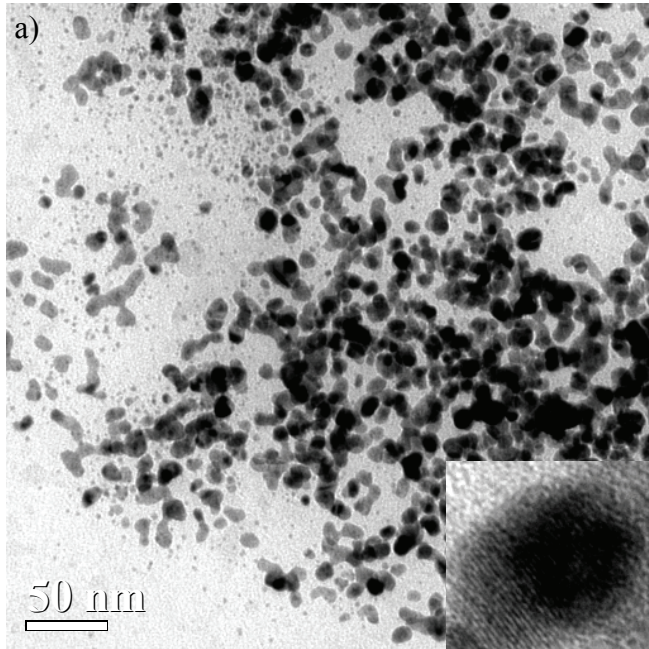


Figure 5.5 XPS of Pt 4f for as-made FePt nanoparticles.

5.4.2 Annealing induced particle sintering

High temperature annealing can lead to particle aggregation. Figure 5.6 (a), clearly shows the morphology of FePt nanoparticles annealed at 500°C under 5% hydrogen and 95% argon for 1 h. According to the literature²⁷⁶, using 5% hydrogen and 95% argon as the reducing atmosphere can reduce the iron oxide layer present around each FePt nanoparticle. The average diameter of FePt nanoparticles increases from 3 nm to 10.7±1.7 nm. At this temperature, the dendrimer will decompose and only leave carbonaceous residue. As shown in the TEM image, sintering occurs at this temperature, and the sizes of FePt nanoparticles increase. Figure 5.6 (b) shows the FePt nanoparticles annealed at 600°C for 1h. Heating the specimen at this temperature will result in further coalescing of nanocrystals: The size of the FePt nanoparticles increased to 14.1±4.1 nm. The inset in Figure 5.6 (b) is a high resolution TEM image which shows clear lattice fringes of the FePt nanocrystal. The interplane spacing is 0.219 nm, consistent with the {111} lattice planes of fct FePt. The average particle size slightly increases further with increasing annealing temperature to 700°C. As shown in Figure 5.6 (c), the diameter of FePt nanoparticles increased to 15.4±5.8 nm. The detailed structure of a single FePt nanoparticle annealed to 700 °C was characterized with HRTEM, as shown in Figure 5.6 (d). The lattice fringes of the FePt nanoparticle are clearly shown in the image with adjacent fringe spacing of 0.195 nm corresponding to {200} lattice planes of fct FePt. Figure 5.6(h) is the Fast Fourier transformation (FFT) of the HRTEM image of Figure 5.6(d), which consistent with the fct structure projected from the [001] direction.



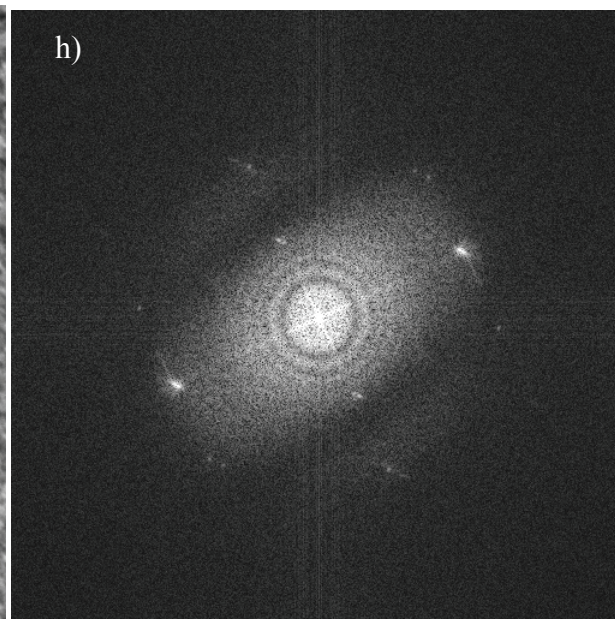
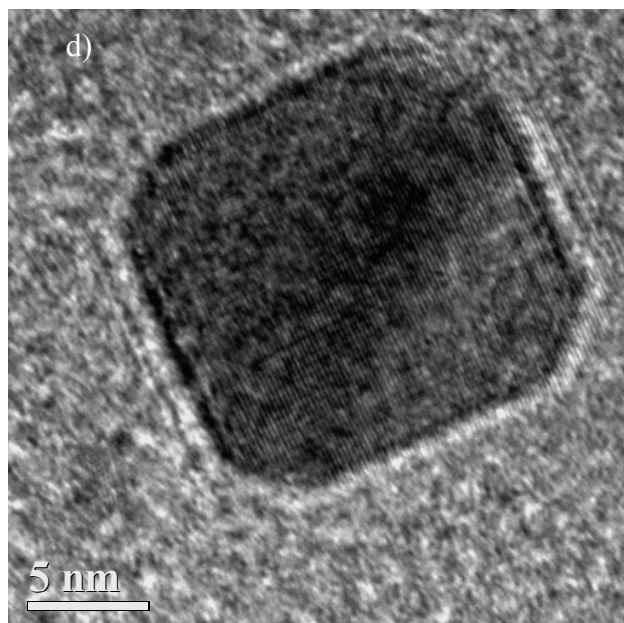
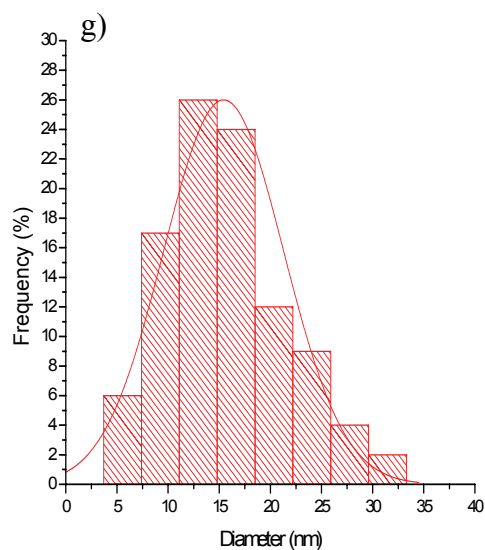
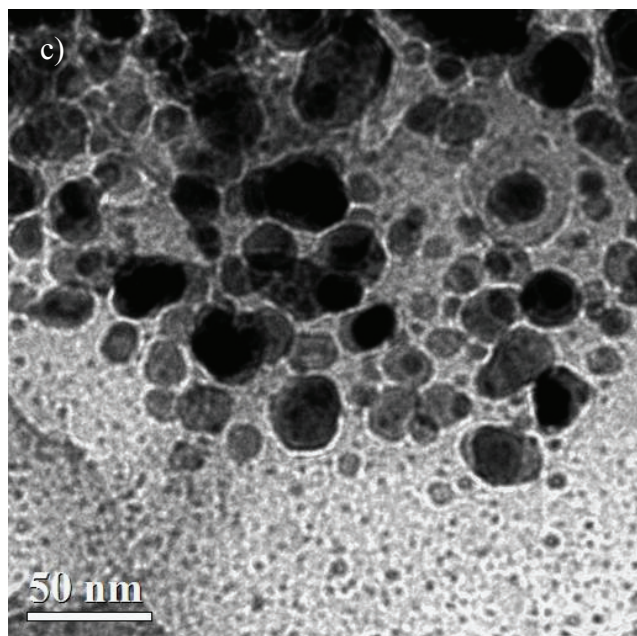


Figure 5.6 (a)TEM images of FePt nanoparticles annealing at 500 °C for 1h; (b) at 600 °C for 1h, (c) at 700 °C for 1h; (d) HRTEM image of a single fct-FePt nanoparticle annealing at 700 °C for 1h with interfringe spacing at 0.195nm; (e) Particle size distribution of sample (a); (f) Particle size distribution of sample (b); (g) Particle size distribution of sample (c); (h) FFT of the corresponding HRTEM image (d).

Both the size of the particles and their size distribution are affected by the annealing temperature. Figure 5.7 shows size and size distribution of FePt nanoparticle as a function of annealing temperature. It can be found that both the size and size distribution of FePt nanoparticle increase with the increasing annealing temperature. This means that although the high temperature is needed to transform the fcc FePt to fct FePt, but the high annealing temperature will make the size bigger and distribution much broader than as-prepared FePt nanoparticles. To prevent agglomeration of the FePt nanoparticles, silica or other material can be coated outside of dendrimer mediated FePt nanoparticles before annealing²⁷⁷. Dendrimer is an ideal template with good compatibility with other materials^{278, 279}.

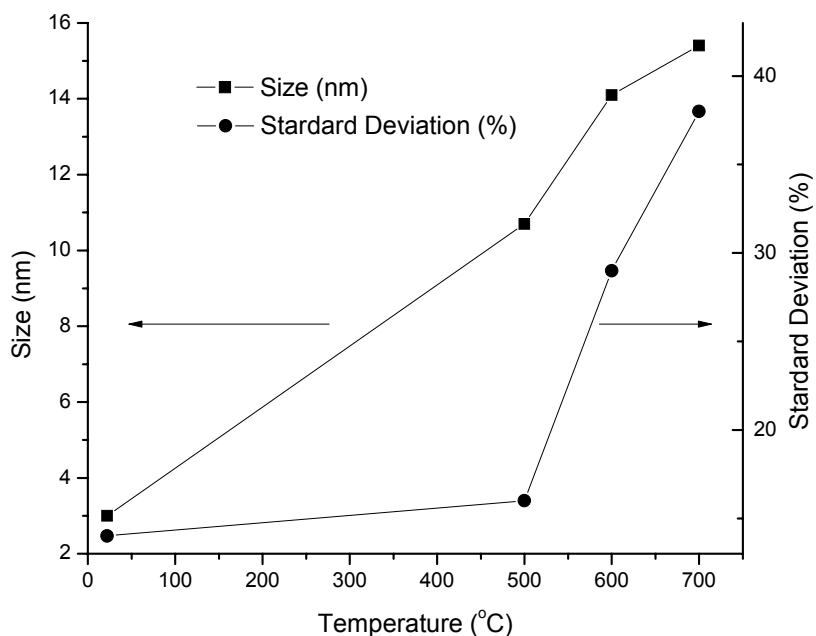


Figure 5.7 Effect of annealing temperature on the average particle size and standard deviation.

5.4.3 Structural analysis of the FePt nanoparticles

The crystal structure of the FePt nanoparticles was determined by X-ray diffraction (XRD). As shown in Figure 5.8 (a), X-ray diffraction of the as-synthesized FePt particles reveals a typical chemically disordered fcc structure, in which Pt atoms are substituted into Fe positions and vice versa. Annealing induces the Fe and Pt atoms to rearrange into the long range chemically ordered fct structure, which can be viewed as a natural superlattice of alternating Fe and Pt atomic planes. The change in the particle structure upon annealing depends on annealing temperature and other factors such as annealing time, Fe/Pt ratio etc. Figure 5.8 (b) shows the XRD for the FePt nanoparticles annealed for 60min at 500 °C. Careful examination of curve b in Figure 5.8 shows that the (111) peak is shifted to high angle and the (002) peak begins to appear, which means that the onset of phase change apparently occurs at about 500 °C. This result is consistent with previous observations of FePt nanoparticles prepared by other methods. Further increase in the temperature to 600°C, (001) and (110) peaks become apparent, as shown in Figure 5.8 (c). Scans of FePt nanoparticles annealed at 700 °C in Figure 5.8 (d) clearly shows the typical superlattice peaks of (001) and (110) that are characteristic of the ordered FePt ($L1_0$) compound phase. The lattice constants of the FePt nanoparticles ($a=3.8417$) are in good agreement with standard values (Joint Committee for Powder Diffraction Standards-International Centre for Diffraction Data (JCPDS-ICDD) card no. 65-1051). Therefore, annealing caused the Pt and Fe atoms to rearrange into a chemically ordered fct structure.

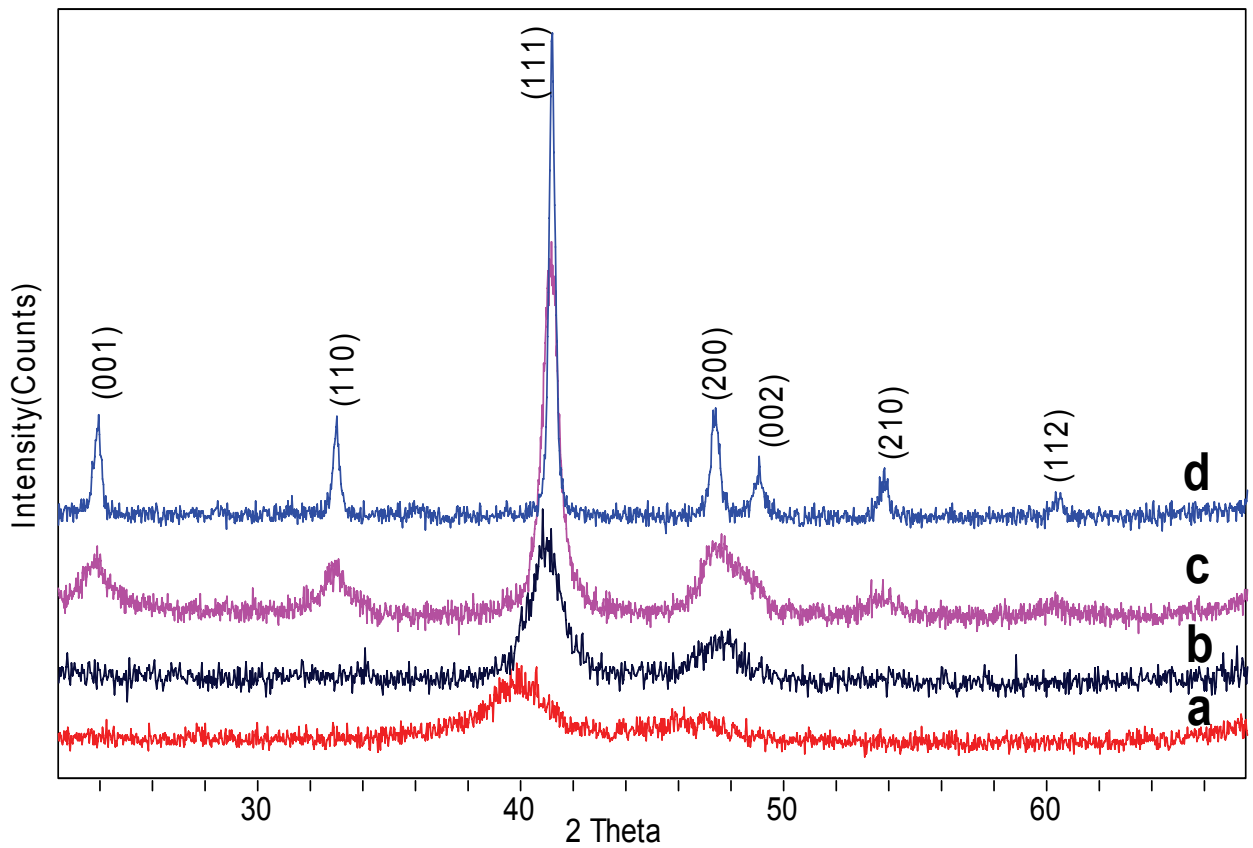


Figure 5.8 X-ray diffraction patterns of FePt nanoparticles: a) as-synthesized and a series of samples annealed under Ar/H₂ (5%) for 1 hour at temperatures of (b) 500, (c) 600, and (d) 700 °C.

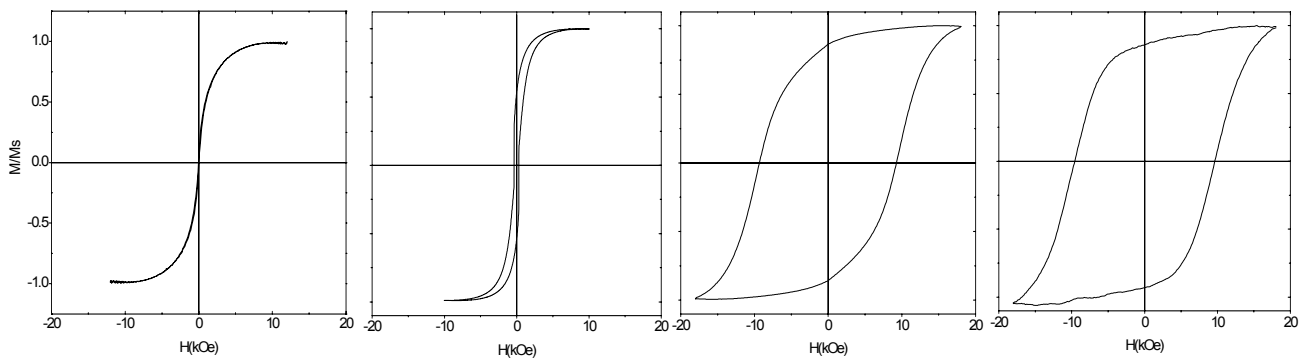


Figure 5.9 Hysteresis loops of FePt nanoparticle a) as-prepared, b) annealed at 500 °C, c) annealed at 600 °C, d) annealed at 700 °C.

5.4.4 Magnetic properties

It is well-known that the coercivity of FePt nanoparticles strongly depends on the degree of chemical ordering as well as particle size²⁸⁰. Along with the phase change, magnetic properties can be easily tuned. The magnetic properties of FePt nanoparticles were studied by AGM at room temperature. Figure 5.9 gives the hysteresis loops of dendrimer-mediated FePt nanoparticles annealed in different temperature. Here, M/M_s represents the normalized saturation magnetization. From the XRD result, the as-prepared as-synthesized FePt nanoparticles were confirmed to be chemically disordered fcc structure, and magnetic measurements in Figure 5.9 (a) confirmed that the as-synthesized FePt nanoparticles are superparamagnetic at room temperature with $H_c \approx 0$, consistent with the low magnetocrystalline anisotropy of the fcc structure. The thermal annealing transforms the chemically disordered fcc structure to the chemically ordered fct structure. The coercivity of the annealed FePt nanoparticle increases with temperature, and a minimum annealing temperature of about 500 °C under an Ar with 5% H₂ atmosphere are required to form ferromagnetic FePt nanoparticles. This corresponds to the structure transformation from the fcc phase to the fct phase at this temperature. Figure 5.9 (b) is the hysteresis loop for 1 hour annealed sample in 500 °C whose coercivity reaches 325.4Oe at room temperature, consisting with a small portion of the nanoparticles having sufficient anisotropy to be ferromagnetically ordered at room temperature. For the 600 °C annealed sample, the coercivity is greatly increased to 9298Oe. This is an agreement with FePt phase transforming with increasing of annealing temperature indicated in Figure 5.8. Annealing at 700 °C can yield typical FCT FePt nanoparticles with coercivity of 9668Oe, in agreement with the high magnetocrystalline anisotropy of the fct phase.

Figure 5.10 shows the room temperature coercivity as a function of annealing temperature for dendrimer mediated FePt nanoparticles. The coercivity value increases dramatically after 500 °C, consistent with XRD data. It should be noted that the coercivity increasing not only dependent with phase change but also with the size growth due to coalescence, as confirmed by the TEM images.

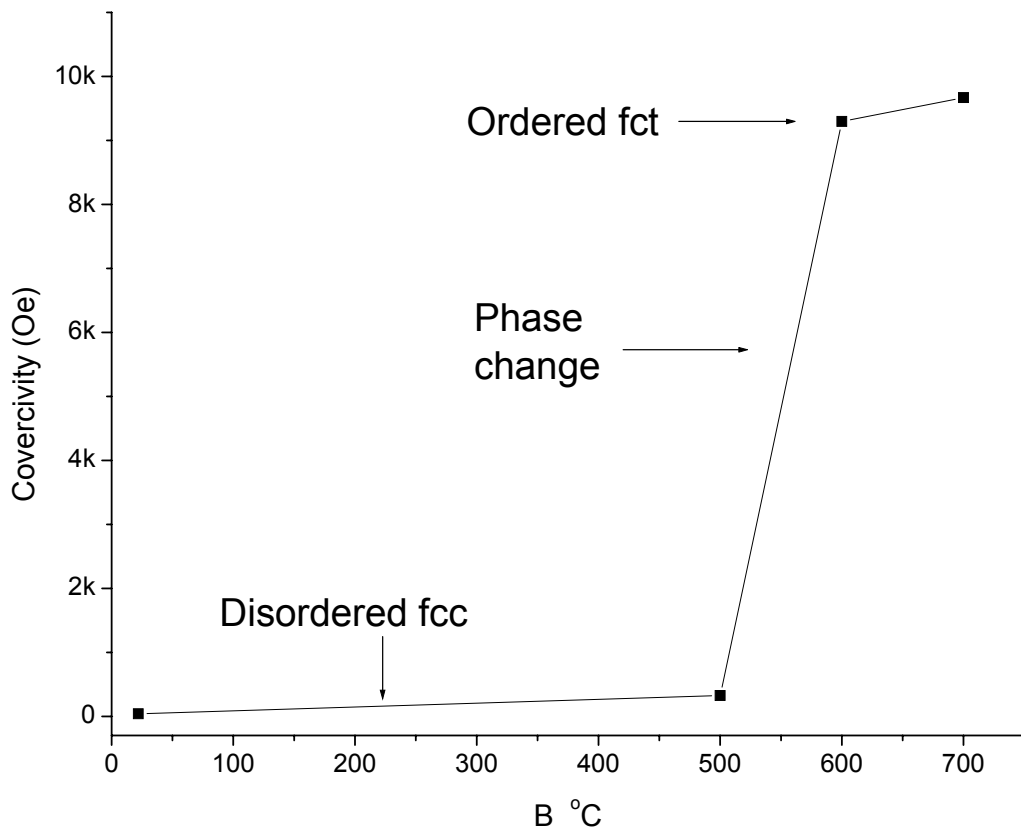


Figure 5.10 Room-temperature of coercivity values as a function of annealing temperature for dendrimer mediated FePt nanoparticles.

5.5 Conclusions

Monodisperse dendrimer mediated 3 nm FePt nanoparticles was synthesized by reduction of FeSO_4 and H_2PtCl_6 in the presence of the dendrimer template using superhydride as the reducing reagent in aqueous solution at room temperature. The as-prepared FePt nanoparticles are chemically disordered with the fcc phase. Thermal annealing induces change in particle structure from chemically disordered fcc to chemically ordered fct and transforms FePt nanoparticles from superparamagnetic to ferromagnetic. Magnetic hysteresis measurements show a coercivity as high as 1T at room temperature for the annealed FePt nanoparticles. The dendrimer template method provides an alternative approach to synthesize monodisperse FePt nanoparticles at room temperature and gives good water compatibility to the FePt magnetic nanoparticles. The well-defined dendrimer mediated magnetic nanoparticle synthesized by chemical reduction method in aqueous solution may be suitable for various multifunctional magnetic nanomaterials applications.

CHAPTER 6 The Enhanced Coercivity for Dendrimer Mediated Multicomponent Magnetic Microspheres

6.1 Synopsis

Dendrimer mediated CoPt alloy nanoparticles were successfully encapsulated in silica microspheres by a multistep technique. Monodisperse CoPt nanoparticles were prepared with PAMAM-OH dendrimer templates by a chemical reduction method, and silica coating was accomplished via sol-gel reaction. These multicomponent spheres exhibit multicore-shell structures. The size of the multicore-shell structured spheres can be effectively tuned by reaction condition. The silica coating is shown to isolate and protect the dendrimers mediated CoPt nanoparticles. The synthesized multicore-shell nanoparticles were characterized by high resolution transmission electron microscopy (HRTEM), EDS and AGM. Magnetic measurements indicate that the magnetic properties multicore-shell microspheres can be effectively modulated by the silica coating process.

6.2 Introduction

The synthesis of ultrasmall magnetic nanoparticles with uniform size distribution has been the focus of an increasing amount of the recent literatures because of their extensive technological applications which include single-bit elements in high-density magnetic data storage arrays, magnetic fluids, magnetic resonance imaging, biology and medicine^{31, 65, 281, 282}. Particularly, superparamagnetic nanoparticles have generated considerable interest because of their special features and applications in biomedicine²⁸³⁻²⁸⁸. But pure magnetic particles still suffer from a lot of shortcomings which limit their practical applications²⁸⁹, such as: (i) naked

magnetic nanoparticles tend to form large aggregates due to magnetic dipole moment, (ii) some magnetic materials such as Co, Ni-based can be biohazardous and also not stable at ambient condition resulting in the alteration of magnetic properties and (iii) they undergo biodegradation when they are directly exposed to the biological system. Thus coating of magnetic nanoparticles with biocompatible polymer may favorite their biomedical applications²⁹⁰⁻²⁹². As shown in last chapter, ultrasmall superparamagnetic alloy nanoparticles can be synthesized within dendrimer templates. FePt and CoPt nanoparticles^{293, 294} with the chemically ordered fct structure have been considered as best candidates for fabricating next-generation information storage media. However the as-made FePt or CoPt nanoparticles typically have the chemically disordered face centered cubic (fcc) structure, which exhibit low magnetic corcivity³¹. High temperature anneals is necessary to transform the disordered fcc phase to the fct phase to improve their magnetic properties. But their original shape changed and size increased in the annealing process. It is well known that the size and shape of nanoparticles plays an important role in determining the magnetic properties. Hence an increased interest in coating their surface with a protecting shell^{295, 296} to control over the particle size and dispersity with tunable coercivity, obviate particle coalescence upon annealing²⁸⁹. Coating with silica will provide a better chemical stability. Knecht et al^{279, 297} have investigated encapsulation of dendrimers with silica. Their result proved that PAMAM dendrimers can been utilized as both a host for Au⁰ nanoparticle synthesis and an active agent for silica condensation. The resulting product yields mesoporous silica nanospheres of 80-nm diameter supporting randomly distributed gold nanoparticles. Dendrimer may also provide a media to stabilize magnetic alloy nanoparticles and used as a template to grow silica microspheres. Coating magnetic alloy nanoparticles with silica can provide a model to

investigate magnetic behavior of magnetic nanoparticles due to new surface, interparticle, and exchange interactions in magnetic/nonmagnetic matrix.

In this chapter, silica encapsulated CoPt with multicore-shell structure was fabricated with a multistep technique. A chemical reduction process was first used to synthesize ultrasmall spherical shape CoPt nanoparticles by the chemical reduction of $\text{CoCl}_2 \cdot 6\text{H}_2\text{O}$ and H_2PtCl_6 with NaBH_4 in the presence of PAMAM dendrimers. Then a Stober synthesis was used to encapsulate the dendrimer mediated CoPt nanoparticles. The magnetic and structural properties of the dendrimer mediated CoPt and silica multicore-shell microspheres were systematically investigated.

6.3 Experimental

6.3.1 Materials

H_2PtCl_6 , FeSO_4 , NaBH_4 , ethanol and tetramethyl orthosilicate (TEOS) were purchased from Aldrich Chemical Company. Ammonia (30%) was purchased from Fisher Scientific. All of chemicals were used as received without further purification.

6.3.2 Preparation of CoPt@silica nanoparticles

Dendrimer mediated CoPt nanoparticle Synthesis. Dendrimer mediated CoPt nanoparticles were prepared before condensation of silica. A co-complexation and chemical reduction method was used to prepare dendrimer-mediated CoPt nanoparticles. In a typical procedure, 10 mM of an aqueous solution of $\text{CoCl}_2 \cdot 6\text{H}_2\text{O}$ and H_2PtCl_6 were mixed with 0.1 mM of Generation 6 hydroxyl-terminated PAMAM dendrimer (G6-OH) (Aldrich). The stoichiometric ratio of Co to Pt was 1: 1. The molar ratio of total metal ions to the number of surface groups of the dendrimers was 1: 4. The aqueous mixture was stirred and bubbled with nitrogen for 2 hours at

room temperature. Then a 10-fold excess of freshly prepared aqueous NaBH_4 solution (10 ml) was added dropwise to the mixture. In minutes, the solution changed to a dark black color. The reaction occurred at room temperature.

Silica encapsulation of CoPt nanoparticles. Silica encapsulation was realized by Stober method. In a typical experiment, 10 ml dendrimer mediated CoPt aqueous solution was mixed with 40ml ethanol. 2 ml concentrated ammonia was added to the mixture. To that, TEOS was added and the reaction was taken in a ultrasonic cell for 60 min at room temperature. Once complete, the reaction mixture was centrifuged for 5 min (12K RPM) to form a pellet which was washed copiously with DI water.

6.3.3 Characterization of silica encapsulation of CoPt nanoparticles

The nanoparticles morphology and size were analyzed by TEM with a FEI TECNAI F20 microscope. The electron beam acceleration voltage was set at 200 kV. Silica nanosphere samples were suspended in water and then drop onto a carbon-coated 300 mesh copper TEM grid, followed by air-drying under ambient conditions. Particle size distribution was obtained by measuring about 100 particles in arbitrarily chosen areas in the enlarged photograph. Energy-dispersive X-ray spectrometry (EDS) was obtained using an EDAX package integrated onto the TEM. Samples were tilted at 15° for analysis at 200 kV during STEM analysis. Samples for magnetic measurements were obtained by evaporating Silica nanosphere solution on Si wafers at room temperature. Room temperature magnetic hysteresis curves were measured using a Princeton Micromag 2900 alternating gradient magnetometer (AGM).

6.4 Results and discussion

6.4.1 Characterization of as made dendrimer mediated CoPt nanoparticles

The as-made dendrimer mediated CoPt nanoparticles were firstly analyzed by TEM. Figure 6.1 is a representative bright field TEM image, size distribution histogram and corresponding diffraction pattern of as-prepared FePt nanoparticles. TEM image indicates that the nanoparticles are well separated with uniform sized spherical particles of ~3.5 nm in diameter. In some region of TEM image, clear lattice fringes can be observed, which indicate the good crystalline quality of these nanoparticles. The diffraction pattern shows the formation of the chemically disordered fcc structure. The dendrimer matrix is transparent in TEM image thus it cannot be simply discerned whether the particles are inside or outside of the dendrimer molecules²⁹⁸. So these nanoparticles were either entrapped within the interior of the dendrimer or surface passivated by select dendrimers which leave numerous surface function groups of the dendrimer template available for silica condensation reactivity

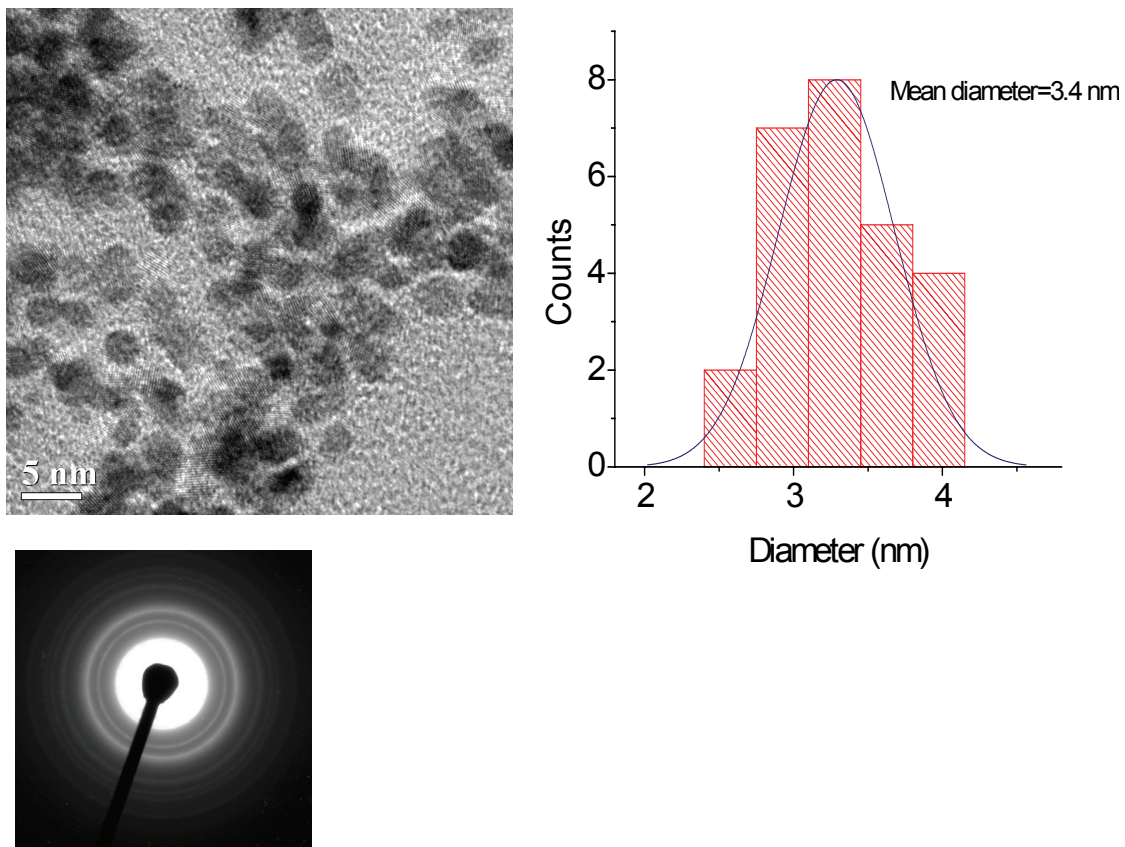


Figure 6.1 TEM image, size distribution and diffraction pattern of as-made dendrimer mediated CoPt nanoparticles.

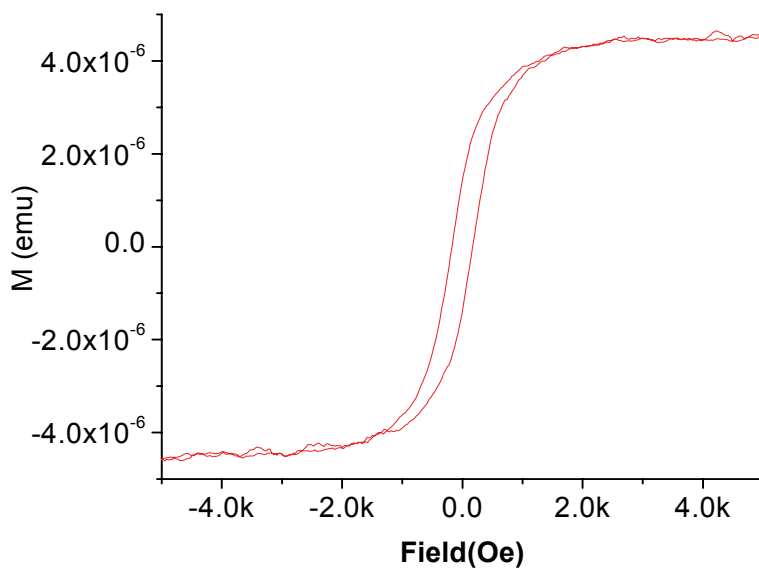


Figure 6.2 Magnetic loops of as-made dendrimer-coated CoPt nanoparticle.

Magnetic hysteresis loops of as-made dendrimer-mediated CoPt nanoparticle was shown in Figure 6.2. The as-made loop has low coercivity of 168 Oe since the particles have the disordered fcc phase at room temperature.

6.4.2 Characterization of silica encapsulated CoPt nanoparticles

The dendrimer mediated CoPt nanoparticles aqueous solution was mixed with ethanol with a ratio of 1:4 which provide the media for the silica polycondensation reaction. Silica condensation reaction occurs almost immediately after adding TEOS which can be observed from the color change of the solution. Once the reaction complete the product was centrifuged and washed with water to remove excess unreacted chemicals. Silica encapsulation of the dendrimer-supported CoPt nanoparticles was evident by the isolation of a gray precipitation after centrifugation.

The resulting multicomponent nanocomposite was analyzed using TEM and AGM. The effect of TEOS concentration for CoPt silica core shell particles was investigated with different amount of TEOS starting materials. Sample 1-3 was prepared with 0.05, 0.1, 0.2 ml TEOS respectively. TEM images of the composite material revealed individual CoPt nanoparticles are well dispersed throughout silica nanospheres. As shown in Figure 6.3, different amount of TEOS result in different size of silica microspheres. Analysis of these images shows that the nanoparticle dispersity remained the same before and after encapsulation (3.4 nm) which suggests that the silica encapsulation did not lead aggregation or coagulation of dendrimer mediated nanoparticles.

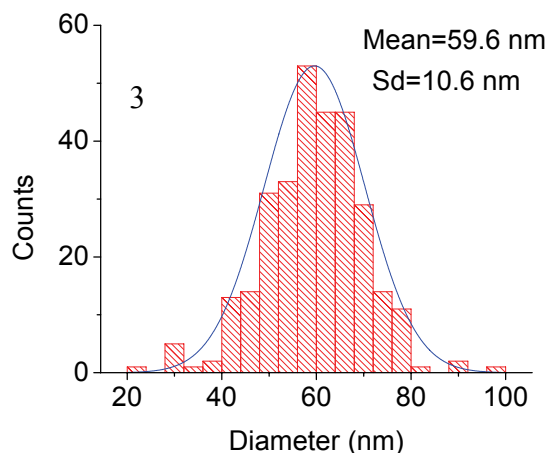
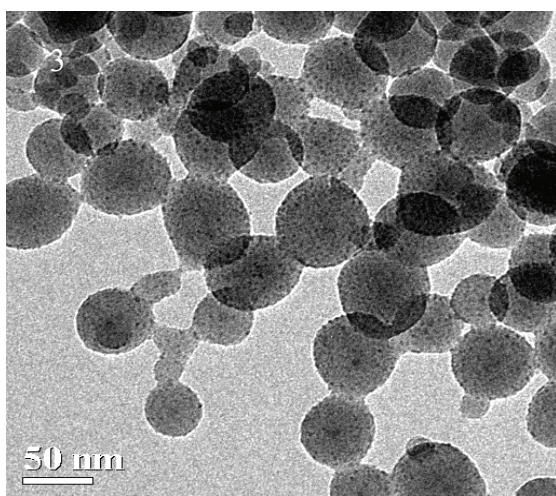
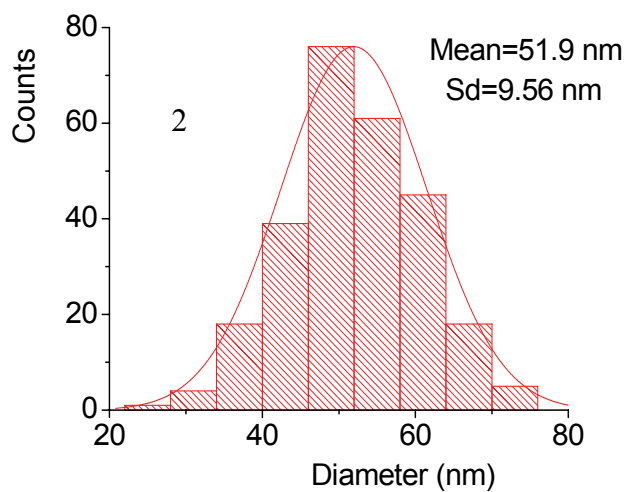
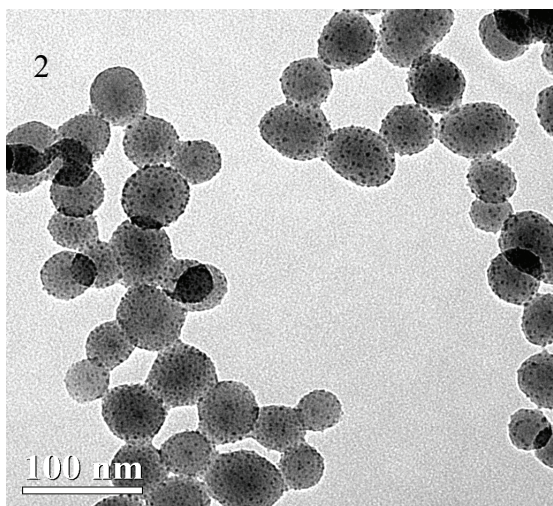
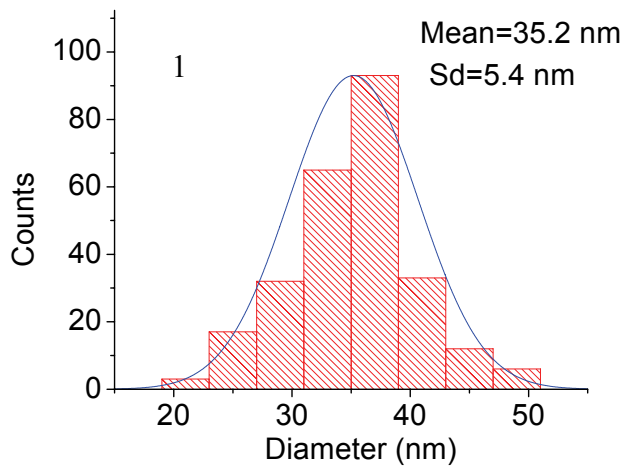
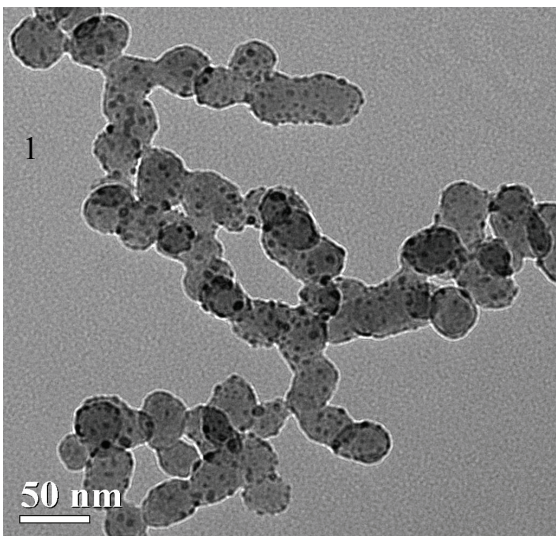


Figure 6.3 TEM images of Silica encapsulated CoPt nanoparticles with TEOS of (1) 0.05 ml, (2) 0.1 ml, (3) 0.2 ml and their size distribution histograms.

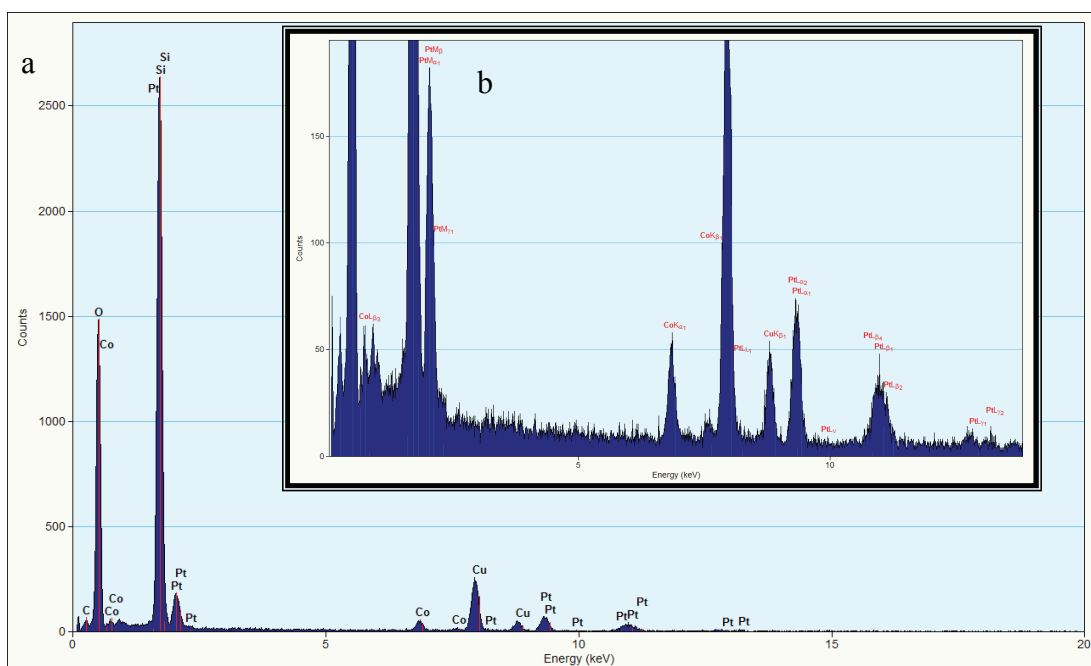


Figure 6.4 EDS of silica encapsulated CoPt nanoparticles. a) Whole EDS spectra, b) Selective region of EDS.

Figure 6.4a shows the EDS of silica encapsulated CoPt nanoparticles. It clearly shows the Si and O signal. Because the percentage of Co and Pt in the sample is very low, their signal is much lower than Si and O. The magnified EDS spectrum of Figure 6.4b clearly shows the Co and Pt signal. The Cu signal comes from TEM copper grids. EDS test clearly confirmed that the sample is composed of Co, Pt, Si and O.

The magnetic properties were studied by AGM at room temperature. It was found that all of the three samples have totally different magnetic properties from the as-made dendrimer mediated CoPt nanoparticles. Figure 6.5 show the hysteresis loops of three silica encapsulated CoPt nanoparticles.

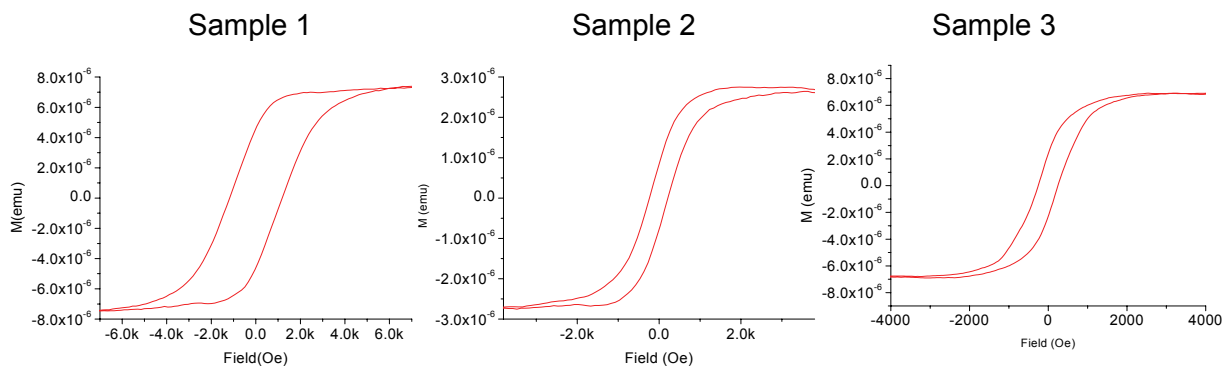


Figure 6.5 Hysteresis loops of three silica encapsulated CoPt nanoparticles.

Table 6.1 Comparison of the size and coercivity of silica encapsulated CoPt nanoparticles

	Sample 1	Sample 2	Sample 3
Hc (Oe)	1198	214	258
Size (nm)	35	52	60
SD (nm)	5.4	9.6	10.6

Table 6.1 summarized the change of coercivity with the changing of the size of silica microspheres. It shows that the coercivity of silica coated CoPt increased a lot compared with the sample without coating. In magnetic nanoparticles system, the coercivity is dependent on anisotropy. For the coated nanoparticles, the magnetic properties are a combination of many anisotropies, which include magnetocrystalline anisotropy, surface anisotropy, and interparticle interactions. In noninteracting particle system, the total magnetic anisotropy (K) are the sum of bulk magnetocrystalline anisotropy (K_{xtal}) and surface anisotropy (K_s), which is expressed by²⁹⁹:

$$K = K_{xtal} + (6/d) K_s$$

d is the diameter of the particles. Upon coating, the surface anisotropy will decrease, thus a decreasing of coercivity should be expected³⁰⁰. But it seems this result is inconsistent with this theory. The assumption of this theory is noninteracting particle system. For this system, the dipolar magnetostatic interactions are big enough not to be neglected. So the magnetostatic dipolar interaction (K_{di}) has to be added to the equation. The total magnetic anisotropy should be revised as:

$$K = K_{\text{xtal}} + (6/d) K_s + K_{di}$$

The contribution of dipolar magnetostatic interactions will make big difference in anisotropy among the samples. Because of the different morphology and size of silica microspheres with different synthesis conditions, the distance between the CoPt nanoparticles and the surface area of the samples will be different, the coercivity was also changed. The similar phenomenon has been found for cobalt ferrite particles in silica matrix and magnetite nanoparticle in silica spheres³⁰¹⁻³⁰³. In those cases, the coercive field was enhanced by the interparticle dipolar interaction which was explained by reflecting the “intrinsic anisotropy” of the particles. Another theory used to explain for the increasing of coercivity of nanocomposite comes from the stronger obstacles when the domains of magnetic nanoparticle try to turn under an applied field. This means that the magnetic nanoparticles are limited and embedded in the matrix and can be considered as pinned³⁰⁴. These results prove that the thickness of silica shell and dispersion of CoPt nanoparticles can significantly influence the coercivity. Thus, the magnetic properties can be simply tuned by silica coating.

6.5 Conclusions

Using PAMAM dendrimer templates, it had been demonstrated that by combining the host/guest properties of dendrimers, new strategies for the synthesis of encapsulated magnetic

alloy nanoparticles into discrete nanosphere composites have been achieved. Dendrimer mediated CoPt multicomponent spheres exhibit multicore-shell structures. The size of the multicore-shell structured spheres can be effectively tuned by the concentration of TEOS. Silica encapsulated CoPt nanoparticles exhibit essential magnetic properties which can be modulated by the synthesis conditions. Such multicomponent microspheres may be used as an important model to study the magnetic properties of multicore-shell system and it may find important applications for the encapsulation and stabilization of magnetic materials, as well as the formation of multi-functional composite systems.

CHAPTER 7 Doubling the Resolution of Discrete Ferromagnetic Nanoparticles Arrays: Capillary Filling in a Magnetic Field

7.1 Synopsis

One prerequisite for future applications of magnetic nanoparticles is their patterning into particular periodic structures within which interparticle distance and magnetic properties of each nanoparticle are well controlled. Here, a scalable technique for controllable two-dimensional assembly of ferromagnetic magnetite nanoparticles beyond the template resolution is presented. Polyethyleneimine was used as a stabilizer to synthesize magnetite nanoparticles. Individual magnetite nanoparticle arrays were fabricated by a capillary filling technique modified by an external magnetic field. In this method, evidently both electrostatic repulsion and anisotropic magnetic dipole-dipole interactions are used to direct magnetite nanoparticle assembly. It is shown that individual magnetic particles were patterned on a silica wafer in paired arrays, doubling the intrinsic resolution of the capillary pattern itself. The technique is technologically feasible and scalable to make ordered magnetic nanoparticles over a large area, which could perhaps be used for ultra-high-density magnetic storage.

7.2 Introduction

In nanotechnology research, a major effort has been devoted to the controlled synthesis and patterning of magnetic nanostructures because of their fascinating properties and unique applications^{69, 305}. The synthesis of magnetic nanoparticles with well-defined nanostructures is the essential first step in the study of nanomagnetism and use in various technologies. Their assembly onto surfaces is a prerequisite for exploiting their properties and applications in

practice. It is a real challenge to pattern magnetic nanoparticles into particular periodic structures within which interparticle distance and magnetic properties of each nanoparticles are well controlled. It is even more difficult for ferromagnetic nanoparticles, since they tend to aggregate due to their magnetic dipole moments. Patterned magnetic nanostructures play an important role in fundamental studies and applications in areas such as ultra high-density storage, nanomagnets, magnetoresistive random access memory (MRAM) and spinelectronic devices^{281, 306}. It is clear that there is a fast growing interest in fabrication of well-defined nanosize magnetic structures^{23, 307}.

It has been shown that evaporation of magnetic nanoparticle solutions under a magnetic field can achieve an ordering of magnetic nanoparticles³⁰⁸. When the applied magnetic field is parallel to the substrate during the evaporation process, the nanocrystals assemble with formation of large linear patterns along the field^{301, 309}. It is clearly seen that the applied field induces the magnetic nanoparticles to form ribbons structures in most studies³¹⁰⁻³¹². In these structures, the spaces between the lines and the positions of the lines are hard to control, and the accurate control of these parameters in assembly is of vital importance to their application. New strategies are required to control the assembly process of magnetic nanoparticles.

A variety of methods have been investigated for patterning of magnetic nanostructures. Direct writing and writing with mask are demonstrated methods for fabrication of highly ordered arrays of magnetic nanoparticles³¹³. Direct writing techniques include electron-beam lithograph, scanning probe nanolithography and laser interference annealing, which are sequential processes³¹⁴⁻³¹⁶. These processes yield precise magnetic patterns, but seem to be highly impractical for mass production because of the lengthy time and expensive equipment required for pattern fabrication. Writing with mask techniques include nanoimprint, electrodeposition and

micromolding technology³¹⁷⁻³¹⁹. Although most of these methods are flexible and effective in producing arrays of magnetic nanoparticles, their accuracy in controlling the spatial arrangement still needs to be demonstrated or improved.

Capillary filling is a promising patterning technique for the formation of continuous features^{320, 321}. In this technique, when an elastomeric stamp with a relief feature is placed on a flat substrate, a network of capillaries is formed at the interface. Suitable solutions are placed at one end of the stamp, and spontaneously fill the open channels by capillary forces. After solvent evaporation, elastomeric stamp is peeled off and a replicated feature is left on the substrate. With the capillary filling technique, well-defined arrays of polymers, hydrogels, liquid crystals, proteins, and inorganic salts have been fabricated³²²⁻³²⁵. The array resolution is limited by the feature size of stamp and it can only form continuous features. It is still a challenge to form controllable individual particle arrays with high resolution.

Here we describe a simple and convenient method that allowed for the large-scale production of highly ordered arrays of magnetite (Fe_3O_4) nanoparticles rapidly and in a controllable fashion. Magnetite is an important example of a half-metallic magnetic material. The key feature of this method is assembly of polyelectrolyte protected magnetic nanoparticles using capillary filling in a magnetic field to control the balance of magnetic dipolar attractive and polyelectrolyte electrostatic repulsive interactions. By this method, two lines of ordered magnetic nanoparticle arrays are formed in each channel. Thus the pattern doubles the resolution of the original stamp. First, capillary filling was used to form a continuous pattern feature. The surfactant polyelectrolyte's electrostatic interactions were used to avoid aggregation of the ferromagnetic nanoparticles. Magnetic forces allowed the magnetic nanoparticles to form an aligned structure. Slow evaporation of solvent resulted in separation of the magnetic

nanoparticles into two lines in each channel. In contrast to other techniques, this method allows formation of individual ferromagnetic nanoparticle arrays with doubled pattern resolution.

7.3 Experimental

7.3.1 Materials

Iron sulfate heptahydrate ($\text{FeSO}_4 \cdot 7\text{H}_2\text{O}$), polyethyleneimine (PEI, $M_w \approx 25\,000\text{ g mol}^{-1}$) were purchased from Aldrich Chemical Company. Potassium nitrate (KNO_3), and potassium hydroxide (KOH) were obtained from Fisher Scientific. All chemicals were used as received without further purification. Millipore quality deionized water (resistivity $>18\text{ M}$) was utilized in experiments.

7.3.2 Preparation of PEI encapsulated Fe_3O_4

PEI encapsulated Fe_3O_4 Synthesis. PEI encapsulated Fe_3O_4 nanoparticles were prepared by a method adapted from the literatures^{326, 327}. A oxidation reaction was used to prepare Fe_3O_4 nanoparticles. In a typical procedure, FeSO_4 , KNO_3 and KOH were dissolved in de-ionized water to make three solutions, with concentrations of 0.06, 2 and 1 mol/L, respectively. These solutions were bubbled with N_2 before use. 10 ml of the potassium hydroxide solution was first mixed with 10 ml potassium nitrate in a beaker. While stirring at a rate of 1000 rpm, this mixture solution was added to 80 ml of iron sulfate solution in a three-neck flask under N_2 protection. The temperature increased to 95 °C, and 0.3g PEI was added to the flask. After one hour of reaction, the mixture was sonicated for one more hour.

Cleaning of PEI encapsulated Fe_3O_4 nanoparticle. Nanoparticles were magnetically separated from solution by placing a magnet below the three-neck flask for 15 min to capture the

particles. Then the upper layer of solution was discarded. The collected Fe_3O_4 nanoparticles were redispersed and rinsed 6 times with deionized water. Finally Fe_3O_4 nanoparticles were suspended in 1 L of deionized water.

7.3.3 Patterning of PEI encapsulated Fe_3O_4 nanoparticles

Figure 7.1 shows the scheme of fabrication. Capillary filling in magnetic field was used in this study to fabricate ordered individual magnetite nanoparticles arrays. A polydimethylsiloxane (PDMS), whose motif consists of parallel grooves across the whole surfaces was placed in contact with a silicon substrate. Microchannels formed between the PDMS stamp and the substrate because of the conformal contact. Drops of Fe_3O_4 nanoparticle solution were deposited at one open end of the PDMS stamp. The solution spontaneously entered the micro-channels because of capillary forces. A magnetic field was applied parallel to the substrate. The solvent evaporated at room temperature in the presence of the magnetic field. After the complete evaporation of the solvent, the PDMS was gently peeled off, leaving the magnetite nanoparticle ordered arrays.

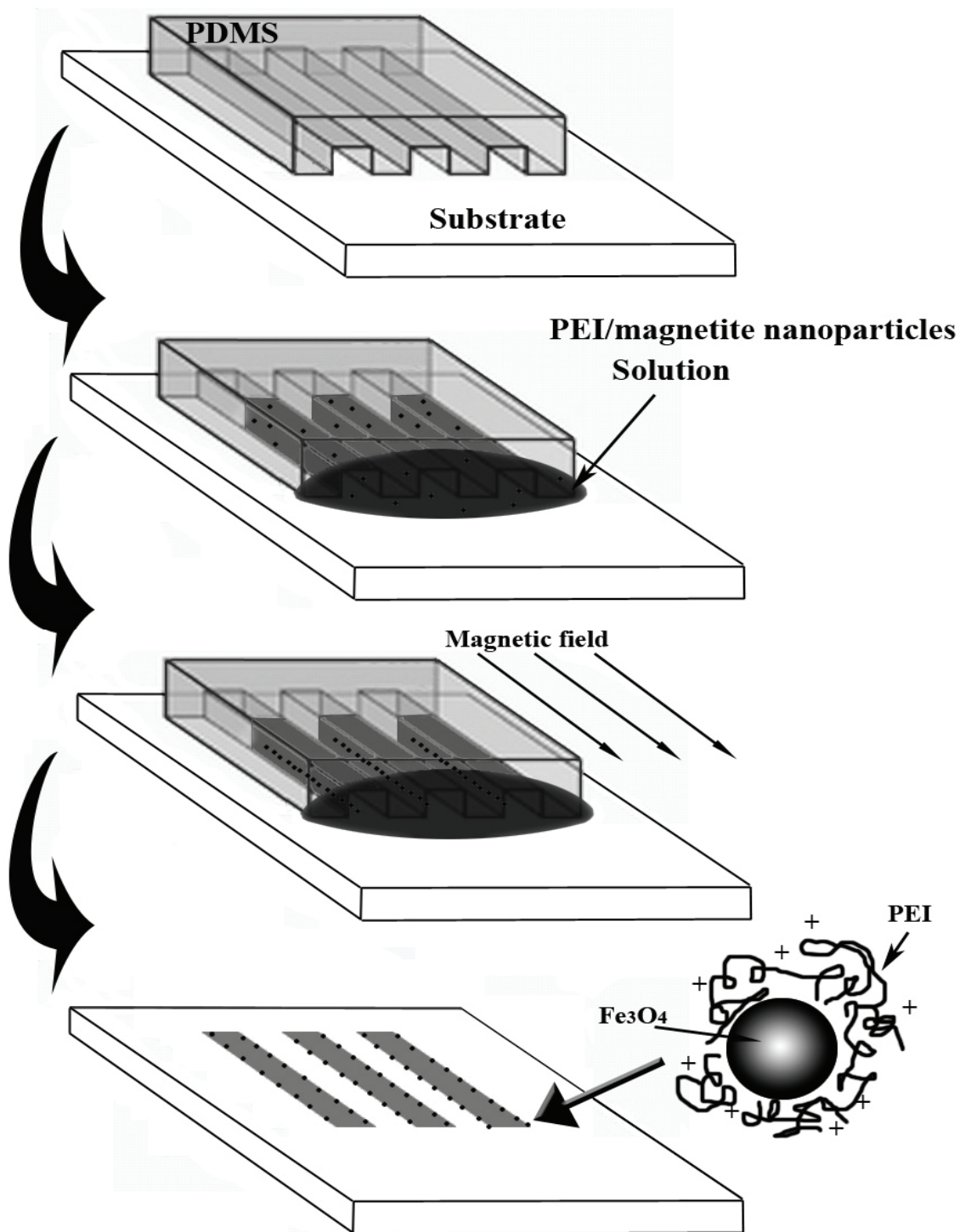


Figure 7.1 Scheme of capillary filling in magnetic field (CFIMF) used to fabricate pattern structures.

7.3.4 Characterization of PEI encapsulated Fe₃O₄ and their pattern.

The Fe₃O₄ nanoparticles morphologies and sizes were analyzed by TEM with a FEI TECNAI F20 microscope. The electron beam acceleration voltage was set at 200kV. TEM samples were prepared by dropping the solution onto a carbon-coated 300 mesh copper TEM grid, followed by air-drying under ambient conditions. Samples for magnetic measurements were obtained by evaporating Fe₃O₄ nanoparticles solution on Si wafers at room temperature. Room temperature magnetic hysteresis curves were measured using a Princeton Micromag 2900 alternating gradient magnetometer (AGM). SEM images were made on a Philips XL30. Energy-dispersive X-ray spectrometry (EDS), was obtained using an EDAX package integrated with the SEM. AFM images were obtained with Nanoscope D-3000 (Digital Instruments, Inc.) The X-ray diffraction pattern was recorded using Philips X'pert-MRD with Cu K_α radiation ($\lambda = 0.15418$ nm).

7.4 Results and discussion

7.4.1 PEI encapsulated Fe₃O₄ nanoparticles

It is believed that the formation of Fe₃O₄ follows a nucleation-growth mechanism³²⁶. Fe²⁺ in the solution is first reacted with OH⁻ to form Fe(OH)₂. Partial oxidation of Fe²⁺ by potassium nitrate to Fe³⁺, then forms Fe(OH)₃. When the molar ratio of Fe(OH)₂ / Fe(OH)₃ is near 1 : 2, which is the characteristic value for magnetite, the nucleation of magnetite particles occurs and the core of Fe₃O₄ begins to grow. In this process, the positively charged PEI can assemble on the surface of the negatively charged Fe₃O₄ nanoparticles and effectively prevent aggregation³²⁷. Figure 7.2a shows the typical transmission electron micrograph of the PEI-coated Fe₃O₄ nanoparticles. It was found that the magnetite nanoparticles are mainly consisted of quadrate

crystallites. Inset is an HRTEM image which apparently shows the PEI around the Fe_3O_4 nanoparticles. Similar HRTEM images of polyelectrolyte coated nanoparticles in other studies confirms the present of polyelectrolyte³²⁷. Figure 7.2 b gives the size distribution histogram of Fe_3O_4 nanoparticles. The average size from statistical analysis of TEM image is 47.9 ± 11.7 nm. Compared with the Fe_3O_4 prepared without PEI³²⁸, it is concluded that the formation of uniform magnetite nanoparticles is attributed to the surfactant properties of the polyelectrolyte. PEI can prevent the coalescence of particles due to the repulsive interaction between the positive charges on the PEI. As shown in Figure 7.2 c, the spotted electron diffraction (ED) pattern with clear and well-defined rings is indicative of the crystalline nature of nanoparticles with uniform crystallite size. The atomic planes indexed in the ED are consistent with those of magnetite.

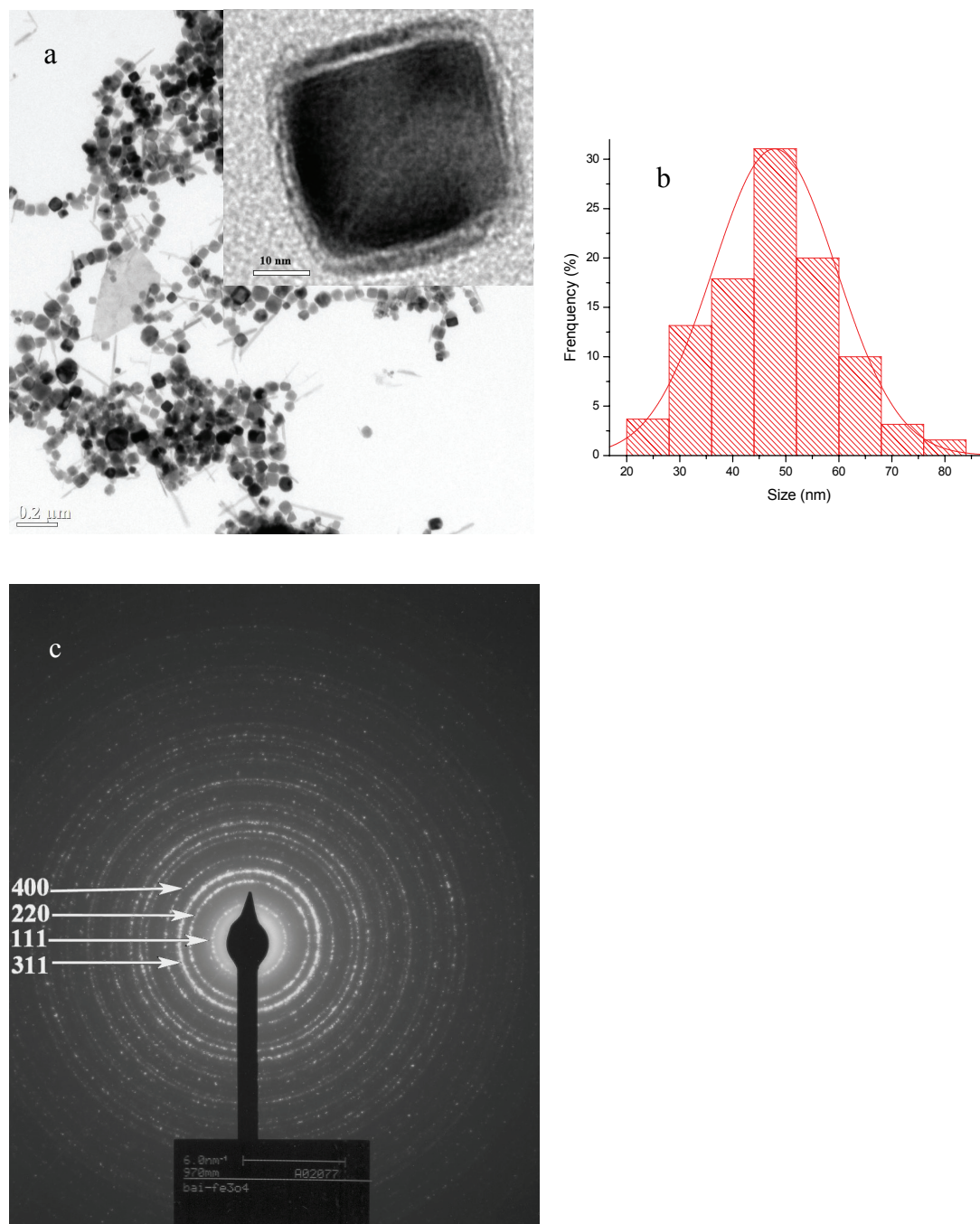


Figure 7.2 a) TEM image of PEI mediated magnetite nanoparticles. Insert shows an HRTEM image of one single PEI mediated magnetite nanoparticle; b) size distribution of magnetite nanoparticles; c) Electron diffraction pattern of magnetite nanoparticles.

The XRD pattern of the sample prepared is shown in Figure 7.3. The insert pattern shows standard magnetite (JCPDS: 19-0629). The position and intensity of the five major peaks match

very well with the standard face-centered cubic (fcc) lattice of Fe_3O_4 . The strong peaks in Figure 7.3 indicate that the sample has good crystallinity state, and no impurity was found in the sample. Scherrer's equation analysis of the full width at half maximum gives the average diameter of the nanoparticles 42.7 nm, in agreement with the TEM result. The good agreement between TEM and x-ray data suggests that Fe_3O_4 nanoparticles are a single crystal.

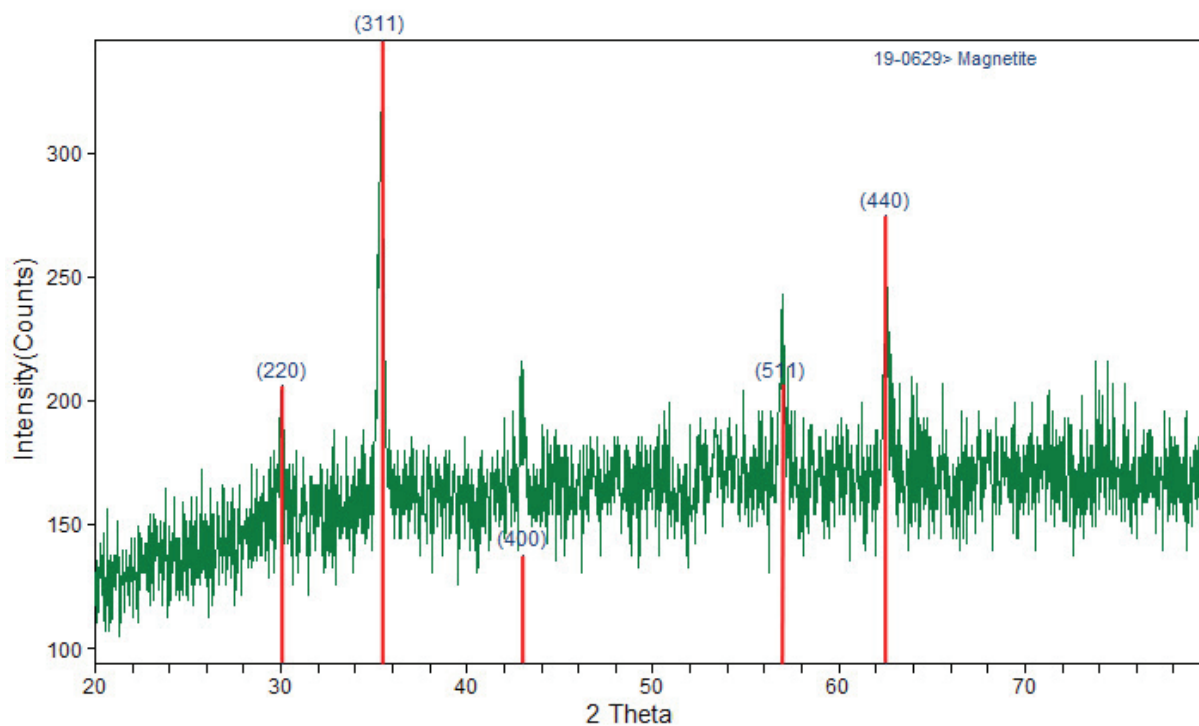


Figure 7.3 XRD pattern of the PEI coated magnetite nanoparticles.

Magnetization curves measured at room temperature are shown in Figure 7.4. The sample has a coercivity of 91 Oe. It is apparently not superparamagnetic because of their size (The switch from ferromagnetic to superparamagnetic behavior for Fe_3O_4 occurs at ~ 13 nm). Although Fe_3O_4 nanoparticles can attract each other via their magnetic dipole moments, the coating of PEI effectively separates them and prevents their aggregation by electrostatic repulsion and steric hindrance. A redispersion experiment demonstrates this. A magnet

attracted and thus aggregated the nanoparticles. After the magnet was removed, the Fe_3O_4 particles remained aggregated; this observation suggested that the Fe_3O_4 particles were ferromagnetic. The Fe_3O_4 particles were resuspended by ultrasonication. This process yielded a uniform suspension of Fe_3O_4 particles that clarified within 10–20 s. This observation confirmed the effectiveness of PEI to prevent aggregation.

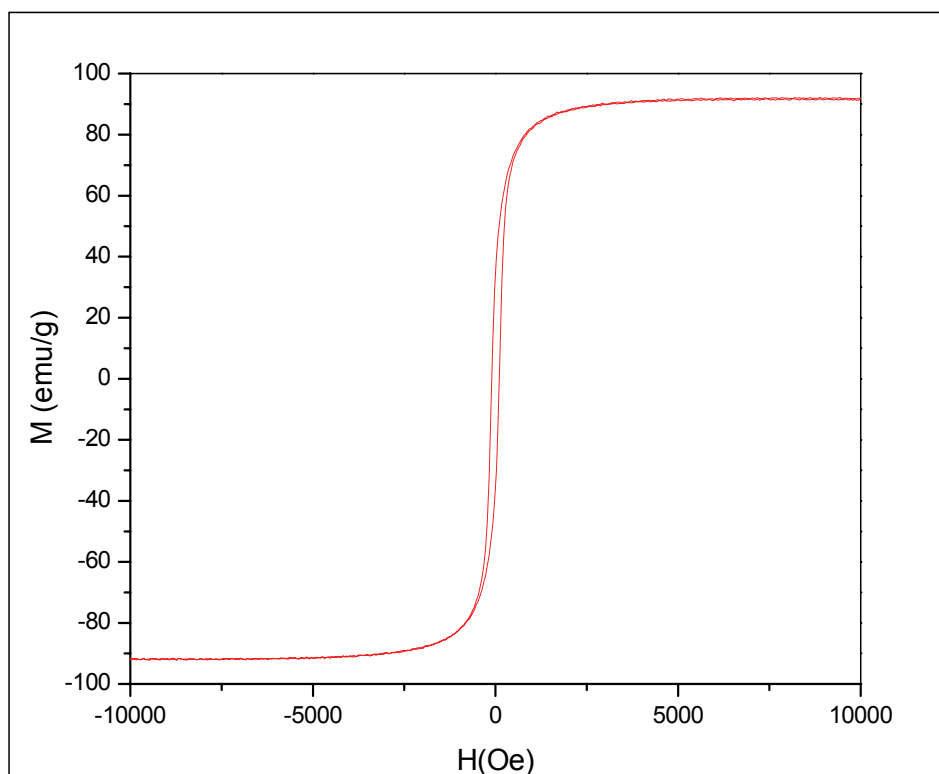


Figure 7.4 AGM magnetometry curves of magnetite nanoparticles.

In order to gain further insight into Fe_3O_4 nanoparticles ordering, SEM was employed and the images are shown in Figure 7.5. It was found that Fe_3O_4 nanoparticles randomly distributed on the substrate with a size about 50 nm. Inset is an EDX spectrum of the sample. Fe_K and O_K can be observed clearly from the inset EDX. Si signal comes from the substrate. In the presence of a magnetic field parallel to substrate but no capillary, evaporation of solvent in magnetite

nanoparticles solution results in assembly of magnetite nanoparticles into linear patterns, (Figure 7.6). The assembly of magnetite nanoparticles involves the coupling of particle's magnetic moment to the applied field which aligns the magnetite nanoparticles along the field. This result indicates that uniaxial magnetic anisotropy predominates and the Zeeman energy is in the same order of magnitude as the thermal energy (K_bT) in the presence of a magnetic field³²⁹. Thus it is enough to align the magnetite nanoparticles. The inset of Figure 7.6 indicates that the line pattern is actually composed of fiber structure with many magnetite wires. It is inferred that in the presence of a magnetic field some of particles will align, generating a local inhomogeneous magnetic field which will align nearby particles with the applied magnetic field, resulting in long ribbon-like structure.

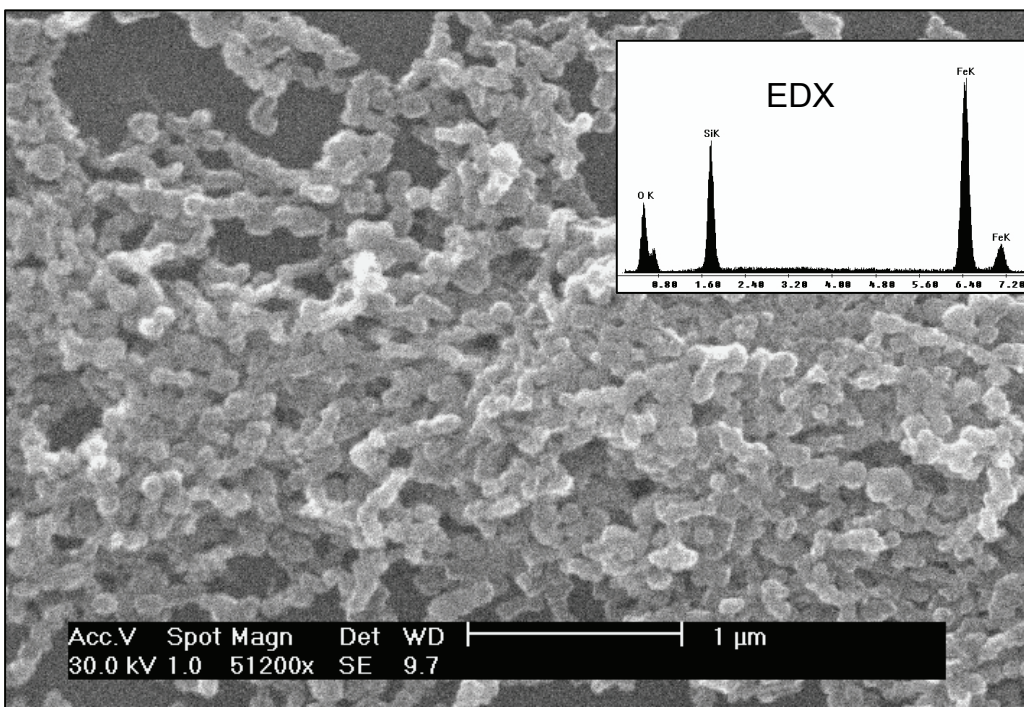


Figure 7.5 SEM image of magnetite nanoparticles. Insert is EDX spectra of the sample.

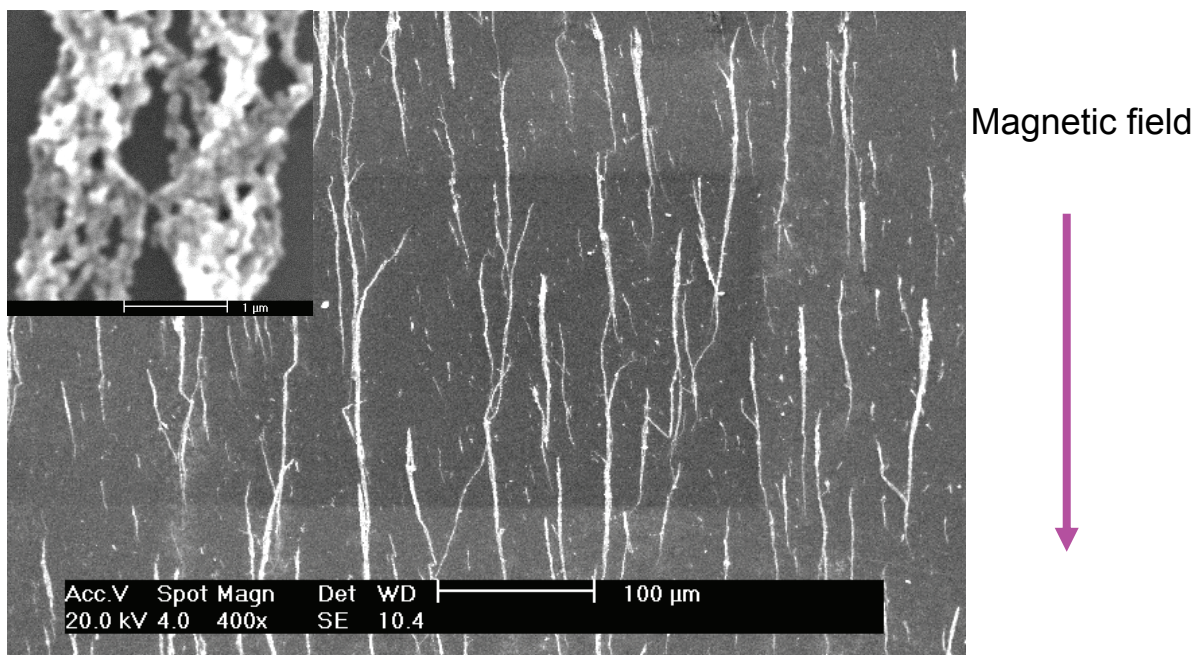


Figure 7.6 SEM image of assembled chain of magnetite nanoparticles. Inset shows magnified chain structure.

7.4.2 Patterning of Fe_3O_4 nanoparticles

Capillary filling (also called micromolding in capillaries-MIMIC) is a soft lithographic technique that allows generation of complex structures of functional materials on both planar and curved surfaces. Here, capillary filling was used to fabricate individual magnetite nanoparticle arrays in a magnetic field. PDMS stamps used in this study were prepared by replica molding of a structured master. Figure 7.7 shows a typical AFM image of the PDMS stamp used in this study. The stamp consists of parallel lines with a periodicity of $5\ \mu\text{m}$. The grooves are $2\ \mu\text{m}$ in width. As shown in Figure 7.1, when the PDMS stamp was brought into conformal contact with a silicon substrate, microcavities formed between them. Then, by capillary forces, drops of magnetite solution were drawn into the channels. Applying a magnetic field parallel to the substrate further align the particles. Subsequent evaporation of solvent induces a small flux of nanoparticles and form two line arrays in each channel. A SEM image of magnetite nanoparticle

arrays is shown in Figure 7.8. The magnetite nanoparticles are well separated and form line structure on the substrate. The arrow in the SEM image is 2 μm in width, which equal to the width of groove in the PDMS stamp. So two lines of magnetite nanoparticles with single-particle resolution forms in one groove. Capillary filling in magnetic field double the pattern resolution of the stamp master.

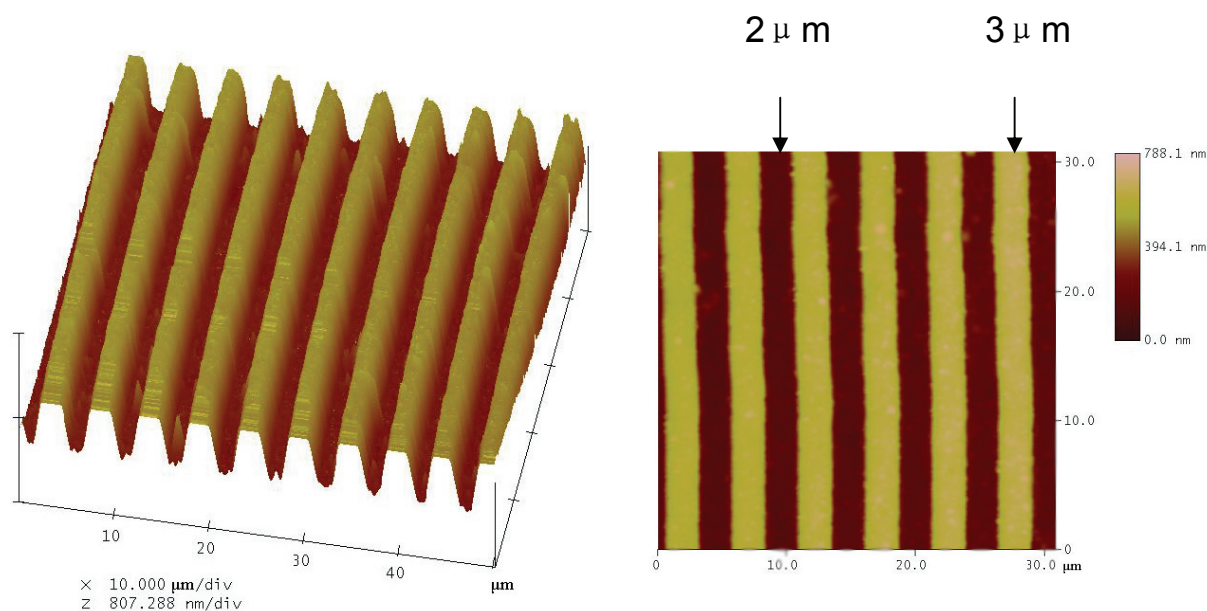


Figure 7. 7 AFM images of the PDMS stamp used in this dissertation.

For convenience, most studies of the assembly of nanoparticles only involve non-magnetic or superparamagnetic nanoparticles which do not possess a dipole in the absence of an applied magnetic field. In this study, ferromagnetic nanoparticles were used. If there is no counter interaction, aggregation will occur, preventing ordered assembly. Thus PEI was coated on magnetite nanoparticles and electrostatic repulsion was used as a counter interaction. The assembly of ferromagnetic nanoparticles is a much more complex process, which involves interaction of the magnetic moment with the applied field, the Van de Waals interactions,

thermal kinetics, capillary forces, electrostatic repulsion, and magnetic dipolar-dipolar interactions³³⁰. A schematic of the process is shown in Figure 7.9. It is well known that the solution enters the channel between the PDMS stamp and the substrate because of capillary forces. Since the magnetite nanoparticles are much smaller than the diameter of the channel, they will enter the channel with the solvent. Due to the thermal motion of the nanoparticles, they will randomly distribute in the channel, as shown in Figure 7.9. When a magnetic field was applied parallel to the channel, the external field aligns the magnetic moment of magnetite particles along the field. It is expected that in the presence of an external magnetic field, the dipole–dipole interaction energy and the thermal energy are two of the dominant factors in the system. The dipole–dipole interaction of particles will overcome the kinetic energy and align the particles with the applied magnetic field, as shown in Figure 7.9 step 1. Long chainlike structures of the magnetic nanoparticles along the direction of the applied magnetic field will form in the channel. This phenomenon is adequately explained by the mechanism that the magnetic moment of the suspended magnetic nanoparticles quickly turns and remains identical to the direction of the applied field³³¹. The PEI polyelectrolyte effectively counteracts the dipole-dipole interaction and prevents aggregation. With the evaporation of solvent (Figure 7.9 step 2), the residual of solution is not enough to fill the channel, and then the solvent tends to accumulate at the boundaries of the channel. This will drag the magnetite nanoparticles to the edges of the channels^{332, 333}. Because the electrostatic repulsion interaction can partially counteract the dipole-dipole interaction, this helped the dragging of magnetite nanoparticle to the corner by solvent evaporation. The dragging of magnetite nanoparticle to both edges cause the formation of two line of ordered magnetite nanoparticle arrays in one channel (Figure 7.9 step 3). The deposited particles are separated by large distances where the electrostatic repulsion interaction between

particles is substantially decreased. In this complicated process, many interactions are apparently at work in forming ordered ferromagnetic nanoparticles arrays with higher pattern resolution: capillary forces draw the particles into the channel; magnetic field help to suppress Brownian motion and the align particles; electrostatic forces help to prevent the aggregation; evaporation of solvent help to separate to two lines.

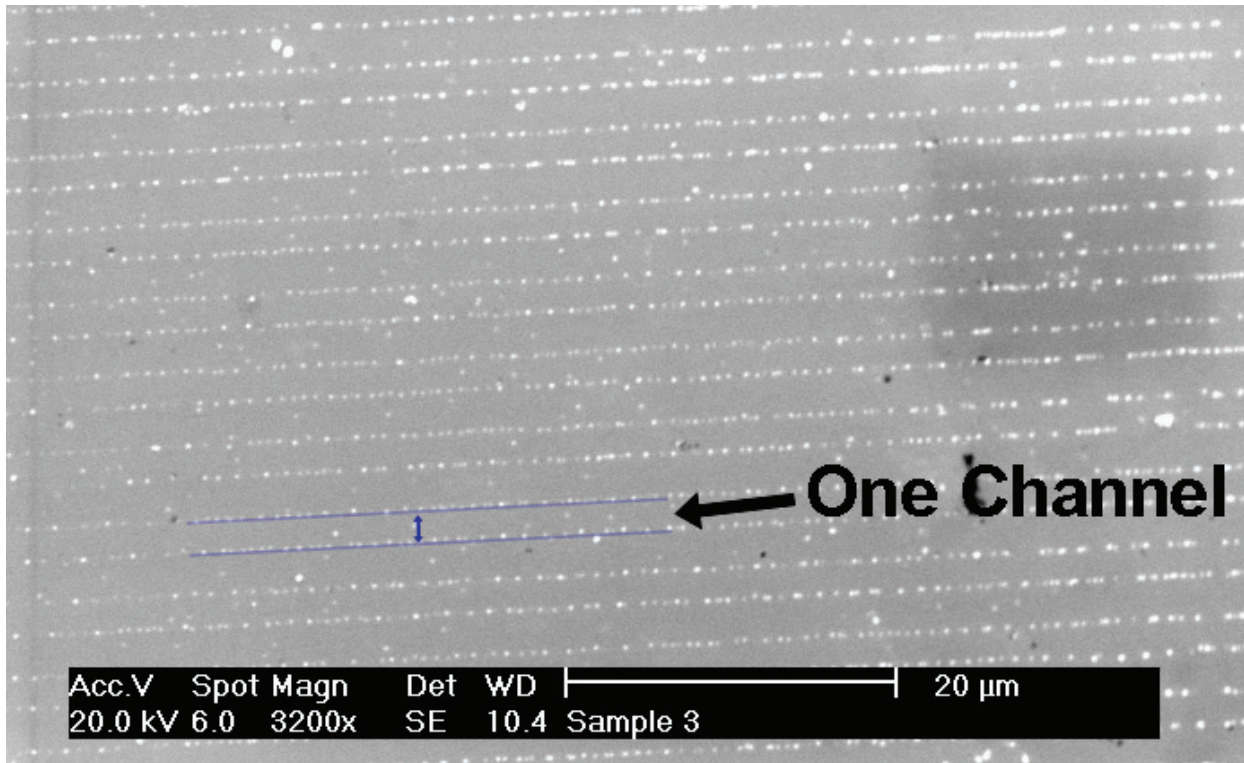


Figure 7. 8 SEM image of magnetite nanoparticles pattern structure.

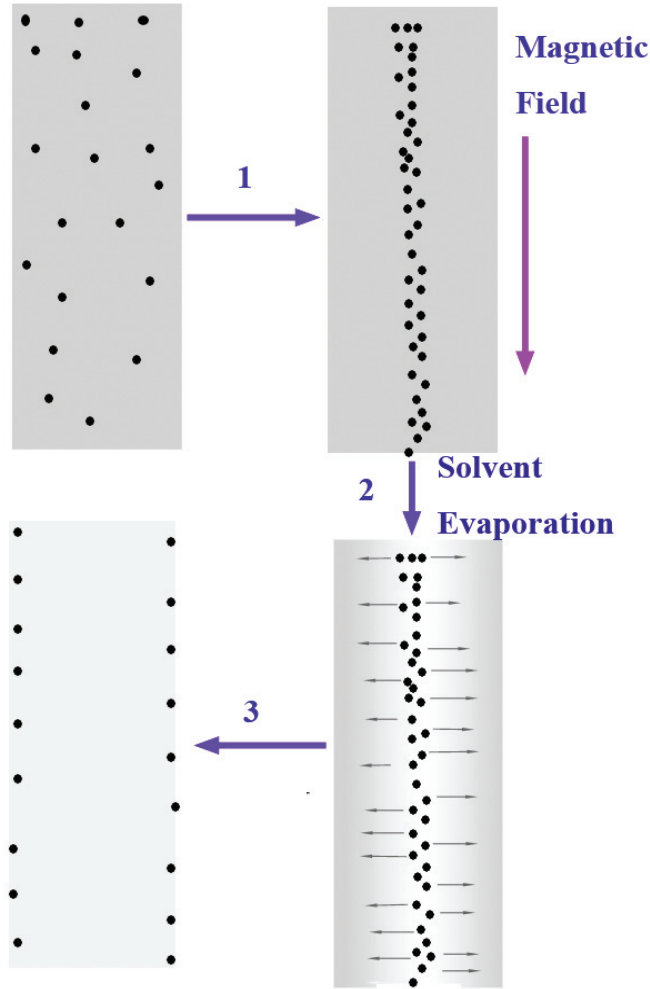


Figure 7.9 Schematic representation of the assembly process of capillary filling in magnetic field.

But is the magnetic field necessary in the assembly process? A complementary experiment was performed to answer this question, keeping all of the conditions the same except without the magnetic field. The experiment procedure is shown in Figure 7.10. SEM was also used to characterize the magnetite nanoparticles arrays, as shown in Figure 7.11. In contrast with assembly in a magnetic field, it can be clearly seen that magnetite nanoparticles randomly distributed in the channel and no double line pattern was seen.

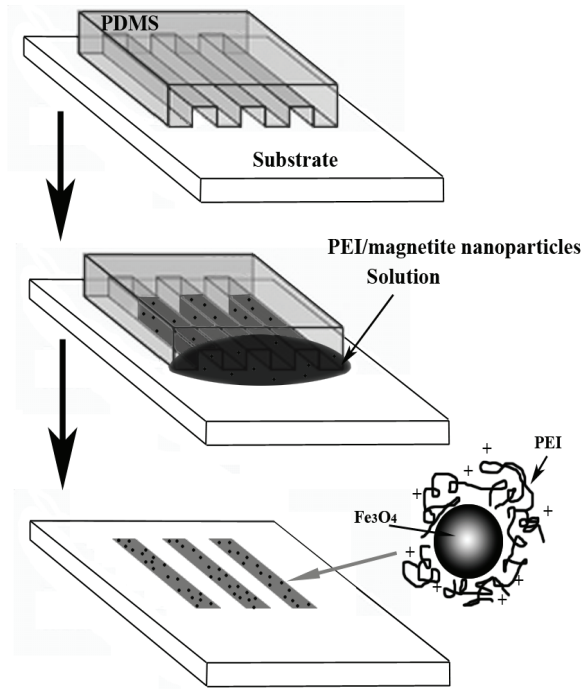


Figure 7.10 Scheme of capillary filling of magnetite nanoparticles without magnetic field.

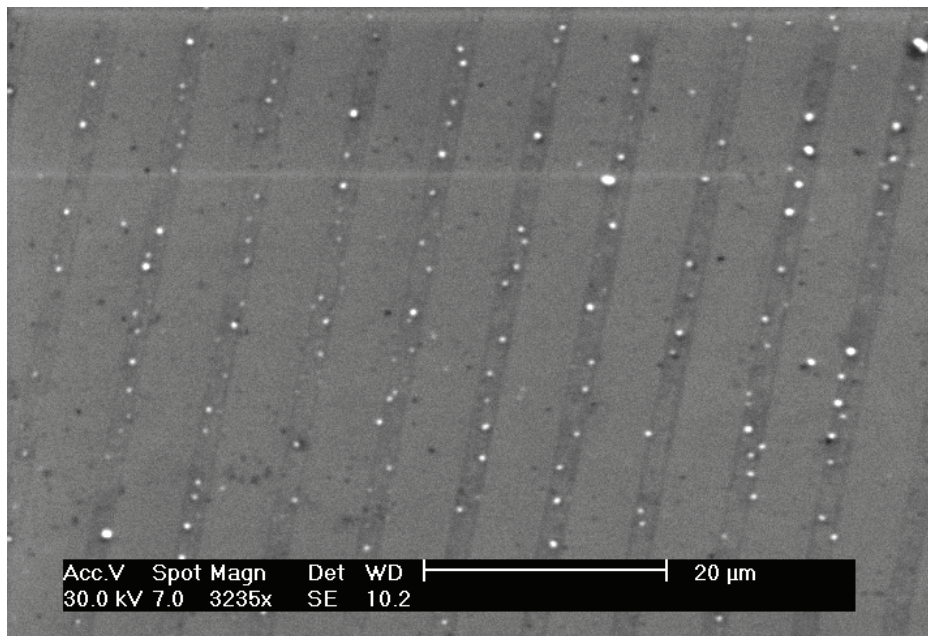


Figure 7.11 SEM image of magnetite nanoparticles arrays by capillary filling without magnetic field.

We believe that the assembly conditions affect the formation of ordered arrays in the channel. If the humidity, temperature, concentration and magnetic field are adjusted, it is apparently possible to form *four* lines in one channel (As shown in Figure 7.12). At present, the exact factors to form better arrays are still under the study.

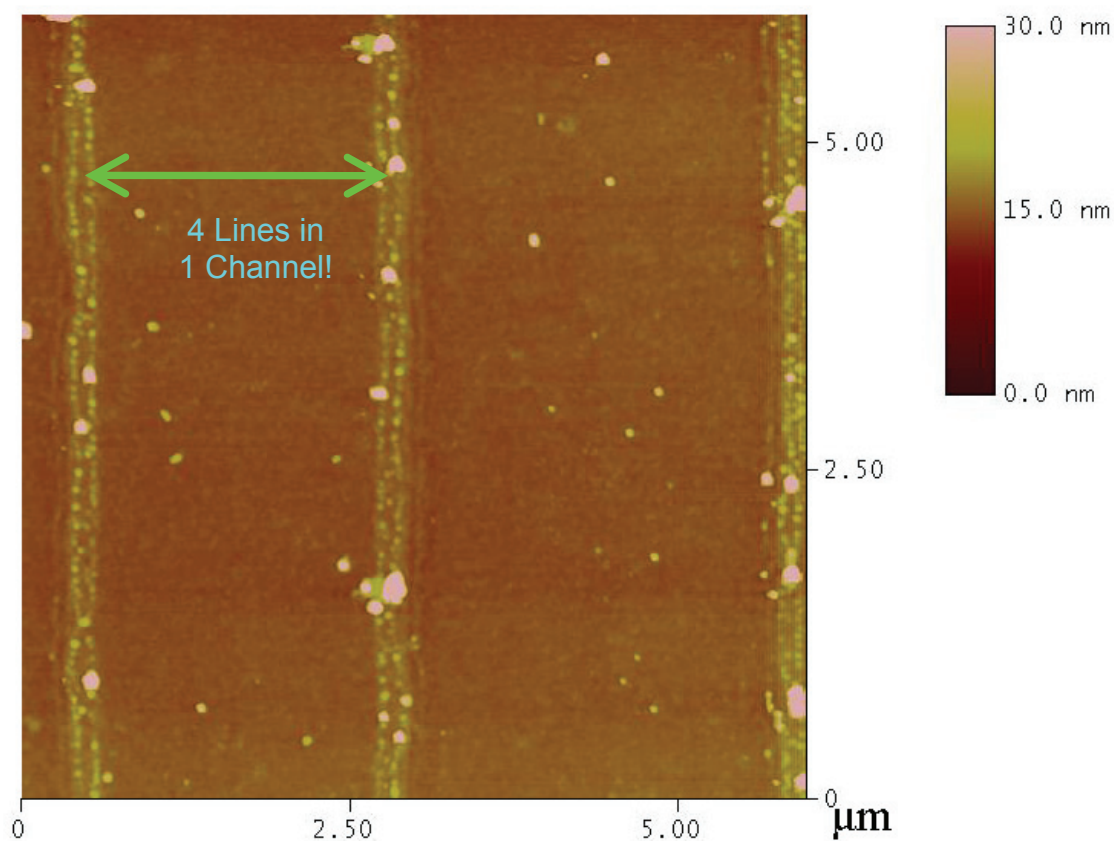


Figure 7.12 AFM images of higher resolution of magnetite nanoparticles array by capillary filling in magnetic field.

7.5 Conclusions

An efficient process was designed to pattern individual magnetic particles in paired arrays, doubling the intrinsic resolution of the template. PEI coated magnetite nanoparticles were synthesized and characterized, then used as assembly materials. It has been shown that the synthesis of magnetite nanoparticles in polyelectrolyte solution can effectively control the growth and aggregation of magnetite nanoparticles. The assembly of magnetite nanoparticles with capillary filling in magnetic field can double the resolution of PDMS template and form ordered magnetite nanoparticles assemblies with single particle resolution. Due to its high resolution, magnetic nanoparticles assembled this way can be efficiently defined within the critical dimension for nanoscale devices. Further doubling the resolution may be possible.

Capillary filling in magnetic field is a well designed method which uses many interactions to direct magnetic nanoparticles assembly. This procedure is very flexible. It is believed that this method can be adapted to other superparamagnetic or ferromagnetic nanoparticles. Extending this method to other systems, capillary filling in magnetic field will allow addressing and manipulation of various magnetic nanoparticles and enable fabrication of magnetic nanoparticle patterns with higher resolution.

CHAPTER 8 Conclusions and Suggestions for Future Research

8.1 Conclusions

Polymer-mediated nanoparticles are versatile and diverse functional materials, with applications ranging from catalysis to nanosize device fabrication. Coating with polyelectrolyte polymers gives them new functionality and properties. The understanding of polymer mediated nanoparticles and how their properties are affected by synthesis is to the application of these nanomaterials in practice. The original objective of this dissertation research was to gain both fundamental and application oriented information about polymer templates, nanoparticles and their interactions. To achieve this goal, two kinds of polymers were used, including PEI and PAMAM dendrimer; various nanoparticles were used, including, Pt, Co_3O_4 , FePt, Fe_3O_4 , CoPt. The synthesis and assembly of these polymer-mediated metal and metal oxide nanoparticles has been investigated.

It has been demonstrated that a photochemical strategy is an effective method to synthesize monodisperse or morphologically controlled nanoparticles. Using a photoreduction method, PEI mediated Pt nanoparticles have been prepared. It has been shown that PEI plays an important role in the preparation of the Pt nanoparticles. Different ratios of the ratio of PEI to Pt result in products with different stability. Testing the catalytic activity of the photoreduced particles by reduction of 4-nitrophenol showed that there is a strong relationship between the the ratio of PEI to Pt and the catalytic activity. PEI mediated Pt nanoparticles also exhibit excellent electrochemical catalytic properties for the methanol oxidation reaction. The results indicate that PEI is a good capping, reducing agent and carrier for the synthesis of nanoparticles, and does not block the active sites on the metal surfaces. PEI assisted photoreduction synthesis appears to be a

promising method for the preparation of well-dispersed Pt nanoparticles, and this method provides an attractive route to Pt catalysts with good catalytic activity and reliable catalytic performance.

A photochemical method was also successfully used to synthesize PEI-mediated Co_3O_4 nanoparticles at room temperature and ambient pressure. High quality rod-shape Co_3O_4 nanocrystals were synthesized. This approach is not simply the photoreduction of precursor metal ions to zerovalent metal but rather a photo-driven process from a complexed intermediate. PEI was used as a stabilizer in this reaction. It has been shown that the morphology of Co_3O_4 nanorods is dependent on the molar ratio of PEI to precursor Co^{2+} . PEI proved to be a good template leading to the growth of nanocrystals to nanorods.

Chemical methods are also effective ways to synthesize polymer mediated nanoparticles. In this work, FePt and CoPt nanoparticles were prepared by a chemical reduction method with dendrimer template. Both as-prepared alloy nanoparticles are chemically disordered with the fcc phase. Thermal annealing induces a change in particle structure from chemically disordered fcc to chemically ordered fct and transforms alloy nanoparticles from superparamagnetic to ferromagnetic. By combining the host/guest properties of dendrimers, CoPt nanoparticles were encapsulated in silica microspheres. Dendrimer mediated CoPt multicomponent spheres exhibit multicore-shell structures. Silica encapsulated CoPt nanoparticles exhibit magnetic properties which can be modulated by the synthesis conditions. These results indicate that dendrimer can be used as template to synthesize magnetic alloy nanoparticles and allow encapsulating by other materials.

Formation of morphologically controlled and highly ordered arrays of nanoparticles is prerequisite to exploit nanoparticle properties for device fabrication. A new way to generate

patterned magnetic nanoparticles was developed as described in the end of the dissertation. Individual magnetite nanoparticle arrays were fabricated by a capillary filling technique modified by an external magnetic field. In this method, evidently both electrostatic repulsion and anisotropic magnetic dipole-dipole interactions are used to direct magnetite nanoparticle assembly. It is shown that individual magnetic particles were patterned on a silica wafer in paired arrays, doubling the intrinsic resolution of the capillary pattern itself. It is a feasible and scalable technique to make ordered magnetic nanoparticles over a large area, which could perhaps be used for ultra-high-density magnetic storage.

By the above examples, polymers (PEI, dendrimer) were demonstrated to be valuable materials in nanoscience. First, polymers can be used as templates for the preparation of nanomaterials, such as, nanoparticles and nanorods. PEI and PAMAM dendrimer are commercially available and size controllable with various molecular weights. It is very convenient to control the size of nanoparticles. Second, dendrimer and PEI mediated nanoparticles are very stable and dispersible in water because of hydrophilicity of these polymers. Third, the catalytic activity of nanoparticles is not deteriorated by coated of polyelectrolyte PEI. Fourth, coating with polyelectrolytes give the nanoparticles new functionalities and they can be assembled by various methods without aggregation. Thus, the strategies developed in this work take advantage of polymers and nanoparticles. These strategies can be further developed to 1) use these kinds of materials for technological applications and fundamental research; and 2) invent new functional materials in catalysis, biotechnology, medicine, electronics, and photonics.

8.2 Suggestions for Future Research

8.2.1 Pt coated magnetite nanoparticles

In the Chapter 7, it was shown that PEI mediated magnetite nanoparticles can be synthesized by a simple chemical method. In Chapter 2, Pt nanoparticles were synthesized by a photoreduction method. Can we combine these two processes together? Can Pt nanoparticles be synthesized at the surface of magnetite nanoparticle? If this combination works, Pt coated magnetite complex structure will be fabricated. Because of the magnetic properties of magnetite and catalytic properties of Pt, these kinds of complex Pt/magnetite nanostructure will be a kind of catalyst that can be easily recovered. After the catalytic reaction, the catalyst can be separated by a magnetic field. Some efforts have been spent on this direction. Figure 8.1 shows the TEM image of Pt/magnetite nanostructure. The catalytic activity needs to be evaluated in the future to prove the assumptions above.

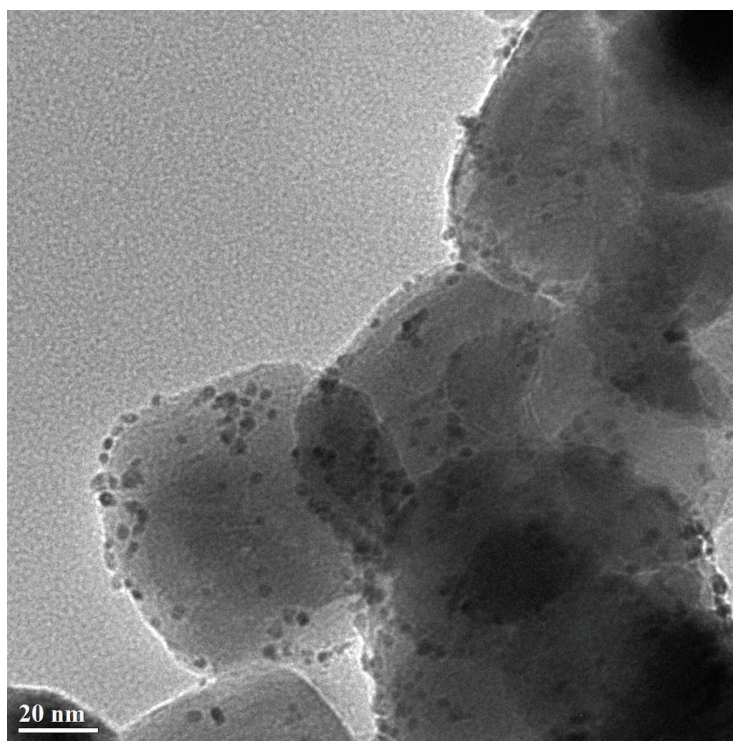


Figure 8.1 TEM image of Pt/magnetite nanoparticles.

8.2.2 Oxygen reduction reaction (ORR) of PEI mediated Pt nanoparticles

The electrocatalytic reduction of oxygen to water is especially important for fuel cells, batteries, and many other electrode applications^{334, 335}. Pure Pt and Pt alloys have been extensively studied, and show high catalytic activity toward ORR³³⁶⁻³³⁸. Reduction of oxygen at low overpotential is the main goal of studies aimed at the development of efficient cathodes for fuel cells. PEI mediated Pt show excellent catalytic activity for methanol reduction reaction, as shown in chapter 3. PEI mediated Pt nanoparticles may also exhibit catalytic activity toward oxygen reduction reaction. In the future, electrocatalytic reduction of oxygen by PEI mediated Pt nanoparticles should to be investigated.

8.2.3 PEI mediated Ru nanoparticles

Ru is very useful for the methanol reduction and oxygen reduction reactions. The synthesis of Ru nanoparticles have attracted much attraction^{339, 340}. PEI was used as a stabilizer to synthesize Ru nanoparticles in aqueous solution by photoreduction. Figure 8.2 (a) and (b) show preliminary TEM and EDX data of Ru nanoparticles which was irradiated for 24 h. It has been shown that the Ru are spherical particles with average size of about 4 nm. Ru nanoparticles have not yet been evaluated for their catalytic activity and stability.

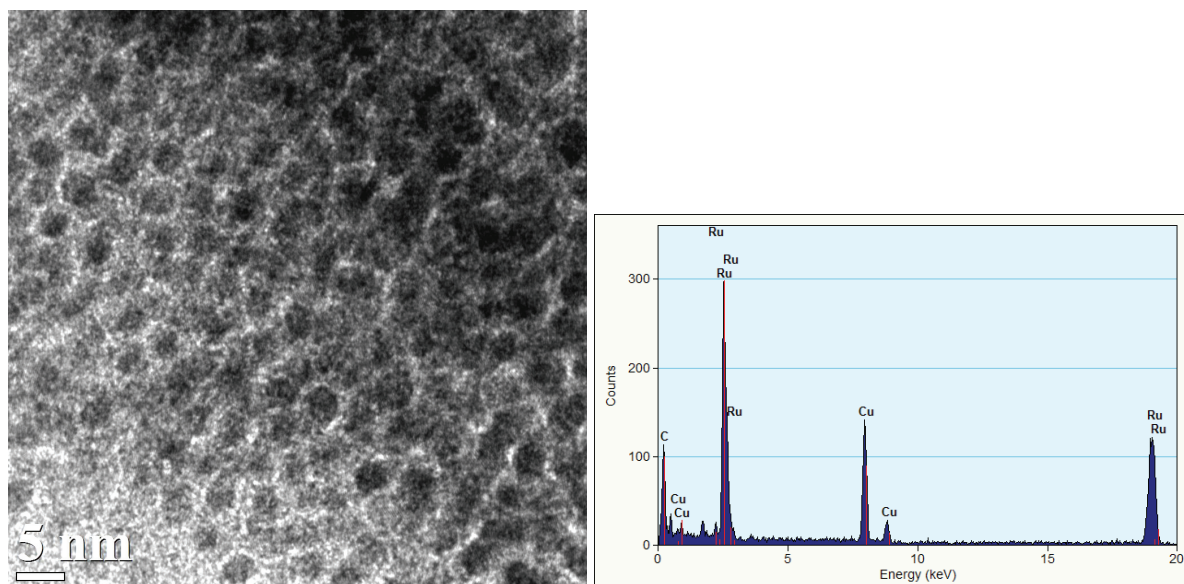


Figure 8.2 a) TEM image of Ru nanoparticles; b) EDX of as-made PEI mediated Ru nanoparticles.

8.2.4 PEI mediated magnetic alloy nanoparticles

PEI and PAMAM are chemically and physically similar polymers. Their shape, molecular weight, and functional groups are all similar. The difference between them is that PEI is not monodisperse as dendrimer. So it is possible to use PEI as template to synthesize magnetic alloy nanoparticles like just with the dendrimer. The dendrimer template is monodisperse, and we find that the particles made by dendrimer have some size distribution. In the future, techniques need to be used to control the molecular weight and shape of PEI, or some strategies need to be designed to quickly narrow the size distribution of PEI. With the monodisperse PEI, the size distribution of metal nanoparticles is expected to be improved.

8.2.5 Enhanced coercivity by silica sphere encapsulation

In chapter 6, it has been shown that silica encapsulated CoPt nanoparticles exhibit improved magnetic properties which can be modulated by the synthesis conditions. There are

still several theories to explain this phenomenon. One of them stated that the dipole-dipole moment was changed by the silica coating, which separates the particles from each other. Hutlova³⁰³ pointed out that the increase of coercivity of the magnetic nanoparticles with silica coating reflects the “intrinsic anisotropy”. Another explanation of the increase of the coercivity of the nanocomposite comes from the higher barrier when the domains of magnetic nanoparticles try to turn under an applied field³⁰². Further work needs to be done to prove these theories.

8.2.6 Study of PEI oxidation mechanism

The results in this dissertation indicate that PEI can be used as a capping and reducing agent and as a carrier in the synthesis of nanoparticles. Preliminary FT-IR results show that primary amine groups disappeared after UV irradiation. But the exact oxidation mechanism needs to be carefully studied to extend PEI capping and reducing agent to other particle preparations.

8.2.7 Patterned structures of magnetic nanoparticles

It has been demonstrated in chapter 7 that capillary filling in magnetic field is an effective way to improve the resolution of magnetic nanoparticles patterned structures. The temperature, humidity, pressure, strength of magnetic field will strongly affect the order and density of the pattern. Experiments are suggested to study how these parameters affect the arrays. This work should also be extended to other magnetic nanoparticles, which include silica multicomponent magnetic microspheres.

REFERENCES

1. Meyer, G.; Neu, B.; Rieder, K. H., *Physica Status Solidi B-Basic Research* **1995**, *192* (2), 313-324.
2. Meyer, G.; Rieder, K. H., *Surface Science* **1997**, *377* (1-3), 1087-1093.
3. Neu, B.; Meyer, G.; Rieder, K. H., *Modern Physics Letters B* **1995**, *9* (15), 963-969.
4. Eigler, D. M.; Schweizer, E. K., *Nature* **1990**, *344* (6266), 524-526.
5. Wang, Z. L., *Characterization of nanophase materials*. 1st ed.; Wiley-VCH: Weinheim ; New York, 2000; p 406.
6. Wolf, E. L., *Nanophysics and nanotechnology : an introduction to modern concepts in nanoscience*. 2nd updated and enl. ed.; Wiley-VCH: Weinheim, 2006; p 292.
7. Hornyak, G. L., *Introduction to nanoscience*. CRC Press: Boca Raton, 2008; p 815.
8. Edelstein, A. S.; Cammarata, R. C., *Nanomaterials : synthesis, properties, and applications*. Institute of Physics Pub.: Bristol ; Philadelphia, 1996; p 596.
9. Cao, G., *Nanostructures & nanomaterials : synthesis, properties & applications*. Imperial College Press: London, 2004; p 433.
10. Rao, C. N. R.; Ramachandra, C. N.; Müller, A.; Cheetham, A. K., *The Chemistry of Nanomaterials: Synthesis, Properties and Applications*. Wiley-VCH ;John Wiley: Weinheim, Chichester, 2004; p 761.
11. Shatkin, J. A., *Nanotechnology : health and environmental risks*. CRC Press/Taylor & Francis Group: Boca Raton, 2008; p 167.
12. Wang, J. X.; Zhou, G. Q.; Chen, C. Y.; Yu, H. W.; Wang, T. C.; Ma, Y. M.; Jia, G.; Gao, Y. X.; Li, B.; Sun, J.; Li, Y. F.; Jiao, F.; Zhao, Y. L.; Chai, Z. F., *Toxicology Letters* **2007**, *168* (2), 176-185.
13. Skomski, R.; NetLibrary Inc., *Simple models of magnetism*. Oxford University Press: Oxford ; New York, 2008; p 349.
14. Hall, S.; Nazarov, A. N.; Lysenko, V. S., *Nanoscaled semiconductor-on-insulator structures and devices*. Springer: Dordrecht, 2007; p 369.
15. Nalwa, H. S., *Nanostructured materials and nanotechnology*. Concise ed.; Academic Press: San Diego, 2001; p 834.
16. Baraton, M.-I., *Synthesis, functionalization and surface treatment of nanoparticles*. American Scientific Publishers: Stevenson Ranch, Calif., 2003; p 302.

17. Koch, C. C., *Nanostructured materials : processing, properties, and potential applications*. Noyes Publications/William Andrew Pub.: Norwich, N.Y., 2002; p 612.
18. Ozin, G. A.; Arsenault, A. C.; Royal Society of Chemistry (Great Britain), *Nanochemistry : a chemical approach to nanomaterials*. Royal Society of Chemistry: Cambridge, UK, 2005; p 628.
19. Nutzenadel, C.; Zuttell, A.; Chartouni, D.; Schmid, G.; Schlapbach, L., *European Physical Journal D* **2000**, 8 (2), 245-250.
20. Vollath, D., *Nanomaterials : an introduction to synthesis, properties and application*. Wiley-VCH: Weinheim, 2008; p 352.
21. Edelstein, A. S.; Cammarata, R. C.; NetLibrary Inc., *Nanomaterials synthesis, properties, and applications*. Pbk. ed.; Institute of Physics Pub.: Bristol ; Philadelphia, 1998; p 596.
22. Astruc, D., *Nanoparticles and catalysis*. Wiley-VCH: Weinheim, 2008; p 640.
23. Somasundaran, P., *Encyclopedia of surface and colloid science*. 2nd ed.; Taylor & Francis: Boca Raton, 2006; p 6675.
24. Atwood, J. L.; Steed, J. W., *Encyclopedia of supramolecular chemistry*. M. Dekker: New York, 2004; p 1670.
25. Alaa S Abd-El-Aziz, C. E. C. J., Charles U Pittman Jr, *Macromolecules containing metal and metal-like elements*. J. Wiley & Sons: Hoboken, NJ, 2003; p 198.
26. Mayya, K. S.; Schoeler, B.; Caruso, F., *Advanced Functional Materials* **2003**, 13 (3), 183-188.
27. Mayer, A. B. R., *Polymers for Advanced Technologies* **2001**, 12 (1-2), 96-106.
28. Scalzullo, S.; Mondal, K.; Witcomb, M.; Deshmukh, A.; Scurrall, M.; Mallick, K., *Nanotechnology* **2008**, 19 (7), 1-8.
29. Li, J. Y.; Li, L.; Xu, J. P.; Zhang, X. S.; Li, H. Y.; Zhuang, J. Y., *Science in China Series E-Technological Sciences* **2009**, 52 (4), 888-892.
30. Kohler, J. U.; Bradley, J. S., *Langmuir* **1998**, 14 (10), 2730-2735.
31. Rotello, V. M., *Nanoparticles : building blocks for nanotechnology*. Kluwer Academic/Plenum Publishers: New York, 2004; p 284.
32. Boal, A. K.; Frankamp, B. L.; Uzun, O.; Tuominen, M. T.; Rotello, V. M., *Chemistry of Materials* **2004**, 16 (17), 3252-3256.
33. Sun, S. H.; Anders, S.; Hamann, H. F.; Thiele, J. U.; Baglin, J. E. E.; Thomson, T.; Fullerton, E. E.; Murray, C. B.; Terris, B. D., *Journal of the American Chemical Society* **2002**, 124 (12), 2884-2885.

34. Bhattacharya, S. N.; Kamal, M. R.; Gupta, R. K., *Polymeric nanocomposites : theory and practice*. Carl Hanser Publishers ; Hanser Gardner Publications: Munich Cincinnati, Ohio, 2008; p 383.
35. Lombardi, S. L., *Nanoparticles : new research*. Nova Science Publishers: New York, 2008; p 412.
36. Dykes, G. M., *Journal of Chemical Technology and Biotechnology* **2001**, 76 (9), 903-918.
37. Fréchet, J. M. J.; Tomalia, D. A., *Dendrimers and other dendritic polymers*. Wiley: Chichester ; New York, 2001; p 647.
38. Newkome, G. R.; Shreiner, C. D., *Polymer* **2008**, 49 (1), 1-173.
39. Boas, U.; Heegaard, P. M. H., *Chemical Society Reviews* **2004**, 33 (1), 43-63.
40. Fritz Vögtle, C. A. S., Hak-Fun Chow, *Dendrimers III: design, dimension, function*. Springer: 2001; p 97-110.
41. Maiti, P. K.; Goddard, W. A., *Journal of Physical Chemistry B* **2006**, 110 (51), 25628-25632.
42. Unal, B.; Hedden, R. C., *Polymer* **2009**, 50 (3), 905-912.
43. Maiti, P. K.; Cagin, T.; Lin, S. T.; Goddard, W. A., *Macromolecules* **2005**, 38 (3), 979-991.
44. Fritz Vögtle, M. B.; Tomalia, D. A., *Dendrimers and other dendritic polymers*. **2001**, p 647.
45. Feldheim, D. L.; Foss, C. A., *Metal nanoparticles : synthesis, characterization, and applications*. Marcel Dekker: New York, 2002; p 338.
46. Zhao, M. Q.; Sun, L.; Crooks, R. M., *Journal of the American Chemical Society* **1998**, 120 (19), 4877-4878.
47. Balogh, L.; Tomalia, D. A., *Journal of the American Chemical Society* **1998**, 120 (29), 7355-7356.
48. Esumi, K.; Suzuki, A.; Yamahira, A.; Torigoe, K., *Langmuir* **2000**, 16 (6), 2604-2608.
49. Esumi, K.; Hosoya, T.; Suzuki, A.; Torigoe, K., *Journal of Colloid and Interface Science* **2000**, 226 (2), 346-352.
50. Esumi, K.; Suzuki, A.; Aihara, N.; Usui, K.; Torigoe, K., *Langmuir* **1998**, 14 (12), 3157-3159.
51. Esumi, K., *Colloid Chemistry Ii* **2003**, 227, 31-52.

52. Grohn, F.; Bauer, B. J.; Akpalu, Y. A.; Jackson, C. L.; Amis, E. J., *Macromolecules* **2000**, *33* (16), 6042-6050.
53. Crooks, R. M.; Zhao, M. Q.; Sun, L.; Chechik, V.; Yeung, L. K., *Accounts of Chemical Research* **2001**, *34* (3), 181-190.
54. Zhao, M. Q.; Crooks, R. M., *Angewandte Chemie-International Edition* **1999**, *38* (3), 364-366.
55. Zhao, M. Q.; Crooks, R. M., *Advanced Materials* **1999**, *11* (3), 217-220.
56. Peng, X. H.; Pan, Q. M.; Rempel, G. L., *Chemical Society Reviews* **2008**, *37* (8), 1619-1628.
57. Knecht, M. R.; Weir, M. G.; Frenkel, A. I.; Crooks, R. M., *Chemistry of Materials* **2008**, *20* (3), 1019-1028.
58. Niu, Y. H.; Yeung, L. K.; Crooks, R. M., *Journal of the American Chemical Society* **2001**, *123* (28), 6840-6846.
59. Meszaros, R.; Thompson, L.; Bos, M.; de Groot, P., *Langmuir* **2002**, *18* (16), 6164-6169.
60. Dietrich Braun, H. C., Helmut Ritter, *Polymer Synthesis: Theory and Practice: Fundamentals, Methods, Experiments*. 2001.
61. Cho, K. C.; Choi, S. H.; Park, T. G., *Macromolecular Research* **2006**, *14* (3), 348-353.
62. Salamone, J. C., *Polymeric materials encyclopedia*. CD-ROM ed.; CRC Press,: Boca Raton, 1996.
63. Sun, X. P.; Dong, S. J.; Wang, E. K., *Polymer* **2004**, *45* (7), 2181-2184.
64. Tan, S.; Erol, M.; Attygalle, A.; Du, H.; Sukhishvili, S., *Langmuir* **2007**, *23* (19), 9836-9843.
65. Wang, Z. Y.; Liu, G.; Sun, J.; Wu, B. Y.; Gong, Q. Y.; Song, B.; Ai, H.; Gu, Z. W., *Journal of Nanoscience and Nanotechnology* **2009**, *9* (1), 378-385.
66. Hong, H.; Davidov, D.; Kallinger, C.; Lemmer, U.; Feldmann, J.; Harth, E.; Gugel, A.; Mullen, K., *Synthetic Metals* **1999**, *102* (1-3), 1487-1487.
67. Ganesan, P. G.; Wang, X.; Nalamasu, O., *Applied Physics Letters* **2006**, *89* (21), 3107.
68. Rodríguez, J. A.; Fernández Garcia, M., *Synthesis, properties, and applications of oxide nanomaterials*. Wiley-Interscience: Hoboken, N.J., 2007; p 717.
69. Sellmyer, D. J.; Skomski, R., *Advanced magnetic nanostructures*. Springer: New York, 2006; p 507.

70. Franke, M. E.; Koplin, T. J.; Simon, U., *Small* **2006**, 2 (1), 36-50.
71. Oskam, G., *Journal of Sol-Gel Science and Technology* **2006**, 37 (3), 161-164.
72. Rodríguez, J. A.; Fernández Garcia, M., *Synthesis, properties, and applications of oxide nanomaterials*. Wiley-Interscience: Hoboken, N.J., 2007; p 717.
73. Sergeev, G. B., *Nanochemistry*. Elsevier: Amsterdam ; London, 2006; p 249.
74. Challa S. S. R. Kumar, C. S. S. R. K., *Metallic Nanomaterials*. 2009.
75. Dragieva, I.; Ivanova, G.; Bliznakov, S.; Lefterova, E.; Stoynov, Z.; Markova, I.; Pankova, M., *Physics and Chemistry of Glasses* **2000**, 41 (5), 264-266.
76. Male, K. B.; Li, J. J.; Bun, C. C.; Ng, S. C.; Luong, J. H. T., *Journal of Physical Chemistry C* **2008**, 112 (2), 443-451.
77. Zhu, C. Y.; Xue, J. F.; He, J. H., *Journal of Nanoscience and Nanotechnology* **2009**, 9 (5), 3067-3074.
78. Kim, P.; Joo, J. B.; Kim, W.; Kim, J.; Song, I. K.; Yi, J., *Journal of Power Sources* **2006**, 160 (2), 987-990.
79. Wi*eckowski, A.; Savinova, E. R.; Vayenas, C. G., *Catalysis and electrocatalysis at nanoparticle surfaces*. Marcel Dekker: New York, 2003; p 970.
80. Lu, J. M.; Dreisinger, D. B.; Cooper, W. C., *Hydrometallurgy* **1997**, 45 (3), 305-322.
81. Kinge, S.; Bonnemann, H., *Applied Organometallic Chemistry* **2006**, 20 (11), 784-787.
82. Lu, F.; Liu, J.; Xu, J., *Materials Chemistry and Physics* **2008**, 108 (2-3), 369-374.
83. Vargaftik, M. N.; Zagorodnikov, V. P.; Stolyarov, I. P.; Moiseev, I. I.; Likholobov, V. A.; Kochubey, D. I.; Chuvilin, A. L.; Zaikovskiy, V. I.; Zamaraev, K. I.; Timofeeva, G. I., *Journal of the Chemical Society-Chemical Communications* **1985**, (14), 937-939.
84. Vargaftik, M. N.; Zagorodnikov, V. P.; Stolyarov, I. P.; Kochubei, D. I.; Nekipelov, V. M.; Mastikhin, V. M.; Chinakov, V. D.; Zamaraev, K. I.; Moiseev, I. I., *Bulletin of the Academy of Sciences of the USSR Division of Chemical Science* **1985**, 34 (10), 2206-2209.
85. Niesz, K.; Grass, M.; Somorjai, G. A., *Nano Lett* **2005**, 5 (11), 2238-40.
86. Zheng, N.; Fan, J.; Stucky, G. D., *Journal of the American Chemical Society* **2006**, 128 (20), 6550-6551.
87. Warren, S. C.; Jackson, A. C.; Cater-Cyker, Z. D.; DiSalvo, F. J.; Wiesner, U., *Journal of the American Chemical Society* **2007**, 129 (33), 10072-10073.

88. Sugimoto, T., *Fine particles : synthesis, characterization, and mechanisms of growth*. Marcel Dekker: New York, 2000; p 738.
89. Liz-Marzán, L. M.; Kamat, P. V., *Nanoscale materials*. Kluwer Academic Publishers: Boston, 2003; p 499.
90. Mallik, K.; Mandal, M.; Pradhan, N.; Pal, T., *Nano Letters* **2001**, *1* (6), 319-322.
91. Lu, Y.; Mei, Y.; Schrunner, M.; Ballauff, M.; Moller, M. W., *Journal of Physical Chemistry C* **2007**, *111* (21), 7676-7681.
92. Ozkaraoglu, E.; Tunc, K.; Suzer, S., *Polymer* **2009**, *50* (2), 462-466.
93. Kapoor, S.; Mukherjee, T., *Chemical Physics Letters* **2003**, *370* (1-2), 83-87.
94. Murakata, T.; Higashi, Y.; Yasui, N.; Higuchi, T.; Sato, S., *Journal of Chemical Engineering of Japan* **2002**, *35* (12), 1270-1276.
95. Schmid, G., *Nanoparticles : from theory to application*. Wiley-VCH ; John Wiley: Weinheim Chichester, 2004; p 434.
96. Shipway, A. N.; Katz, E.; Willner, I., *Chemphyschem* **2000**, *1* (1), 18-52.
97. Kotov, N. A., *Nanoparticle assemblies and superstructures*. Taylor & Francis: Boca Raton, FL, 2006; p 626.
98. Caruso, F., *Colloids and colloid assemblies : synthesis, modification, organization and utilization of colloid particles*. Wiley-VCH: Weinheim ; New York, 2004; p 603.
99. Chen, Y.; Munechika, K.; Ginger, D. S., *Nano Letters* **2007**, *7* (3), 690-696.
100. Sakai, N.; Fujiwara, Y.; Arai, M.; Yu, K.; Tatsuma, T., *Journal of Electroanalytical Chemistry* **2009**, *628* (1-2), 7-15.
101. Zhang, G. D.; Chen, X.; Zhao, J. K.; Chai, Y. C.; Zhuang, W. C.; Wang, L. Y., *Materials Letters* **2006**, *60* (23), 2889-2892.
102. Frisiras, C. T., *Progress in nanoparticles research*. Nova Science Publishers: New York, 2008; p 378.
103. Wang, W.; Gutu, T.; Gale, D. K.; Jiao, J.; Rorrer, G. L.; Chang, C. H., *Journal of the American Chemical Society* **2009**, *131* (12), 4178-4179.
104. Limsavarn, L.; Sritaveesinsub, V.; Dubas, S. T., *Materials Letters* **2007**, *61* (14-15), 3048-3051.
105. Yang, G. B.; Geng, Z. G.; Ma, H. X.; Wu, Z. S.; Zhang, P. Y., *Thin Solid Films* **2009**, *517* (5), 1778-1783.

106. Pinto, R. J. B.; Marques, P. A. A. P.; Martins, M. A.; Neto, C. P.; Trindade, T., *Journal of Colloid and Interface Science* **2007**, *312* (2), 506-512.
107. Pol, V. G.; Grisar, H.; Gedanken, A., *Langmuir* **2005**, *21* (8), 3635-3640.
108. Sarkar, J.; Pal, P.; Talapatra, G. B., *Chemical Physics Letters* **2005**, *401* (4-6), 400-404.
109. Galvez, N.; Fernandez, B.; Sanchez, P.; Morales-Sanfrutos, J.; Santoyo-Gonzalez, F.; Cuesta, R.; Bermejo, R.; Clemente-Leon, M.; Coronado, E.; Soriano-Portillo, A.; Dominguez-Vera, J. M., *Solid State Sciences* **2009**, *11* (4), 754-759.
110. Mammeri, F.; Le Bras, Y.; Daou, T. J.; Gallani, J. L.; Colis, S.; Pourroy, G.; Donnio, B.; Guillon, D.; Begin-Colin, S., *Journal of Physical Chemistry B* **2009**, *113* (3), 734-738.
111. Xu, B.; Wang, Y.; Zhang, Y. F., *Chemical Journal of Chinese Universities-Chinese* **2008**, *29* (7), 1317-1320.
112. Lee, D. K.; Kim, Y. H.; Kim, C. W.; Cha, H. G.; Kang, Y. S., *Journal of Physical Chemistry B* **2007**, *111* (31), 9288-9293.
113. Jiang, C. Y.; Markutsya, S.; Tsukruk, V. V., *Langmuir* **2004**, *20* (3), 882-890.
114. Kim, J. S.; Rieter, W. J.; Taylor, K. M. L.; An, H.; Lin, W. L.; Lin, W. B., *Journal of the American Chemical Society* **2007**, *129* (29), 8962-8963.
115. Srivastava, S.; Kotov, N. A., *Accounts of Chemical Research* **2008**, *41* (12), 1831-1841.
116. Dietrich, C.; Koslowski, B.; Weigl, F.; Ziemann, P., *Surface and Interface Analysis* **2006**, *38* (6), 1034-1038.
117. Li, Q. G.; Zheng, J. W.; Liu, Z. F., *Langmuir* **2003**, *19* (1), 166-171.
118. Plaza, J. L.; Chen, Y.; Jacke, S.; Palmer, R. E., *Langmuir* **2005**, *21* (4), 1556-1559.
119. Di Ventra, M.; Evoy, S.; Heflin, J. R., *Introduction to nanoscale science and technology*. Kluwer Academic Publishers: Boston, 2004; p 611.
120. Cerf, A.; Vieu, C., *Colloids and Surfaces a-Physicochemical and Engineering Aspects* **2009**, *342* (1-3), 136-140.
121. Li, Z. W.; Gu, Y. N.; Wang, L.; Ge, H. X.; Wu, W.; Xia, Q. F.; Yuan, C. S.; Chen, Y.; Cui, B.; Williams, R. S., *Nano Letters* **2009**, *9* (6), 2306-2310.
122. Santhanam, V.; Andres, R. P., *Nano Letters* **2004**, *4* (1), 41-44.
123. Weibel, D. B.; DiLuzio, W. R.; Whitesides, G. M., *Nature Reviews Microbiology* **2007**, *5* (3), 209-218.

124. Niu, Y., Dendrimer-encapsulated metal nanoparticles synthesis, characterization, and applications to catalysis. Texas A&M University: College Station, Tex., 2004.
125. Tanaka, T., *Experimental methods in polymer science : modern methods in polymer research and technology*. Academic Press: San Diego, 2000; p 604.
126. Adachi, M.; Lockwood, D. J.; SpringerLink (Online service), *Self-Organized Nanoscale Materials*. Springer Science+Business Media, Inc.: New York, NY, 2006.
127. Nicolais, L.; Carotenuto, G., *Metal-polymer nanocomposites*. Wiley-Interscience: Hoboken, N.J., 2005; p 300.
128. Koetz, J.; Kosmella, S.; SpringerLink (Online service), *Polyelectrolytes and Nanoparticles*. Springer-Verlag Berlin Heidelberg: Berlin, Heidelberg, 2007; p 54-55.
129. Wang, Z. L., *Characterization of nanophase materials*. 1st ed.; Wiley-VCH: Weinheim ; New York, 2000; p 406.
130. Griffiths, P. R.; De Haseth, J. A., *Fourier transform infrared spectrometry*. 2nd ed.; Wiley-Interscience: Hoboken, N.J., 2007; p 529.
131. Smith, B. C., *Fundamentals of Fourier transform infrared spectroscopy*. CRC Press: Boca Raton, 1996; p 202.
132. Pelletier, M. J., *Analytical applications of Raman spectroscopy*. Blackwell Science: Oxford ; Malden, MA, 1999; p 478.
133. Hendra, P.; Jones, C.; Warnes, G., *Fourier transform Raman spectroscopy : instrumentation and chemical applications*. Ellis Horwood: New York, 1991; p 311.
134. Williams, D. B.; Carter, C. B., *Transmission electron microscopy : a textbook for materials science*. 2nd ed.; Springer: New York ; London, 2008.
135. Fultz, B.; Howe, J. M., *Transmission electron microscopy and diffractometry of materials*. 2nd ed.; Springer: Berlin ; New York, 2002; p 748.
136. Rühle, M.; Ernst, F., *High-resolution imaging and spectrometry of materials*. Springer: Berlin ; New York, 2003; p 440.
137. Buseck, P.; Cowley, J. M.; Eyring, L., *High-resolution transmission electron microscopy and associated techniques*. Oxford University Press: New York, 1988; p 645.
138. Goldstein, J., *Scanning electron microscopy and x-ray microanalysis*. 3rd ed.; Springer: New York, 2003; p 689.
139. Zhou, W.; Wang, Z. L., *Scanning microscopy for nanotechnology : techniques and applications*. Springer: New York, 2007; p 522.

140. Koo, J. H., *Polymer nanocomposites : processing, characterization, and applications*. McGraw-Hill: New York, 2006; p 272.
141. Srnova-Sloufova, I.; Vlckova, B.; Bastl, Z.; Hasslett, T. L., *Langmuir* **2004**, *20* (8), 3407-3415.
142. Herzing, A. A.; Watanabe, M.; Edwards, J. K.; Conte, M.; Tang, Z. R.; Hutchings, G. J.; Kiely, C. J., *Faraday Discussions* **2008**, *138*, 337-351.
143. Niemantsverdriet, J. W., *Spectroscopy in catalysis : an introduction*. 3rd rev ed.; Wiley-VCH ; John Wiley, Weinheim Chichester, 2007; p 325.
144. Briggs, D.; Grant, J. T., *Surface analysis by Auger and x-ray photoelectron spectroscopy*. IM Publications: Chichester, West Sussex, U.K., 2003; p 899.
145. Bernasek, S. L., *Heterogeneous reaction dynamics*. VCH: New York, 1995; p 158.
146. Guinier, A., *X-ray diffraction in crystals, imperfect crystals, and amorphous bodies*. Dover: New York, 1994; p 378.
147. Klug, H. P.; Alexander, L. E., *X-ray diffraction procedures for polycrystalline and amorphous materials*. Wiley: New York,, 1954; p 716.
148. Wang, Z. L.; Liu, Y.; Zhang, Z., *Handbook of nanophase and nanostructured materials*. Kluwer Academic/Plenum: New York, 2003.
149. Morita, S.; Wiesendanger, R.; Meyer, E., *Noncontact atomic force microscopy*. Springer: Berlin ; New York, 2002; p 439.
150. Mee, C. D.; Daniel, E. D., *Magnetic recording technology*. 2nd ed.; McGraw-Hill: New York, 1996; p 704.
151. Czichos, H.; Saito, T.; Smith, L. R., *Springer handbook of materials measurement methods*. Springer: Germany, 2006; p 1208.
152. Cullity, B. D.; Graham, C. D., *Introduction to magnetic materials*. 2nd ed.; IEEE/Wiley: Hoboken, N.J., 2009; p 544.
153. Wang, H. D.; Sun, X. Q.; Ye, Y.; Qiu, S. L., *Journal of Power Sources* **2006**, *161* (2), 839-842.
154. Christensen, P. A.; Hamnett, A.; NetLibrary Inc., *Techniques and mechanisms in electrochemistry*. 1st ed. ed.; Blackie Academic & Professional,; London ; New York, 1994. p 379.
155. Kumar, C. S. S. R., *Metallic Nanomaterials*. Wiley-VCH, 2009 ; p 596.

156. McGrath, K. M.; Prakash, G. K. S.; Olah, G. A., *Journal of Industrial and Engineering Chemistry* **2004**, *10* (7), 1063-1080.
157. Antolini, E.; Lopes, T.; Gonzalez, E. R., *Journal of Alloys and Compounds* **2008**, *461* (1-2), 253-262.
158. Vigier, F.; Rousseau, S.; Coutanceau, C.; Leger, J. M.; Lamy, C., *Topics in Catalysis* **2006**, *40* (1-4), 111-121.
159. Kjeang, E.; Goldak, J.; Golriz, M. R.; Gu, J.; James, D.; Kordesch, K., *Journal of Power Sources* **2006**, *153* (1), 89-99.
160. Hogarth, M. P.; Ralph, T. R., *Platinum Metals Review* **2002**, *46* (4), 146-164.
161. Zhdanov, V. P.; KaSerno, B., *Electrochemistry Communications* **2006**, *8* (7), 1132-1136.
162. Lovic, J., *Journal of the Serbian Chemical Society* **2007**, *72* (7), 709-712.
163. Liu, H. S.; Song, C. J.; Zhang, L.; Zhang, J. J.; Wang, H. J.; Wilkinson, D. P., *Journal of Power Sources* **2006**, *155* (2), 95-110.
164. Yano, H.; Inukai, J.; Uchida, H.; Watanabe, M.; Babu, P. K.; Kobayashi, T.; Chung, J. H.; Oldfield, E.; Wieckowski, A., *Physical Chemistry Chemical Physics* **2006**, *8* (42), 4932-4939.
165. Ye, H.; Crooks, J. A.; Crooks, R. M., *Langmuir* **2007**, *23* (23), 11901-11906.
166. Zhang, L.; Lee, K. C.; Zhang, J. J., *Electrochimica Acta* **2007**, *52* (28), 7964-7971.
167. Ahmadi, T. S.; Wang, Z. L.; Green, T. C.; Henglein, A.; ElSayed, M. A., *Science* **1996**, *272* (5270), 1924-1926.
168. Elechiguerra, J. L.; Larios-Lopez, L.; Jose-Yacaman, M., *Applied Physics a-Materials Science & Processing* **2006**, *84* (1-2), 11-19.
169. Siani, A.; Wigal, K. R.; Alexeev, O. S.; Amiridis, M. D., *Journal of Catalysis* **2008**, *257* (1), 5-15.
170. Li, J.; Liang, Y.; Xu, Q. C.; Fu, X. Z.; Xu, J. Q.; Lin, J. D., *Journal of Nanoscience and Nanotechnology* **2006**, *6* (4), 1107-1113.
171. Chen, J. Y.; Herricks, T.; Xia, Y. N., *Angewandte Chemie-International Edition* **2005**, *44* (17), 2589-2592.
172. Maiyalagan, T., *Journal of Power Sources* **2008**, *179* (2), 443-450.
173. Chen, C. W.; Takezako, T.; Yamamoto, K.; Serizawa, T.; Akashi, M., *Colloids and Surfaces a-Physicochemical and Engineering Aspects* **2000**, *169* (1-3), 107-116.

174. Mizukoshi, Y.; Takagi, E.; Okuno, H.; Oshima, R.; Maeda, Y.; Nagata, Y., *Ultrasonics Sonochemistry* **2001**, *8* (1), 1-6.
175. He, B. L.; Chen, Y. X.; Liu, H. F.; Liu, Y., *Journal of Nanoscience and Nanotechnology* **2005**, *5* (2), 266-270.
176. Einaga, H.; Harada, M., *Langmuir* **2005**, *21* (6), 2578-2584.
177. Sastry, M.; Patil, V.; Mayya, K. S.; Paranjape, D. V.; Singh, P.; Sainkar, S. R., *Thin Solid Films* **1998**, *324* (1-2), 239-244.
178. Sakamoto, Y.; Fukuoka, A.; Higuchi, T.; Shimomura, N.; Inagaki, S.; Ichikawa, M., *Journal of Physical Chemistry B* **2004**, *108* (3), 853-858.
179. Luo, X. H.; Imae, T., *Journal of Materials Chemistry* **2007**, *17* (6), 567-571.
180. Luo, Y. L.; Sun, X. P., *Materials Letters* **2007**, *61* (10), 2015-2017.
181. Liang, H. P.; Jones, T. G. J.; Lawrence, N. S.; Jiang, L.; Barnard, J. S., *Journal of Physical Chemistry C* **2008**, *112* (11), 4327-4332.
182. Kuo, P. L.; Chen, W. F.; Huang, H. Y.; Chang, I. C.; Dai, S. A., *Journal of Physical Chemistry B* **2006**, *110* (7), 3071-3077.
183. Laschi, S.; Bulukin, E.; Palchetti, I.; Cristea, C.; Mascini, M., *Irbm* **2008**, *29* (2-3), 202-207.
184. Rubianes, M. D.; Rivas, G. A., *Electrochemistry Communications* **2007**, *9* (3), 480-484.
185. Jena, B. K.; Raj, C. R., *Journal of Physical Chemistry C* **2008**, *112* (10), 3496-3502.
186. Pan, M.; Tang, H. L.; Jiang, S. P.; Liu, Z. C., *Journal of the Electrochemical Society* **2005**, *152* (6), A1081-a1088.
187. Estephan, Z. G.; Alawieh, L.; Halaoui, L. I., *Journal of Physical Chemistry C* **2007**, *111* (22), 8060-8068.
188. Tian, Z. Q.; Jiang, S. P.; Liu, Z. C.; Li, L., *Electrochemistry Communications* **2007**, *9* (7), 1613-1618.
189. Harada, M.; Okamoto, K.; Terazima, M., *Langmuir* **2006**, *22* (22), 9142-9149.
190. Harada, M.; Einaga, H., *Langmuir* **2006**, *22* (5), 2371-2377.
191. Xie, H.; Gu, Y. L.; Ploehn, H. J., *Nanotechnology* **2005**, *16* (7), S492-S501.
192. Knecht, M. R.; Weir, M. G.; Myers, V. S.; Pyrz, W. D.; Ye, H.; Petkov, V.; Buttrey, D. J.; Frenkel, A. I.; Crooks, R. M., *Chemistry of Materials* **2008**, *20* (16), 5218-5228.

193. Cameron, R. E.; Bocarsly, A. B., *Inorganic Chemistry* **1986**, 25 (16), 2910-2913.
194. Praharaj, S.; Nath, S.; Ghosh, S. K.; Kundu, S.; Pal, T., *Langmuir* **2004**, 20 (23), 9889-92.
195. Hayakawa, K.; Yoshimura, T.; Esumi, K., *Langmuir* **2003**, 19 (13), 5517-5521.
196. Silva, C. P.; Carapuca, H. M., *Electrochimica Acta* **2006**, 52 (3), 1182-1190.
197. De Castro, E. S.; Huber, E. W.; Villarroel, D.; Galiatsatos, C.; Mark, J. E.; Heineman, W. R.; Murray, P. T., *Analytical Chemistry* **1987**, 59 (1), 134-139.
198. Frelink, T.; Visscher, W.; Vanveen, J. A. R., *Journal of Electroanalytical Chemistry* **1995**, 382 (1-2), 65-72.
199. Komanicky, V.; Menzel, A.; You, H., *Journal of Physical Chemistry B* **2005**, 109 (49), 23550-23557.
200. Komanicky, V.; Menzel, A.; Chang, K. C.; You, H., *Journal of Physical Chemistry B* **2005**, 109 (49), 23543-23549.
201. Lin, Y. H.; Cui, X. L.; Yen, C.; Wai, C. M., *Journal of Physical Chemistry B* **2005**, 109 (30), 14410-14415.
202. Formo, E.; Peng, Z. M.; Lee, E.; Lu, X. M.; Yang, H.; Xia, Y. N., *Journal of Physical Chemistry C* **2008**, 112 (27), 9970-9975.
203. Wang, J.; Swain, G. M., *Journal of the Electrochemical Society* **2003**, 150 (1), E24-E32.
204. Miki, A.; Ye, S.; Senzaki, T.; Osawa, M., *Journal of Electroanalytical Chemistry* **2004**, 563 (1), 23-31.
205. Liu, Z. L.; Ling, X. Y.; Su, X. D.; Lee, J. Y., *Journal of Physical Chemistry B* **2004**, 108 (24), 8234-8240.
206. Geng, D. S.; Lu, G. X., *Journal of Physical Chemistry C* **2007**, 111 (32), 11897-11902.
207. Chen, A. C.; La Russa, D. J.; Miller, B., *Langmuir* **2004**, 20 (22), 9695-9702.
208. Girishkumar, G.; Vinodgopal, K.; Kamat, P. V., *Journal of Physical Chemistry B* **2004**, 108 (52), 19960-19966.
209. Zhang, Y. J.; Zhu, J., *Micron* **2002**, 33 (6), 523-534.
210. Wang, Z. L., *Nanowires and nanobelts : materials, properties and devices*. Springer: New York, 2006, p 475.
211. Hu, J. T.; Odom, T. W.; Lieber, C. M., *Accounts of Chemical Research* **1999**, 32 (5), 435-445.

212. Song, R. Q.; Xu, A. W.; Yu, S. H., *Journal of the American Chemical Society* **2007**, *129* (14), 4152-4153.
213. Gautam, U. K.; Rao, C. N. R., *Journal of Materials Chemistry* **2004**, *14* (16), 2530-2535.
214. Liu, Y. K.; Wang, G. H.; Xu, C. K.; Wang, W. Z., *Chemical Communications* **2002**, (14), 1486-1487.
215. Chen, H.; Elabd, Y. A.; Palmese, G. R., *Journal of Materials Chemistry* **2007**, *17* (16), 1593-1596.
216. Audoit, G.; Kulkarni, J. S.; Morris, M. A.; Holmes, J. D., *Journal of Materials Chemistry* **2007**, *17* (16), 1608-1613.
217. Li, Y. G.; Tan, B.; Wu, Y. Y., *Journal of the American Chemical Society* **2006**, *128* (44), 14258-14259.
218. Mondal, S. P.; Das, K.; Dhar, A.; Ray, S. K., *Nanotechnology* **2007**, *18* (9), 095606.
219. Fukuoka, A.; Sakamoto, Y.; Higuchi, T.; Shimomura, N.; Ichikawa, M., *Journal of Porous Materials* **2006**, *13* (3-4), 231-235.
220. Rumplecker, A.; Kleitz, F.; Salabas, E. L.; Schuth, F., *Chemistry of Materials* **2007**, *19* (3), 485-496.
221. Kou, X. S.; Zhang, S. Z.; Tsung, C. K.; Yang, Z.; Yeung, M. H.; Stucky, G. D.; Sun, L. D.; Wang, J. F.; Yan, C. H., *Chemistry-a European Journal* **2007**, *13* (10), 2929-2936.
222. Li, Z. Q.; Xiong, Y. J.; Xie, Y., *Nanotechnology* **2005**, *16* (10), 2303-2308.
223. Wang, X. D.; Summers, C. J.; Wang, Z. L., *Nano Letters* **2004**, *4* (3), 423-426.
224. Deng, Z. X.; Tian, Y.; Lee, S. H.; Ribbe, A. E.; Mao, C. D., *Angewandte Chemie, International Edition* **2005**, *44* (23), 3582-3585.
225. Poizot, P.; Laruelle, S.; Grugeon, S.; Dupont, L.; Tarascon, J. M., *Nature* **2000**, *407* (6803), 496-499.
226. Li, Y. G.; Tan, B.; Wu, Y. Y., *Nano Letters* **2008**, *8* (1), 265-270.
227. Li, W. Y.; Xu, L. N.; Chen, J., *Advanced Functional Materials* **2005**, *15* (5), 851-857.
228. Cao, A. M.; Hu, J. S.; Liang, H. P.; Song, W. G.; Wan, L. J.; He, X. L.; Gao, X. G.; Xia, S. H., *Journal of Physical Chemistry B* **2006**, *110* (32), 15858-15863.
229. Bahlawane, N.; Rivera, E. F.; Kohse-Hoinghaus, K.; Brechling, A.; Kleineberg, U., *Applied Catalysis B: Environmental* **2004**, *53* (4), 245-255.

230. Hutchins, M. G.; Wright, P. J.; Grebenik, P. D., *Solar Energy Materials* **1987**, *16* (1-3), 113-131.
231. Sugimoto, T.; Matijevic, E., *Journal of Inorganic and Nuclear Chemistry* **1979**, *41* (2), 165-172.
232. Yang, R. Z.; Wang, Z. X.; Liu, J. Y.; Chen, L. Q., *Electrochemical and Solid-State Letters* **2004**, *7* (12), 496-499.
233. Li, L.; Ren, J. C., *Materials Research Bulletin* **2006**, *41* (12), 2286-2290.
234. Larcher, D.; Sudant, G.; Leriche, J. B.; Chabre, Y.; Tarascon, J. M., *Journal of the Electrochemical Society* **2002**, *149* (3), 234-241.
235. Xu, R.; Zeng, H. C., *Journal of Physical Chemistry B* **2003**, *107* (46), 12643-12649.
236. Yang, L. X.; Zhu, Y. J.; Li, L.; Zhang, L.; Tong, H.; Wang, W. W.; Cheng, G. F.; Zhu, J. F., *European Journal of Inorganic Chemistry* **2006**, (23), 4787-4792.
237. Guan, H. Y.; Shao, C. L.; Wen, S. B.; Chen, B.; Gong, J.; Yang, X. H., *Materials Chemistry and Physics* **2003**, *82* (3), 1002-1006.
238. Hou, Y. L.; Kondoh, H.; Shimojo, M.; Kogure, T.; Ohta, T., *Journal of Physical Chemistry B* **2005**, *109* (41), 19094-19098.
239. Yu, T.; Zhu, Y. W.; Xu, X. J.; Shen, Z. X.; Chen, P.; Lim, C. T.; Thong, J. T. L.; Sow, C. H., *Advanced Materials* **2005**, *17* (13), 1595-1599.
240. Spinolo, G.; Ardizzone, S.; Trasatti, S., *Journal of Electroanalytical Chemistry* **1997**, *423* (1-2), 49-57.
241. Kim, D. Y.; Ju, S. H.; Koo, H. Y.; Hong, S. K.; Kang, Y. C., *Journal of Alloys and Compounds* **2006**, *417* (1-2), 254-258.
242. Braun, D.; Cherdron, H.; Rehahn, M.; Ritter, H.; Voit, B.; SpringerLink (Online service), *Polymer Synthesis: Theory and Practice Fundamentals, Methods, Experiments*. Fourth Edition. ed.; Springer-Verlag Berlin Heidelberg: Berlin, Heidelberg, 2005. <http://libdata.lib.ua.edu/login?url=http://dx.doi.org/10.1007/b138247>.
243. Zou, D. B.; Xu, C.; Luo, H.; Wang, L.; Ying, T. K., *Materials Letters* **2008**, *62* (12-13), 1976-1978.
244. de la Hoz, A.; Diaz-Ortiz, A.; Moreno, A., *Chemical Society Reviews* **2005**, *34* (2), 164-178.
245. Ni, Y. H.; Ge, X. W.; Zhang, Z. C.; Liu, H. R.; Zhu, Z. L.; Ye, Q., *Materials Research Bulletin* **2001**, *36* (13-14), 2383-2387.
246. Itakura, T.; Torigoe, K.; Esumi, K., *Langmuir* **1995**, *11* (10), 4129-4134.

247. Machida, R.; Kimura, E.; Kodama, M., *Inorganic Chemistry* **1983**, 22 (14), 2055-2061.
248. Warren, S. C.; Jackson, A. C.; Cater-Cyker, Z. D.; DiSalvo, F. J.; Wiesner, U., *Journal of the American Chemical Society* **2007**, 129 (33), 10072-10073.
249. Ramana, C. V.; Massot, M.; Julien, C. M., *Surface and Interface Analysis* **2005**, 37 (4), 412-416.
250. Hadjiev, V. G.; Iliev, M. N.; Vergilov, I. V., *Journal of Physics C: Solid State Physics* **1988**, 21 (7), 199-201.
251. McLendon, G.; Martell, A. E., *Coordination Chemistry Reviews* **1976**, 19 (1), 1-39.
252. Bogucki, R. F.; McLendon, G.; Martell, A. E., *Journal of the American Chemical Society* **1976**, 98 (11), 3202-3205.
253. A. G. Sykes, J. A. W., The Formation, Structure, and Reactions of Binuclear Complexes of Cobalt. In *Progress in Inorganic Chemistry*, John, O. E., Ed. 1970; 1-106.
254. Miller, F.; Simplicio, J.; Wilkins, R. G., *Journal of the American Chemical Society* **1969**, 91 (8), 1962-1967.
255. Bosman, A. W.; Janssen, H. M.; Meijer, E. W., *Chemical Reviews* **1999**, 99 (7), 1665-1688.
256. Maiti, P. K.; Cagin, T.; Wang, G. F.; Goddard, W. A., *Macromolecules* **2004**, 37 (16), 6236-6254.
257. Esumi, K.; Isono, R.; Yoshimura, T., *Langmuir* **2004**, 20 (1), 237-243.
258. Scott, R. W. J.; Wilson, O. M.; Crooks, R. M., *Journal of Physical Chemistry B* **2005**, 109 (2), 692-704.
259. Nalwa, H. S., *Magnetic nanostructures*. American Scientific Publishers: Stevenson Ranch, Calif., 2002; p 463.
260. Hoinville, J.; Bewick, A.; Gleeson, D.; Jones, R.; Kasyutich, O.; Mayes, E.; Nartowski, A.; Warne, B.; Wiggins, J.; Wong, K., *Journal of Applied Physics* **2003**, 93 (10), 7187-7189.
261. Ma, Z. Y.; Liu, H. Z., *China Particuology* **2007**, 5 (1-2), 1-10.
262. Kondo, A.; Ohnishi, N., *Journal of the Japan Society for Bioscience Biotechnology and Agrochemistry* **2003**, 77 (9), 861-864.
263. Lu, Y.; Lu, X. M.; Mayers, B. T.; Herricks, T.; Xia, Y. N., *Journal of Solid State Chemistry* **2008**, 181 (7), 1530-1538.

264. Nguyen, H. L.; Howard, L. E. M.; Stinton, G. W.; Giblin, S. R.; Tanner, B. K.; Terry, I.; Hughes, A. K.; Ross, I. M.; Serres, A.; Evans, J. S. O., *Chemistry of Materials* **2006**, *18* (26), 6414-6424.
265. Zhang, Z. J.; Chen, X. Y.; Zhang, X. F.; Shi, C. W., *Solid State Communications* **2006**, *139* (8), 403-405.
266. Yan, H.; Zhang, J. C.; You, C. X.; Song, Z. W.; Yu, B. W.; Shen, Y., *Materials Chemistry and Physics* **2009**, *113* (1), 46-52.
267. Varanda, L. C.; Jafelicci, M., *Journal of the American Chemical Society* **2006**, *128* (34), 11062-11066.
268. Liu, Z. F.; Ada, E. T.; Shamsuzzoha, M.; Thompson, G. B.; Nikles, D. E., *Chemistry of Materials* **2006**, *18* (20), 4946-4951.
269. Liu, C.; Wu, X. W.; Klemmer, T.; Shukla, N.; Yang, X. M.; Weller, D.; Roy, A. G.; Tanase, M.; Laughlin, D., *Journal of Physical Chemistry B* **2004**, *108* (20), 6121-6123.
270. Dai, Z. R.; Sun, S. H.; Wang, Z. L., *Nano Letters* **2001**, *1* (8), 443-447.
271. Wang, H. L.; Huang, Y.; Zhang, Y.; Hadjipanayis, G. C.; Weller, D.; Simopoulos, A., *Journal of Magnetism and Magnetic Materials* **2007**, *310* (1), 22-27.
272. Gibot, P.; Tronc, E.; Chaneac, C.; Jolivet, J. P.; Fiorani, D.; Testa, A. M., *Journal of Magnetism and Magnetic Materials* **2005**, *290*, 555-558.
273. Caiulo, N.; Yu, C. H.; Yu, K. M. K.; Lo, C. C. H.; Oduro, W.; Thiebaut, B.; Bishop, P.; Tsang, S. C., *Advanced Functional Materials* **2007**, *17* (8), 1392-1396.
274. Zeng, Q.; Zhang, Y.; Wang, H. L.; Papaefthymiou, V.; Hadjipanayis, G. C., *Journal of Magnetism and Magnetic Materials* **2004**, *272*, 1223-1225.
275. Stahl, B.; Gajbhiye, N. S.; Wilde, G.; Kramer, D.; Ellrich, J.; Ghafari, M.; Hahn, H.; Gleiter, H.; Weissmuller, J.; Wurschum, R.; Schlossmacher, P., *Advanced Materials* **2002**, *14* (1), 24-27.
276. Sun, S. H.; Anders, S.; Thomson, T.; Baglin, J. E. E.; Toney, M. F.; Hamann, H. F.; Murray, C. B.; Terris, B. D., *Journal of Physical Chemistry B* **2003**, *107* (23), 5419-5425.
277. Yu, C. H.; Caiulo, N.; Lo, C. C. H.; Tam, K.; Tsang, S. C., *Advanced Materials* **2006**, *18* (17), 2312-2314.
278. Miller, S. A.; Hong, E. D.; Wright, D., *Macromolecular Bioscience* **2006**, *6* (10), 839-845.
279. Knecht, M. R.; Wright, D. W., *Chemistry of Materials* **2004**, *16* (24), 4890-4895.
280. Rong, C. B.; Li, D. R.; Nandwana, V.; Poudyal, N.; Ding, Y.; Wang, Z. L.; Zeng, H.; Liu, J. P., *Advanced Materials* **2006**, *18* (22), 2984-2988.

281. Gubin, S. P., *Magnetic nanoparticles*. Wiley-VCH ; John Wiley: Weinheim, Chichester, 2008; p 484.
282. Jain, K. K.; SpringerLink (Online service), *The Handbook of Nanomedicine*. Humana Press: Totowa, NJ, 2008; p 403.
283. Kumar, C. S. S. R., *Nanomaterials for cancer diagnosis*. Wiley-VCH: Weinheim, 2007; p 423.
284. Parekh, K.; Upadhyay, R. V.; Aswal, V. K., *J Nanosci Nanotechnol* **2009**, *9* (3), 2104-2110.
285. Reddy, K. R.; Park, W.; Sin, B. C.; Noh, J.; Lee, Y., *J Colloid Interface Sci* **2009**, *335* (1), 34-39.
286. Yu, F.; Yang, V. C., *J Biomed Mater Res A* **2009**.
287. Cengelli, F.; Grzyb, J. A.; Montoro, A.; Hofmann, H.; Hanessian, S.; Juillerat-Jeanneret, L., *ChemMedChem* **2009**, *4* (6), 988-997.
288. Guo, S.; Li, D.; Zhang, L.; Li, J.; Wang, E., *Biomaterials* **2009**, *30* (10), 1881-1889.
289. Aslam, M.; Fu, L.; Li, S.; Dravid, V. P., *J Colloid Interface Sci* **2005**, *290* (2), 444-449.
290. Xuan, S. H.; Wang, Y. X. J.; Leung, K. C. F.; Shu, K. Y., *Journal of Physical Chemistry C* **2008**, *112* (48), 18804-18809.
291. Hatamie, S.; Dhole, S. D.; Ding, J.; Kale, S. N., *Journal of Magnetism and Magnetic Materials* **2009**, *321* (14), 2135-2138.
292. Daou, T. J.; Pourroy, G.; Greneche, J. M.; Bertin, A.; Felder-Flesch, D.; Begin-Colin, S., *Dalton Transactions* **2009**, (23), 4442-4449.
293. Gruner, M. E.; Rollmann, G.; Entel, P.; Farle, M., *Phys Rev Lett* **2008**, *100* (8), 087203.
294. Sun, X. C.; Huang, Y. H.; Nikles, D. E., *International Journal of Nanotechnology* **2004**, *1* (3), 328-346.
295. Niemeyer, C. M.; Mirkin, C. A., *Nanobiotechnology : concepts, applications and perspectives*. Wiley-VCH: Weinheim, 2004; p 469.
296. Kang, K.; Choi, J.; Nam, J. H.; Lee, S. C.; Kim, K. J.; Lee, S. W.; Chang, J. H., *J Phys Chem B* **2009**, *113* (2), 536-43.
297. Knecht, M. R.; Sewell, S. L.; Wright, D. W., *Langmuir* **2005**, *21* (5), 2058-2061.
298. Wan, H.; University of Alabama. Dept. of Chemistry. The photochemical reduction of dendrimer-mediated metal ions. Thesis (Ph D), University of Alabama, 2007.

299. Dimitrov, D. A.; Wysin, G. M., *Physical Review B* **1994**, *50* (5), 3077-3084.
300. Gradmann, U., *Journal of Magnetism and Magnetic Materials* **1991**, *100* (1-3), 481-496.
301. Wu, M. Z.; Ma, Y. Q.; Liu, Y. M.; Bi, H.; Fang, Q. Q.; Niu, H. L.; Chen, Q. W., *Materials Research Bulletin* **2008**, *43* (5), 1321-1326.
302. Wu, M. Z.; Xiong, Y.; Peng, Z. M.; Jiang, N.; Qi, H. P.; Chen, Q. W., *Materials Research Bulletin* **2004**, *39* (12), 1875-1880.
303. Hutlova, A.; Niznansky, D.; Rehspringer, J. L.; Estournes, C.; Kurmoo, M., *Advanced Materials* **2003**, *15* (19), 1622-1625.
304. Fiorani, D., *Surface effects in magnetic nanoparticles*. Springer: New York, 2005; p 299 .
305. Aktas, B.; Mikailov, F.; Tagirov, L., *Magnetic Nanostructures*. In *Springer Series in Materials Science*, Springer-Verlag Berlin Heidelberg: Berlin, Heidelberg, 2007; p 208.
306. Chou, S. Y., *Proceedings of the Ieee* **1997**, *85* (4), 652-671.
307. Adeyeye, A. O.; Singh, N., *Journal of Physics D-Applied Physics* **2008**, *41* (15), 29.
308. M.-P. Pileni, *Advanced Functional Materials* **2001**, *11* (5), 323-336.
309. Corr, S. A.; Byrne, S. J.; Tekoriute, R.; Meledandri, C. J.; Brougham, D. F.; Lynch, M.; Kerskens, C.; O'Dwyer, L.; Gun'ko, Y. K., *Journal of the American Chemical Society* **2008**, *130* (13), 4214-4215.
310. Sheparovych, R.; Sahoo, Y.; Motornov, M.; Wang, S. M.; Luo, H.; Prasad, P. N.; Sokolov, I.; Minko, S., *Chemistry of Materials* **2006**, *18* (3), 591-593.
311. Sun, J. F.; Zhang, Y.; Chen, Z. P.; Zhou, H.; Gu, N., *Angewandte Chemie-International Edition* **2007**, *46* (25), 4767-4770.
312. Fang, W. X.; He, Z. H.; Xu, X. Q.; Mao, Z. Q.; Shen, H., *Epl* **2007**, *77* (6), 68004.
313. Luttge, R., *Journal of Physics D-Applied Physics* **2009**, *42* (12), 18.
314. Getlawi, S.; Koblichka, M. R.; Hartmann, U.; Richter, C.; Sulzbach, T. In *Patterning of permalloy thin films by means of electron-beam lithography and focused ion-beam milling*, Academic Press Ltd Elsevier Science Ltd: 2008; pp 699-704.
315. Zhou, T. J.; Zhao, Y.; Wang, J. P.; Thong, J. T. L.; Chong, T. C. In *Ferromagnetic nano-dot array fabricated by electron beam radiation induced nano-scale phase transition*, Amer Inst Physics: 2002; pp 6854-6856.
316. Miyashita, K.; Nishimura, S.; Toyofuku, T.; Shirakashi, J. I., *Journal of Vacuum Science & Technology B* **2009**, *27* (2), 953-957.

317. Guo, L. J., *Advanced Materials* **2007**, *19* (4), 495-513.
318. Kraus, T.; Malaquin, L.; Schmid, H.; Riess, W.; Spencer, N. D.; Wolf, H., *Nature Nanotechnology* **2007**, *2* (9), 570-576.
319. Sun, M.; Zangari, G.; Shamsuzzoha, M.; Metzger, R. M., *Applied Physics Letters* **2001**, *78* (19), 2964-2966.
320. D. Pisignano; E. Sariconi; M. Mazzeo; G. Gigli; R. Cingolani, *Advanced Materials* **2002**, *14* (21), 1565-1567.
321. Cavallini, M.; Bystrenova, E.; Timko, M.; Koneracka, M.; Zavisova, V.; Kopcansky, P., *Journal of Physics-Condensed Matter* **2008**, *20* (20), 204144.
322. Chang, C. Y.; Yang, S. Y.; Huang, L. S.; Hsieh, K. H., *Optics Express* **2006**, *14* (13), 6253-6258.
323. Dong, R.; Jensen, T. W.; Engberg, K.; Nuzzo, R. G.; Leckband, D. E., *Langmuir* **2007**, *23* (3), 1483-1488.
324. Delamarche, E.; Bernard, A.; Schmid, H.; Michel, B.; Biebuyck, H., *Science* **1997**, *276* (5313), 779-781.
325. Xia, Y. N.; Whitesides, G. M., *Annual Review of Materials Science* **1998**, *28*, 153-184.
326. Yu, W.; Zhang, T.; Zhang, J.; Qiao, X.; Yang, L.; Liu, Y., *Materials Letters* **2006**, *60* (24), 2998-3001.
327. Goon, I. Y.; Lai, L. M. H.; Lim, M.; Munroe, P.; Gooding, J. J.; Amal, R., *Chemistry of Materials* **2009**, *21* (4), 673-681.
328. Si, S.; Kotal, A.; Mandal, T. K.; Giri, S.; Nakamura, H.; Kohara, T., *Chemistry of Materials* **2004**, *16* (18), 3489-3496.
329. Wu, M.; Ma, Y.; Liu, Y.; Bi, H.; Fang, Q.; Niu, H.; Chen, Q., *Materials Research Bulletin* **2008**, *43* (5), 1321-1326.
330. Young, W. D.; Prieve, D. C., *Industrial & Engineering Chemistry Research* **1996**, *35* (9), 3186-3194.
331. Xuan, Y.; Ye, M.; Li, Q., *International Journal of Heat and Mass Transfer* **2005**, *48* (12), 2443-2451.
332. Lee, L. T.; Leite, C. A. P.; Galembeck, F., *Langmuir* **2004**, *20* (11), 4430-4435.
333. Suematsu, N. J.; Ogawa, Y.; Yamamoto, Y.; Yamaguchi, T., *Journal of Colloid and Interface Science* **2007**, *310* (2), 648-652.
334. El-Deab, M. S.; Ohsaka, T., *Electrochemistry Communications* **2002**, *4* (4), 288-292.

335. Knoll, J.; Swavey, S., *Inorganica Chimica Acta* **2009**, 362 (9), 2989-2993.
336. Wang, C.; Daimon, H.; Sun, S. H., *Nano Letters* **2009**, 9 (4), 1493-1496.
337. Chen, S.; Ferreira, P. J.; Sheng, W. C.; Yabuuchi, N.; Allard, L. F.; Shao-Horn, Y., *Journal of the American Chemical Society* **2008**, 130 (42), 13818-13819.
338. Antoine, O.; Bultel, Y.; Durand, R., *Journal of Electroanalytical Chemistry* **2001**, 499 (1), 85-94.
339. Montiel, M.; Hernandez-Fernandez, P.; Fierro, J. L. G.; Rojas, S.; Ocon, P., *Journal of Power Sources* **2009**, 191 (2), 280-288.
340. Garsuch, A.; Michaud, X.; Wagner, G.; Klepel, O.; Dahn, J. R., *Electrochimica Acta* **2009**, 54 (4), 1350-1354.